Investigation into the iron-zinc coating constitution and crater evolution in galvanneal.

O'Dell, Simon Paul

University of Wales
Swansea

School of Engineering

Investigation into the Iron-Zinc Coating Constitution and Crater Evolution in Galvanneal

Simon Paul O'Dell

Materials Research Centre

Thesis submitted to the University of Wales in candidature for the degree of Engineering Doctorate

August 2004

ProQuest LLC.
789 East Eisenhower Parkway
P.O. Box 1346
Ann Arbor, MI 48106 – 1346

'If I have seen farther, it is by standing on the shoulders of giants.'

- Sir Isaac Newton (1676)

Declaration

This work has not previously been accepted in substance for any degree and is not being concurrently submitted in candidature for any degree.

Signed .....(candidate)

Date 4/11/04

Statement 1

This thesis is the result of my own investigations, except where otherwise stated. Other sources are acknowledged giving explicit references.

Signed .....(candidate)

Date 4/11/04

Statement 2

I hereby give consent for my thesis, if accepted, to be available for photocopying and for inter-library loans, and for the titla and summary to be made available to outside organisations.

Signed .....(candidate)

Date 4/11/04

Acknowledgements

The author gratefully acknowledges the support of EPSRC, Corus and the University of Wales, Swansea throughout the entirety of this doctorate. In particular the author would like to thank all the staff of ECM^2 who, through some difficult times, have maintained their professional integrity and without whom this thesis would never have been completed. A special thank-you to John Demmel for his continued determination and guidance with the Rhesca hot dip simulator.

The author would also like to thank all the students and staff involved with the Engineering Doctorate scheme for their help, support and advice on both a professional and personal level. In particular a big thank-you to Geraint, Hiram, Nicholas, Ian, Paul and Nathan for making the past four years much more entertaining and for acting as cannon fodder in our numerous games of Quake!

A sincere and heart felt thanks goes to my family and friends for their never ending support throughout my years of education. You have always been there when I needed you and have never stood in the way of me achieving my dreams. Thank-you.

TABLE OF CONTENTS

LIST OF TABLES

LIST OF FIGURES

1 INTRODUCTION TO THE PROJECT

The galvanneal coating forms by the isothermal solidification of molten zinc as a result of the diffusion of iron atoms from an effectively infinite source. The result is a coating with good paintability, weldability and corrosion resistance but with the potential to fail during press forming operations. Consequently considerable work has been carried out on the galvanneal product in the two main areas of coating failure and coating formation. The majority of this work has investigated the mechanisms by which the galvanneal coating fails and how the coating constitution influences this failure. However, there is a lack of understanding as to how the formation of surface features within the galvanneal coating may influence the properties of the coating.

In 1998 Carless presented a paper at the Galvatech international conference entitled 'Influence of Substrate Topography on the Formation of Iron-Zinc Phases and the Properties of Galvanneal Coatings'. In his paper Carless stated that the presence of 'craters' within the galvanneal coating increased the resistance to coating failure. In that same year an independent research project organised by the International Lead Zinc Research Organisation (ILZRO) and lead by Wright (1998) also reported similar findings. The project stated that the presence of craters within the galvanneal coating helped to reduce the amount of failure experienced by the galvanneal coating.

The work of both authors gave great insight into the possibility of manipulating the surface features of the coating to improve the resistance to coating failure. However, the work on 'craters' by Carless was only a small part of a much larger study and the work of Wright relied on industrial samples from numerous suppliers. What was needed was an in-depth investigation, under controlled conditions, into the effect of craters upon the properties of the galvanneal coating.

The primary objective of the project was therefore to

'investigate the iron-zinc coating constitution and crater evolution in galvanneal.'

Realisation of this primary objective was achieved by:

1. Developing a quantative technique for measuring and characterising craters.
2. Identifying the affect of process parameters upon the formation of craters.
3. Identifying the mechanism of crater formation during the growth and formation of the galvanneal coating.
4. Identifying the influence of craters upon the coating failure mechanism.
5. Developing a user-friendly computer model of the development of the galvanneal coating constitution.

These objectives were achieved through a critical review of the available literature and a systematic scientific investigation of both process and product.

1.1 THESIS LAYOUT

The first part of the thesis, chapter two, details a critical review of the published literature with regards to the galvannealing process, craters and the mechanisms of coating failure. The literature review then continues in chapter three by looking at the principle of diffusion couples and their application to the galvannealing reaction. The experimental procedures used to carry out the investigations are then explained in chapter four before detailing the programme of work to be carried out in chapter five. The results from each of the investigations are illustrated and explained in chapter six together with an in-depth discussion of the work relating back to the initial literature review. Finally, a general discussion combines each of the investigations in chapter seven to give an overview of the whole project before the final conclusions of the work are stated in chapter eight.

2 LITERATURE REVIEW

The following chapter details a critical review of the current literature regarding the use, production and development of galvanised products.

2.1 INTRODUCTION

The automotive industry is one of the most important markets for the steel industry and has provided the greatest stimulus and challenge for the development of new and improved metallic coatings and anti-corrosion techniques. In spite of competition from aluminium and plastic composites, steel has maintained its position as the predominant material for automobile body parts due to its good formability, ease of welding and relatively low cost.

However, constant developments within the plastics and aluminium industries mean that the steel industry must always be developing and attaining greater understanding of its own products. One such area of development is anti-corrosion protection. For decades, steel has been protected from corrosion by the application of zinc to its surface. However, continuing demands for better paintability, greater corrosion resistance, better formability and lower costs have prompted the development and study of alternative coating technologies and products for corrosion protection.

2.2 THE PROCESS OF CORROSION

Corrosion is a process by which a substance reaches thermodynamic equilibrium with its environment as a result of an electrochemical reaction. As with all electrochemical reactions an anode, a cathode, an electrolyte and a flow of electrons are present. The anode forms when the metal enters the electrolyte:

$$M \rightarrow M^{2+} + 2e^{-} \qquad (2.1)$$

The electrons then flow through the metal and are neutralised at a local cathode where a variety of possible reactions takes place. The most important of these involves the reduction of oxygen that can be written as:

$$O_2 + 2H_2O + 4e \rightarrow 4OH^- \qquad (2.2)$$

and results in OH^- ions being produced in the liquid which in turn becomes locally alkaline.

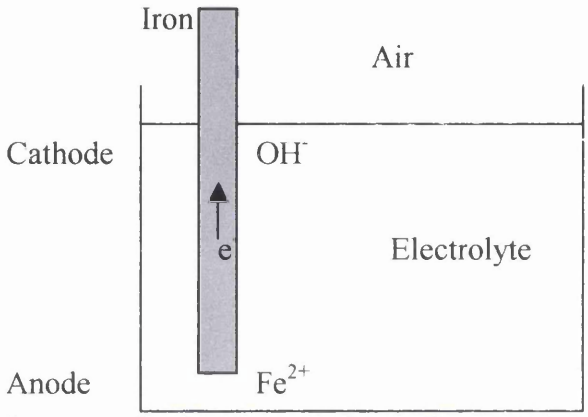

Figure 2.1. Schematic diagram of a simple corrosion cell.

In figure 2.1 atmospheric oxygen will dissolve in the liquid electrolyte so the iron just beneath the surface will experience an increased dissolved oxygen content and will thus act as a cathode. The bottom of the specimen, furthest removed from the surface, will experience a lower dissolved oxygen content and thus act as an anode. Fe^{2+} ions will thus pass into solution as described by equation 2.1 and the metal will corrode. Electrons will pass up the specimen and discharge near the surface where OH^- ions will form in the electrolyte as described by equation 2.2. Diffusion will occur in the liquid over a period of time and the Fe^{2+} ions and the OH^- ions will interact to form an iron hydroxide, better known as rust (Martin, 1996).

Protection from corrosion can take many forms but all varieties use the same principle, without a cathode, an anode, electrolyte or a flow of electrons corrosion cannot take place.

One such method of corrosion prevention is through soluble inhibitors where the liquid is treated with a reagent that removes oxygen from the solution or forms a passive film over the metal thus stifling the attack. However, this method is only viable in closed systems where the liquid is constantly recirculated and not continually exposed to the atmosphere. (Martin, 1996)

The use of paints and lacquers helps to prevent corrosion by excluding water and air from the surface of the metal. However, any breach of the painted surface can leave the metal exposed to the environment and the subject of rapid corrosion.

Another anti-corrosion technique is cathodic protection that can take two forms. The first method is impressed current protection whereby the metal is connected to the negative terminal of a suitable DC source and an inert metal anode placed nearby. The second method is through sacrificial protection whereby a more reactive metal, such as zinc, is connected electrically to the steel. In this instance the more reactive metal will corrode preferentially leaving the less reactive metal unaffected (Martin, 1996).

Sacrificial protection using zinc has become one of the most widely used methods of protecting steel because it offers good sacrificial protection at a relatively low cost. Under normal environmental conditions zinc also forms a passive layer over itself, leading to a reduced rate corrosion of the zinc layer and the added bonus of being able to 'heal' any minor scratches by the formation of zinc oxides as illustrated in figure 2.2.

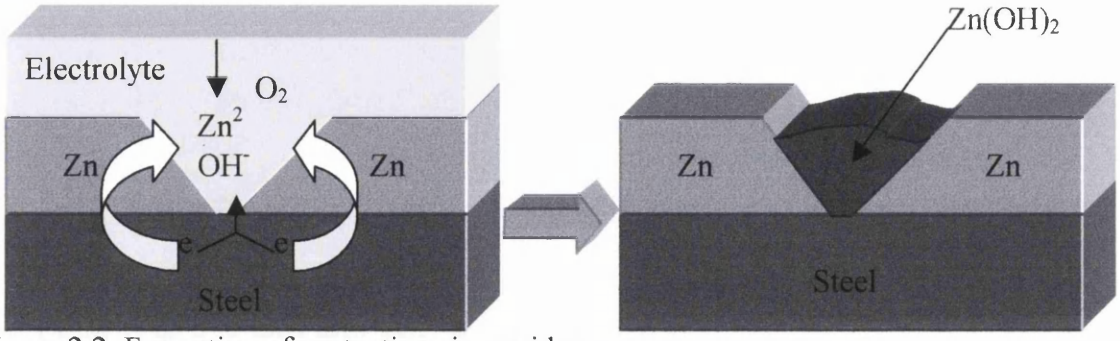

Figure 2.2. Formation of protective zinc oxides.

Therefore, despite the thermodynamic driving force encouraging the corrosion of a steel substrate the application of a zinc coating can help to protect the steel and prevent rusting by offering both galvanic and barrier protection. Consequently, the application of a zinc coating to a steel substrate has become one of the most widely used techniques for preventing the corrosion of steel.

2.3 PRODUCTION OF ZINC COATED PRODUCTS

The application of a zinc coating occurs primarily in one of two ways, either by hot dip galvanising as illustrated in figure 2.3 or by electroplating as illustrated in figure 2.4. Both processes involve a continuous production cycle whereby the coils of steel are welded end to end as they pass through the line. To facilitate this, production lines have accumulators that release or take up extra strip as required when the coils enter or exit the line.

In hot dip galvanising, reducing furnaces heat the steel strip to increase the ductility of the strip by encouraging recovery and recrystallisation of the cold rolled substrate. The strip is also heated to activate and clean the surface so that wetting of the steel by the liquid zinc is unhindered and contamination of the zinc pot by iron fines is reduced to a minimum. Subsequent dipping into the pot of molten zinc coats the steel, upon removal from the bath air knives remove any excess zinc so that a coating of approximately 7-10μm thick is achieved. Cooling of the strip then takes place before subsequent processes such as skin pass rolling, cleaning, and chromating are carried

out. The strip then passes through an inspection area before being recoiled and packed.

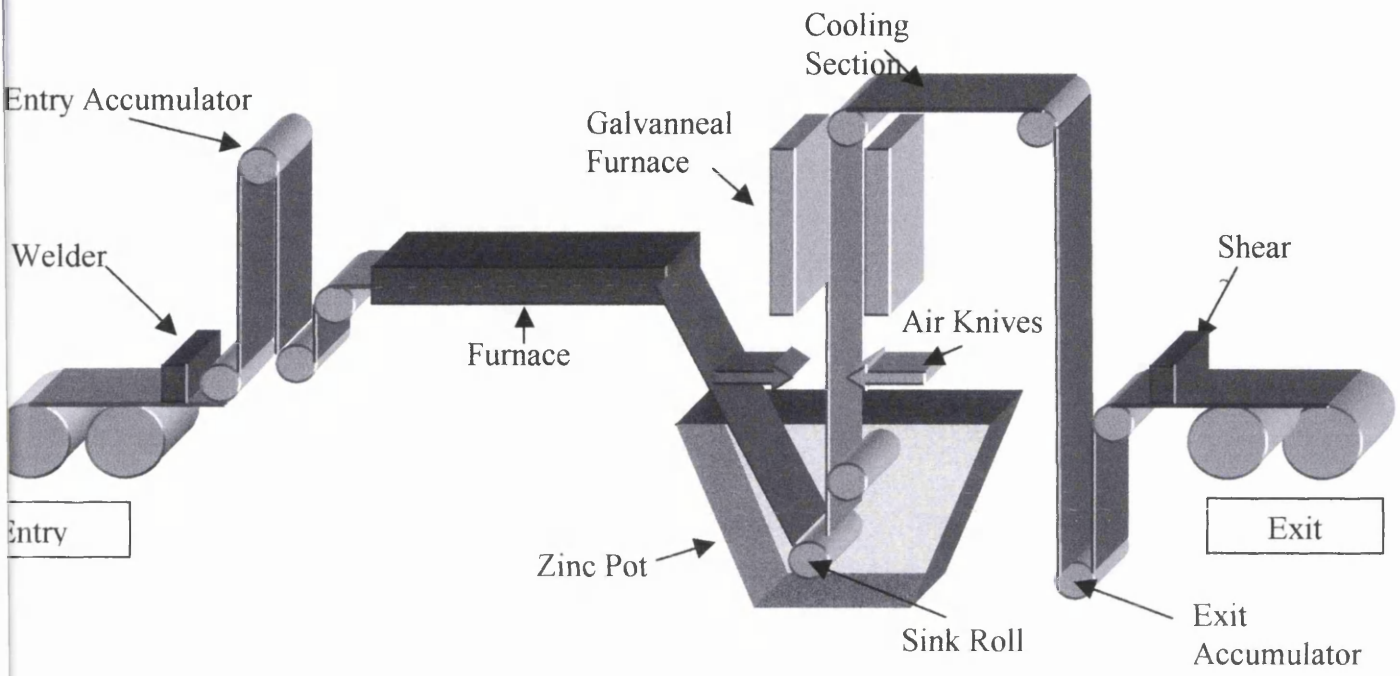

Figure 2.3. Schematic diagram of a continuous hot dip galvanising line.

In electroplating, the strip passes through numerous baths of electrolyte. An electric potential applied across the strip causes the zinc dissolved in the electrolyte to plate onto the strip. Coatings of 2-3μms in thickness are produced for domestic appliance products and up to 7μm for automotive products.

For long life in use, whether for domestic appliances, automotive products or contstruction two areas in zinc steel processing need close attention - paintability and weldability. In terms of paintability, zinc does not allow easy wetting or adherence of paint to its surface unless subsequent pre-treatments are carried out (De Cooman *et al.*, 1998). In terms of weldability the zinc reacts with the copper spot electrodes used to attach the exterior panels to the frame of the car body. The result is rapid alloying of the electrode to form brass and the subsequent deterioration of weld quality and electrode life (Holliday *et al.*, 1996).

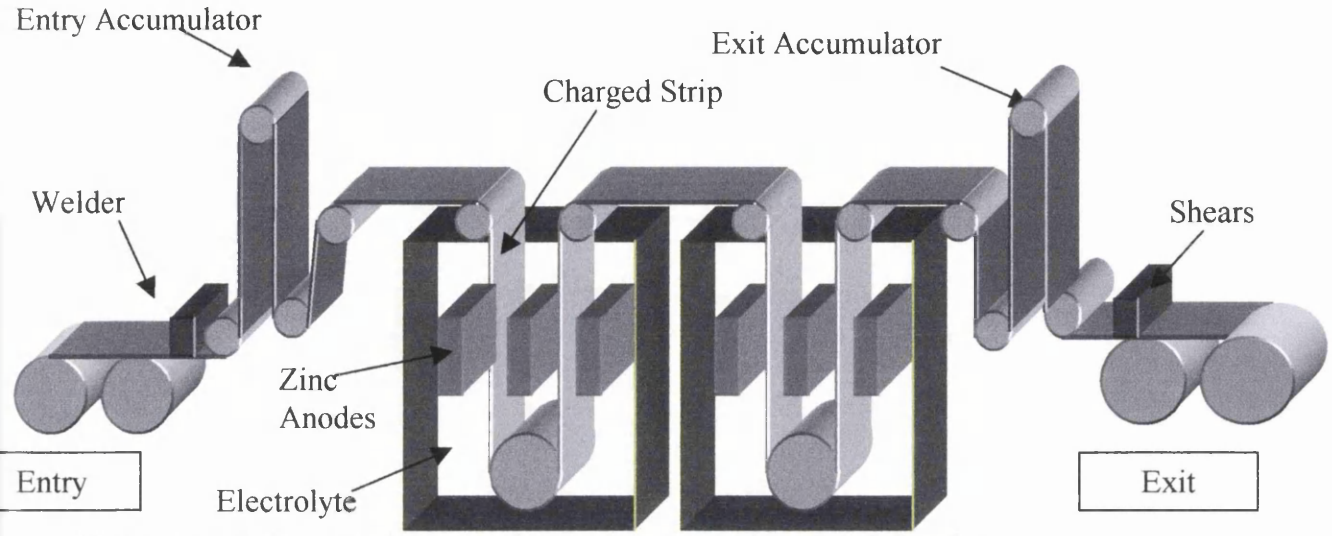

Figure 2.4. Schematic diagram of a continuous electrogalvanising line.

Consequently, the use of galvanised steel for exterior body parts presents many problems to the car manufacturer. Hot dip galvanised steel is cheap and has good corrosion resistance but suffers from poor paintability, weldability and surface feature defects. Electroplated galvanised steel has better paintability but at a much higher cost. The solution to this problem in part comes from the use of the galvanneal coating.

2.4 THE GALVANNEAL COATING

Interdiffusion of the iron and zinc atoms should occur as a result of the elevated temperatures of about 460°C within the zinc pot and the intimate contact between the molten zinc and the steel substrate. However, under normal galvanising conditions, a small amount of aluminium (approximately 0.135wt%Al_{eff}) added to the zinc bath forms a thin inhibition layer of Fe_2Al_5 between the zinc and the iron substrate. This prevents the interdiffusion of the iron and zinc atoms resulting in a coating consisting mainly of pure zinc, figure 2.5.

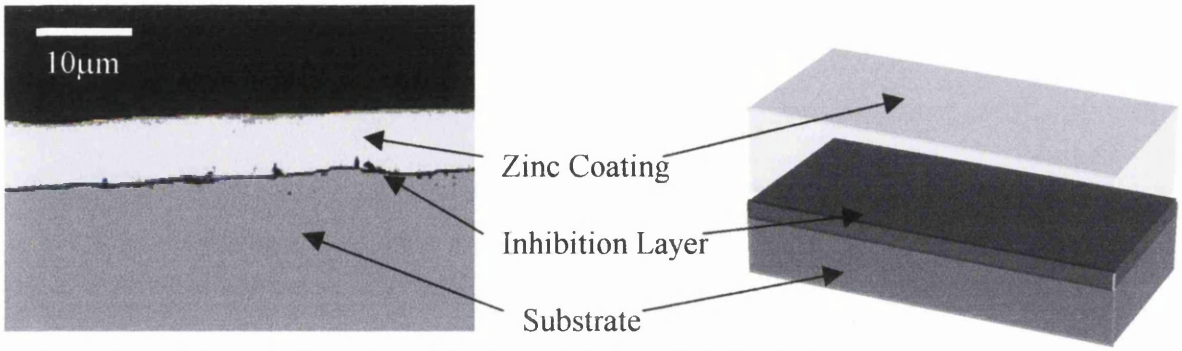

Figure 2.5. Optical image of a zinc coating and a schematic diagram

In the galvanneal process, reduction of the aluminium content in the zinc bath to approximately 0.108wt%Al_{eff} means that the inhibition layer that does form is not as stable. Subsequent heating at a temperature of between 490-510°C for about ten seconds causes the interdiffusion of the iron and zinc atoms and the formation of several alloy layers (Inagaki *et al.*, 1991), figure 2.6.

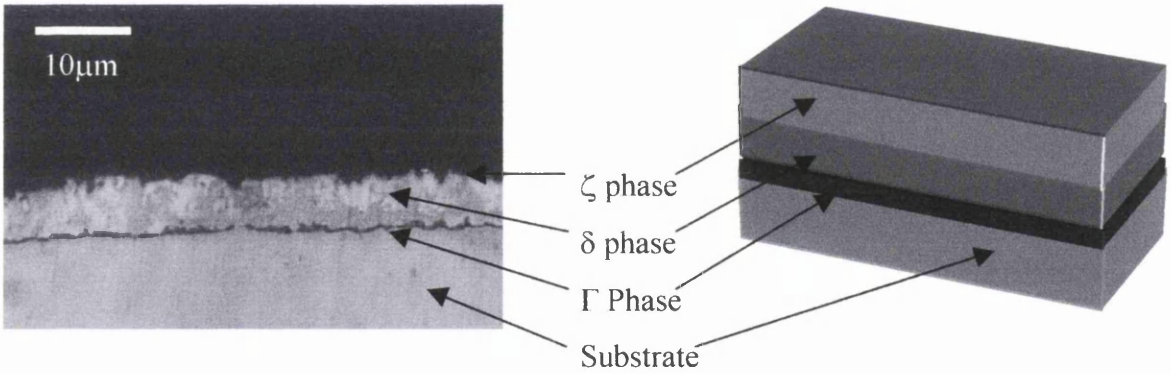

Figure 2.6. Optical image of the galvanneal coating and a schematic diagram

This alloy layer contains about 10wt% iron and has the effect of greatly improving the paintability, weldability and corrosion resistance of the product. Paintability is improved as a result of the surface micro-roughness that occurs due to the alloying process, this enables the paint to key with the surface more easily. The weldability is improved due to the reduced amount of zinc that is present at the surface and the increased melting point of the surface phases. Both of these lead to reduced wear on the copper electrodes.

However, the way in which the galvanneal coating is produced means that there are different intermetallic phases present within the coating. When subjected to stresses and strains such as those experienced in the forming operation each of the different phases behaves in a unique and individual manner. This may result in powdering or flaking of the coating as discussed later in section 2.6.

2.5 GROWTH OF THE GALVANNEAL COATING

The galvannealing process involves the non-equilibrium isothermal solidification of iron-zinc phases by the atomic diffusion of iron atoms from an effectively infinite source. Consequently, many different studies conducted on the coating development have enabled us to achieve an understanding of this complex process. The work of McDevitt *et al.*(1998) divided the process into four main areas:

1. Formation of the Fe-Al layer.
2. Breakdown of the Fe-Al layer.
3. Solidification of coating by δ formation.
4. Growth of Fe-rich phases via diffusion.

The aluminium in the bath has a much higher affinity with iron than it does with zinc and results in a thin inhibition layer of iron and aluminium forming on the substrate surface (Isobe *et al,*, 1992, McDevitt *et al.* 1998). After approximately one second of immersion in the bath, Fe_2Al_5 and FeAl cover about 80% of the substrate surface. However, because the inhibition layer does not form instantaneously and because the surface is not completely covered, the zinc near the substrate has some iron dissolved in it. Iron-zinc phases can now form and McDevitt *et al.* (1998) and Tang and Adams (1993) observed clusters of δ and ζ dispersed between the inhibition layer, figure 2.7. After approximately three seconds the FeAl layer has disappeared leaving just the Fe_2Al_5 behind which has now grown to cover approximately 95% of the substrate. Both ζ and η were observed as well as a 0.1μm thick layer of Γ_1 on top of the inhibition layer. The final microstructure of the inhibition layer is that of colonies of

Fe_2Al_5 with both high and low angle grain boundaries separating them. Guttmann *et al.* (1995) showed that large portions of the Fe_2Al_5 nucleate with strong orientation relationships with respect to the substrate and several different colonies may exist within the area of a single substrate grain. They also suggested that the inhibition layer consisted of an upper layer with a random orientation and a lower layer with an ordered orientation. The formation of the inhibition layer is highly dependent upon the aluminium content of the bath and the thickness has been observed to vary from approximately 30 to 300nm (McDevitt *et al.*, 1997).

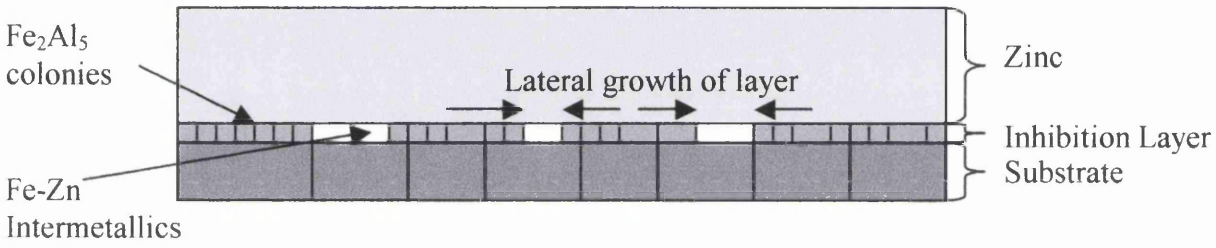

Figure 2.7. Schematic diagram of the initial formation of the inhibition layer.

Upon leaving the bath and entering the galvanneal furnace, the inhibition layer begins to breakdown and Fe-Zn phases begin to form. Two main theories exist about the nature of this breakdown process. The first one proposed by McDevitt *et al.* (1997) suggests that the inhibition layer dissolves and diffuses into the steel substrate. Experiments showing significant amounts of aluminium in the steel grain boundaries help to support this. The other theory suggested by Guttmann *et al.* (1995) proposes that the inhibition layer is broken apart by the formation of Fe-Zn intermetallics beneath the inhibition layer. In actual fact, both theories may be correct depending upon the thickness of the inhibition layer. When the inhibition layer is thin, dissolution could occur before mechanical breakage can take effect, yet when the inhibition layer is thick dissolution is not quick enough and so mechanical breakage occurs.

The exact process by which the inhibition layer forms and is subsequently broken down is still under much debate and much work still needs to be done to arrive at a definitive explanation. However, by whatever mechanism the inhibition layer breaks down the overall outcome is the formation of Fe-Zn intermetallic compounds. Most

experts agree that these Fe-Zn intermetallic compounds occur by the formation of 'outburst' structures at steel grain boundaries that are emerging at the surface of the steel (Kim and Chung, 1998). The high angle boundaries within the Fe-Al layer act as quick diffusion paths through which the zinc can move and react with the iron in the substrate, figure 2.8. (Guttmann, 1995).

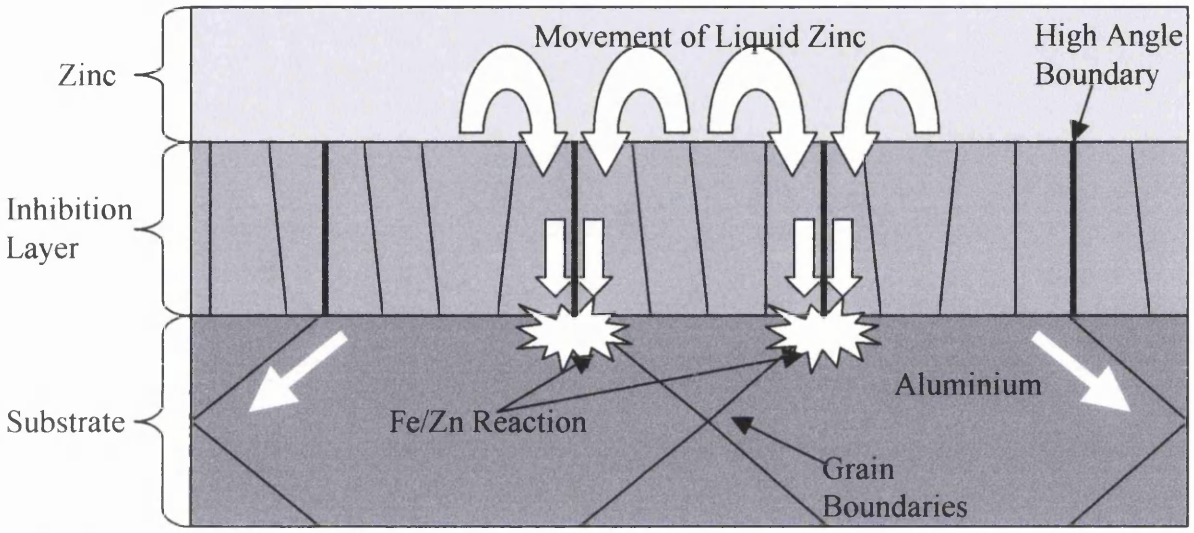

Figure 2.8. Schematic diagram of the formation of outbursts.

Guttmann *et al.* (1995) suggested that by using this path, zinc could diffuse cross a 70nm thick Fe_2Al_5 layer in one second.

When the Fe/Zn reaction takes place, the remaining inhibition layer will be mechanically broken off. Further evidence supporting this hypothesis is demonstrated by the work of Stevenson (1998), who showed that there is a high aluminium concentration at the outburst front.

At 500°C and below, the equilibrium phase diagram predicts that the ζ phase should be the first phase to form as the iron diffuses into the coating. However, experimental evidence shows that it is the δ phase that forms first and propagates through the coating. As demonstrated by Kawaguchi and Hirose (1993) an increase in aluminium content has the effect of reducing the peritectic transformation temperature and making δ the stable phase. From the work of Stevenson (1998), we know that there is an increase in aluminium content ahead of the outburst front. The author therefore postulates that this may result in the lowering of the peritectic temperature and result

in δ crystal formation. Further support of this is given by Jordan *et al.* (1998) who showed that the growth rate constant for δ increased with increasing aluminium content.

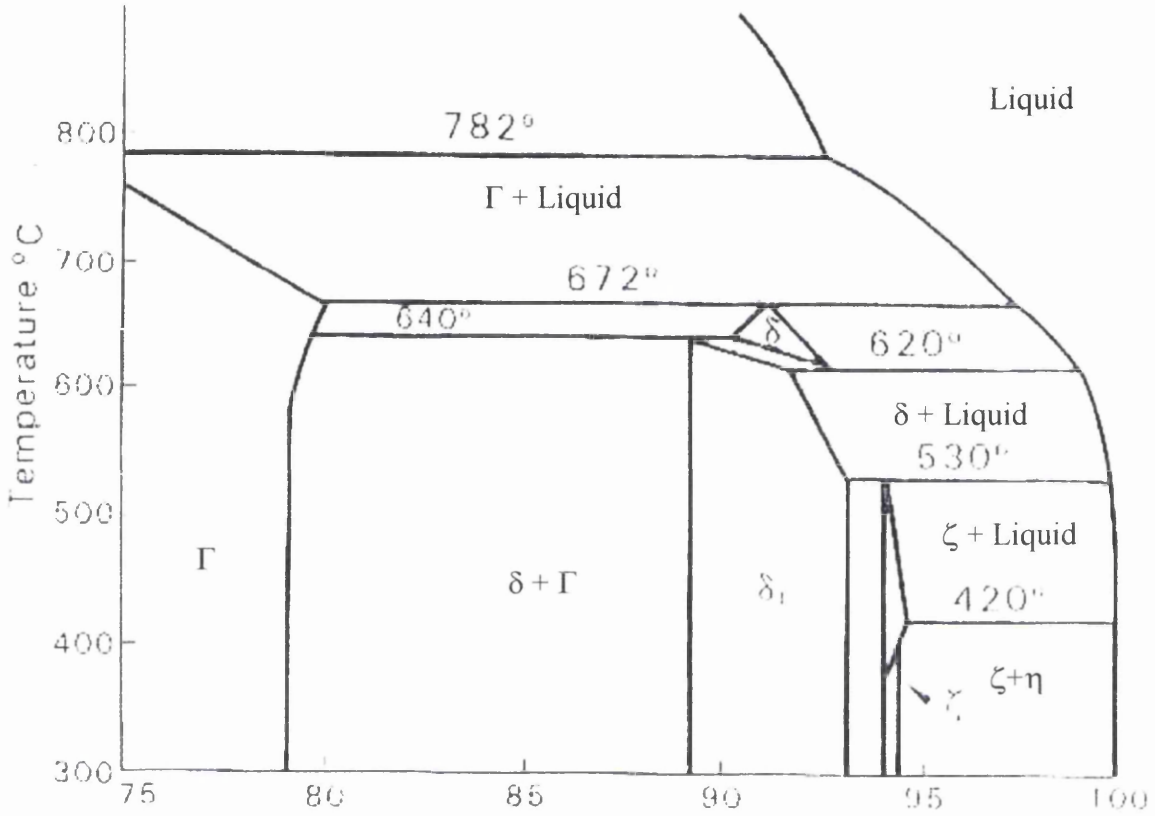

Figure 2.9. Iron zinc equilibrium phase diagram.

Because of the iron concentration gradient that exists between the substrate and the coating, as heating continues, more and more iron diffuses into the coating. This results in further growth of the δ phase and the development of the Γ phase at the coating substrate interface (Foct *et al.*, 1993). On an industrial line, the design of the galvannealing process is such that it finishes when the coating has an iron content of approximately 10wt% and the δ phase is dominant at the surface. The overall resultant coating makeup is essentially determined by the customers needs and desires but generally consists of the δ phase with some ζ phase at the surface and a 0.5μm thick Γ phase at the substrate. The different phases are shown below in table 1.1 along with the Vickers Hardness value as determined by Fujii *et al.* (2000).

Table 1.1. Different phases present within the galvanneal coating.

PHASE	STRUCTURE	WT% FE	AT% FE	HARDNESS (HV)
Eta (η)	Hexagonal	0	0	52
Zeta (ζ)	Monoclinic	5.9-6.3	6.8-7.2	200
Delta (δ)	Hexagonal	7.2-11.4	8.3-13.0	284-300
Gamma$_1$ (Γ_1)	FCC	17.1-19.6	19.4-22.2	505
Gamma (Γ)	BCC	22.0-27.6	24.8-30.9	326

It is clear to see from the table that when subjected to the same force each of the phases will behave in its own unique manner. The result is a build up of internal stresses leading to cracking and powdering of the coating.

2.6 MECHANISMS OF POWDERING AND FLAKING

Powdering and flaking occurs when the galvanneal coating becomes detached from the steel substrate. Flaking occurs by failure at the Γ/substrate interface and results in thin flakes of coating approximately the coating thickness in length. Powdering occurs by failure within the δ layer and leads to very fine particles of the coating being removed (Urai *et al.*, 1999). Both powdering and flaking are major concerns of galvanneal users for two main reasons; firstly, the loss of coating leads to reduced corrosion resistance and secondly any coating that comes off may get trapped in the presses leading to increased tool maintenance and fluctuating friction. The reason for coating failure is that as the solute within an alloy changes then so do the mechanical properties of that alloy (Jordan *et al.*, 1992, Mataigne *et al.*, 1995). The best example is that of steel, whereby variations of carbon content within the steel dramatically alter the mechanical properties and phases present. In the same way varying amounts of iron within the zinc coating can change the mechanical properties and phases present.

Therefore, the main cause behind the powdering and flaking of galvanneal coatings is the reduction in ductility due to the increased iron content within the coating (Zhong *et al.* 1998). This means that when subjected to deformation the coating cannot

accommodate the strain imposed upon it and therefore must crack to relieve the stress (Foct, 1992). The exact nature of this cracking is dependent upon the type and speed of deformation.

Zhong *et al.* (1998) demonstrated that under a shear stress the galvanneal coating tended to fail by flaking whereas under tensile or compressive stresses the tendency was for powder failure. Urai *et al.* (1999) looked at the deformation speed and found that at high deformation rates the layer exfoliated at the interface between the Γ layer and the steel substrate. At lower deformation rates the coating exfoliated in the middle of the δ layer. In general, as the forming speed increased the amount of exfoliation increased (Rangarajan, 1997) and the mode of exfoliation moved from powdering to flaking.

The reason behind this, as proposed by Arimura *et al.* (1995) and Urai *et al.* (1999), is that the deformation mode of the base steel differs depending upon the forming speed. At low forming speeds, there is uniform elongation and therefore the stresses imposed upon the coating (especially at the coating/steel interface) are less harsh resulting in less exfoliation. At high forming speed, the elongation becomes non-uniform resulting in much harsher deformation conditions and greater amounts of exfoliation.

Deits *et al.* (1990) proposed that the actual crack formation and propagation under imposed tensile strains occurred in three stages. In the first stage, the substrate deforms and the coating cannot accommodate the stresses. Cracks start from the coating/steel interface and propagate towards the surface through weak areas in the coating to relieve the internal stresses. Finally, the cracks then propagate along the interface in a further attempt to relieve the stresses placed on the coating, figure 2.10.

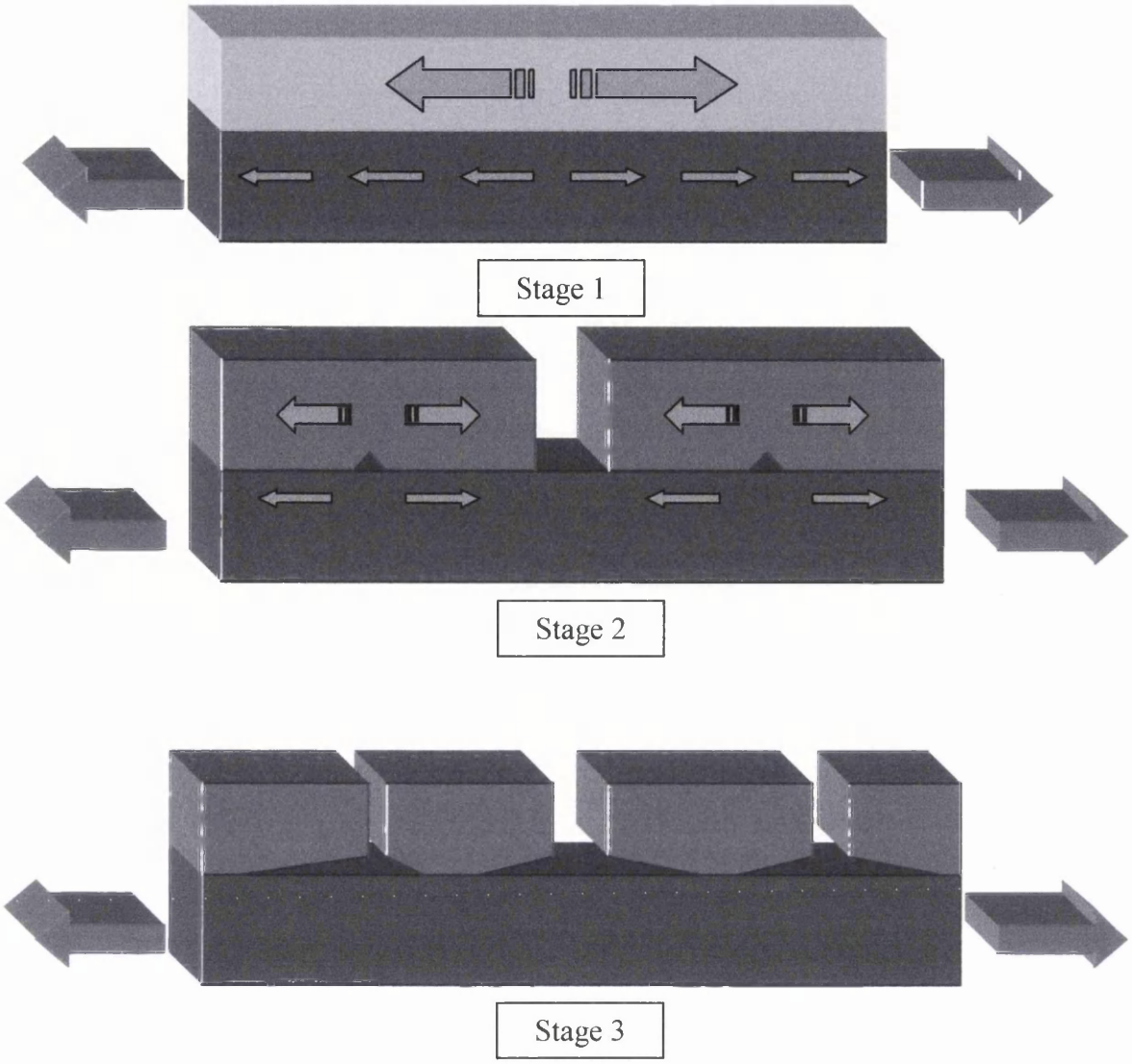

Figure 2.10. Mechanism of coating failure under tensile strain conditions.

Therefore, powdering resistance is lowest when there is a high iron content within the coating and a thick Γ layer. Together they increase the coating brittleness and encourage easy crack propagation along the coating/steel interface.

Urai *et al.* (1996) used coatings with similar iron contents and showed that when the aluminium content within the bath increased from 0.05-0.16wt%Al_{eff} the amount of powdering decreased from 8mg to 1mg. The reason they proposed for this was that as the aluminium content increased then so did the thickness of the Fe-Al inhibition layer. Therefore, in the bath with the high Al content, the alloying reaction occurs

heterogeneously and the coating has a mixed structure of both δ and ζ phases. Upon deformation, the ζ phase deforms preferentially and relaxes some of the stresses that build up in the coating. Ito (1977) also confirmed this and stated that powdering was suppressed by an increase in the ratio of ζ to δ within the coating.

However, from a commercial point of view the thicker Fe-Al layer results in slower diffusion of iron resulting in longer processing times and a reduced production rate. It should also be noted that the work carried out by Urai *et al.* (1996) used high coating weights of $100g/m^2$ and may therefore not be a correct representation of commercial galvanneal products.

2.7 THE EFFECT OF SUBSTRATE CHEMISTRY UPON THE GALVANNEALING REACTION

Solute atoms are present within the steel either because of deliberate additions or as a result of the iron and steel making process. For example, carbon, sulphur and nitrogen are present as a result of the iron and steel making progress whereas phosphorous and niobium are deliberately added to increase the yield strength of the steel.

However, in terms of the development of the galvanneal coatings, interstitial solute atoms will either collect at grain boundaries and hinder the alloying reaction or remove atoms from the grain boundaries and promote the alloying reaction.

The addition of titanium to the steel substrate results in the formation of carbides and nitrides within the iron lattice. This has the effect of removing the carbon from the iron lattice thus making dislocation movement easier and increasing the ductility of the steel. In terms of the development of the galvanneal coating, titanium has the effect of removing carbon atoms from the grain boundaries thus making them far more reactive. Consequently, the alloying reaction occurs at an increased rate when high concentrations of titanium are present within the substrate (Jordan and Marder, 1998).

However, some steels have all of the aforementioned solute atoms present in varying amounts. Toki (1994) therefore produced a formula that would predict the reactivity of the grain boundaries depending upon the solutes present.

$$Ti^{**} = Ti - 3.99C - 1.49S - 3.42N - 1.55P \quad (2.3)$$

Where:

Ti = Wt% titanium

C = Wt% carbon

S = Wt% sulphur

N = Wt% nitrogen

P = Wt% phosphorous

If Ti^{**} is positive then there is excess titanium and the grain boundaries are more reactive resulting in the fastest growth rates of the Fe-Zn alloy. If Ti^{**} is negative then not all the C, N, S or P is tied up and thus the grain boundaries are blocked (Coffin and Thompson, 1995). Toki (1994) showed that as the Ti** value became positive there was a rapid increase of iron in the coating for a given galvanneal time. They also showed that with Ti-added steels (Ti** > 0) that the effect of the grain size upon the reaction was quite large.

This increased reactivity, according to Jordan and Marder (1998), only affects the Γ layer growth, as it is this phase that is primarily controlled by interface diffusion. Jordan and Marder (1998) showed that when Ti^{**} was positive the growth rate constant was clearly higher for the Γ phase but stayed constant for the other phases. Their work also showed that the solute additions had no effect upon the inhibition layer growth and that outburst formation corresponded to the location of substrate grain boundaries.

Just how this relates to powdering was analysed by Zhong *et al.* in 1998. They found that with low iron content coatings, and when the phosphorous or carbon content was high, the bonding strength of the coating to the substrate increased and failure occurred mainly by powdering. However, the addition of Ti had the effect of

reducing bonding strength leading to the failure of the coating by flaking. This may be attributed to an increase in the growth rate constant of the brittle Γ phase as shown by Jordan and Marder, (1998). Overall, through the use of a U channel test, they showed that both the ductility and the interfacial bonding strength of the coating affected the powdering performance. With a low bonding strength, performance was poor regardless of the ductility, whereas, with a high bonding strength the performance was highly dependent upon coating ductility.

2.8 SURFACE FEATURES

The surface of the galvanneal coating is one of the most vital aspects of the galvanneal product. It is the surface that will be exposed to the presses when the steel is formed; it is the surface that will be in contact with the electrodes when the steel is welded and it is the surface that the paint will be in contact with when the steel is painted.

Both ζ and δ can be present at the surface of the galvanneal product and the relative amounts of each phase is determined by the conditions of the galvannealing process. For example, a short galvanneal time and/or unreactive steel may result in large amounts of ζ and η on the surface and the presence of very little or no δ.

2.8.1 Surface Appearance

The work of De Cooman *et al.* (1998) shows that the appearance index, a measure of the surface quality of a sample after it has been painted, is as low as 60% when the coating consists of 20% ζ. The appearance index then rises to about 90% (similar to that of electroplated steel) when the iron content reaches approximately 10wt% and there is between 0-10% ζ. This shows that the presence of the ζ phase at the surface is detrimental to the surface quality of the galvanneal product and that further alloying of the coating helps to improve this. De Cooman *et al.* (1998) also demonstrated that in the absence of outbursts the surface is smoother than the underlying substrate due

to the ability of the zinc to mask some substrate surface features. Furthermore, the emergence of outbursts generates large profile waviness due to the flow of liquid zinc that in turn leads to a very poor visual appearance. Therefore, overall they showed that the presence of the ζ phase within the coating and at the surface results in poor paintability characteristics for the customer.

2.8.2 Formability

The forming operation involves an intimate reaction between the die, the punch, the steel substrate and the coating surface. Previous work has shown that both the steel/coating interface and the coating structure play an important roll in this process. In terms of the surface, two parameters are important, the friction and the roughness. The work of Inagaki *et al.* (1991), Kato *et al.* (1993) and Rangarajan (1997) showed that the amount of ζ phase at the surface greatly affects the frictional coefficient of the galvanneal product. The reason for this is that the higher coefficient of friction of the ζ phase compared to that of the δ phase resulted in the 'sticking' of the steel sheet to the press. However, it should be emphasised that the actual value of the coefficient of friction is not as important as a value that does not fluctuate wildly from sample to sample. The addition of lubricants during pressing will greatly reduce the amount of 'sticking' that occurs (Elliot, 1999 and Kunde *et al.*, 1998), but the amount of lubricant that needs to be added is highly dependent upon the coefficient of friction of the material. Therefore, a customer will want the surface to contain consistent amounts of ζ and δ for a good pressing operation although less ζ would ultimately result in less lubrication being required.

2.8.3 Roughness

Four main features define the roughness of a galvanneal coating, the formation of Fe/Zn phases, emergence of ζ crystals, exaggeration of topographical features and craters (Scheers *et al.*, 1996). The same principle holds with the roughness of the material as it did with the frictional coefficient. The addition of lubricants and the performance during pressing is dependent upon the roughness of the material; a

customer will therefore want a material with constant roughness so that press forming conditions will be constant from one pressing to the next. In terms of ζ and δ the product should have consistent amounts of both, although preferably there would be less ζ so as to reduce the amount of lubrication required for each operation.

2.8.4 Weldability

The weldability of the galvanneal product is determined by the amount of wear that the copper electrode experiences during the spot welding process. The ζ phase has a much lower melting point than the δ phase and causes much more rapid brassing of the copper electrodes. This in turn leads to an increase in both the brittleness of the electrode and the amount of current that must be applied to create a certain weld size. Therefore, in terms of weldability from a customer's point of view, it is preferential to have a greater percent of δ on the surface (Mataigne *et al.*, 1995).

It is clear to see that the presence of the ζ phase on the surface is detrimental to the galvanneal product in terms of surface appearance, weldability, friction and roughness. However, as stated earlier in section 2.6, the softer ζ phase helps to reduce powdering by relieving internal stresses and is therefore beneficial from the point of powdering resistance.

2.9 CRATER FORMATION, GROWTH AND EFFECT

As mentioned previously in section 2.8.3 the surface roughness of the galvanneal coating has an effect upon the formability characteristics of the galvanneal product. One of the main influences on roughness is the presence of craters.

The thickness of the galvanneal coatings varies quite considerably as a result of the alloying reaction that occurs. In some places, gaps in the coating extend almost the full way through the coating and have an ordered layer of ζ crystals at their base

(McDevitt and Meshii, 1998); known as craters they are a unique feature of the galvanneal product.

Their presence has the immediate effect of increasing the roughness of the surface of the galvanneal product and, as proposed by Carless *et al.* (1998), reduce powdering. Essentially, craters form due to the preferential nucleation of ζ crystals on specifically oriented ferrite grains and result in a barrier to the formation of the normal galvanneal coating.

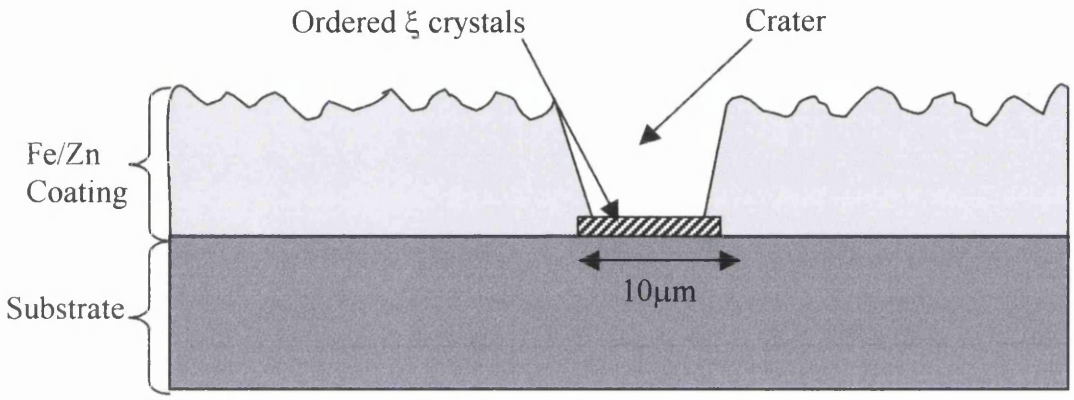

Figure 2.11. Schematic diagram of a galvanneal crater.

2.9.1 Proposed Mechanism of Formation of the Galvanneal Crater

Tang *et al.* (1998) reported that the formation of Fe/Zn intermetallics on the surface of the strip involves a four-step process:

1. Iron atoms separate from the strip
2. Zinc atoms separate from each other
3. Iron atoms mix with the zinc atoms
4. Iron and zinc phases nucleate on the surface of the strip

The energy barrier for the separation of iron atoms from the strip is approximately equal to the free energy of fusion (ΔG_f) as described below in equation 2.4:

$$\Delta G_f = 15200 - 8.4T \quad (2.4)$$

where:

T = Temperature in Kelvin

Therefore, the probability of an Fe atom escaping from the surface (P):

$$P = \frac{1}{6} \times \exp\left(\frac{-\Delta G}{RT}\right) \quad (2.5)$$

where:

ΔG = Free Energy of Fusion

R = Molar Gas Constant

T = Temperature in Kelvin

Using these equations Tang (1998) predicted that the iron content near the strip would be approximately 3.0wt%.

Tang (1998) also looked at the enrichment of the aluminium content near the strip and suggested that it increased by a factor of 200 times at 460°C resulting in 84% of the atomic sites being occupied by aluminium atoms. Therefore, because aluminium and zinc atoms repel each other in the liquid this Al segregation not only affects density of potential nucleation sites for Fe/Zn intermetallics, but also the activity of them at the interface.

Tang (1998) reported a transition point of 0.134wt%Al_{eff} in the bath. Above this concentration the nucleation of Fe/Al on the strip surface is favourable whereas below this point the formation of Fe/Zn intermetallics is favourable. However, the exact nature of these intermetallics is dependent on several factors. When the aluminium level is higher than 0.1wt%Al_{eff} the δ phase becomes the thermodynamically favoured phase. Yet it has been widely reported that the ζ phase frequently grows epitaxially on the surface of the strip. The reason for this, as reported by Tang *et* al. (1998) is threefold. Firstly, the iron solubility sustained by the metastable ζ phase is very much the same as the equilibrium iron solubility determined by the liquid+δ phase.

Secondly, the driving force for the formation of both phases is similar and thirdly the ζ phase can grow epitaxially on the steel substrate whereas the δ phase cannot. Epitaxial nucleation occurs when the atoms within the nucleating phase and the substrate are arranged in such a way that the misalignment between them is very small. This results in a very small amount of energy required to create the new interface and the likelihood of a very small energy barrier to the nucleation of the new phase. In the case of the nucleating ζ phase the grains of the underlying substrate must be oriented with {111} in the plane of the sheet (Nakamori *et al.*, 1995).

What this means is that although the δ phase is the equilibrium phase (Tang, 1996), the ζ phase is thermodynamically permissible and kinetically favourable under epitaxial nucleation. In terms of surface energies and classic nucleation theory, the critical radius for epitaxial nucleation for the ζ phase is only $3.3x10^{-10}$m, which is smaller than the dimension of a unit cell of ζ phase. Therefore, the energy barrier for formation of the ζ phase under epitaxial nucleation is only $1.12x10^{-20}$J (Tang *et al.* 1998).

However, for the ζ phase to grow epitaxially the steel grains must be oriented with {111} in the plane of the sheet. The random δ phase will be able to nucleate preferentially on non-{111} grains and thus a mixture of δ and ζ will be found on the surface of the strip.

When the aluminium content is in the range 0.135-0.15wt%Al_{eff} metastable Fe/Zn intermetallics of mainly ζ crystals are observed. The reason for this is that initially the aluminium atoms contiguous to the interface facilitate the growth of the Fe-Al layer. Consumption of these atoms requires long-range diffusion through the liquid before further growth can take place. Therefore, because the ζ phase can nucleate very easily under epitaxial conditions the formation of ζ crystals is still kinetically possible. Above 0.15wt%Al_{eff} the nucleation of the ζ phase is no longer kinetically or thermodynamically possible as a complete inhibition layer is formed.

Therefore, in summary so far, the reaction at the substrate/liquid interface involves the formation of the Fe-Al layer, the δ phase and the ζ phase. When the effective aluminium is between 0.1 and 0.135wt%Al_{eff} the aluminium concentration is not high enough to cover all the potential nucleation sites and so the ζ and δ phases can nucleate. Above 0.1wt%Al_{eff} the δ phase has the lowest energy barrier to nucleation and will therefore nucleate preferentially. However, the ζ phase has the ability to rapidly nucleate on grains oriented with {111} in the plane of the sheet due to the even lower energy barrier. Overall, the initial layer laid down will be a mixture of Fe-Al phase, δ phase and ζ phase as illustrated below in figure 2.12.

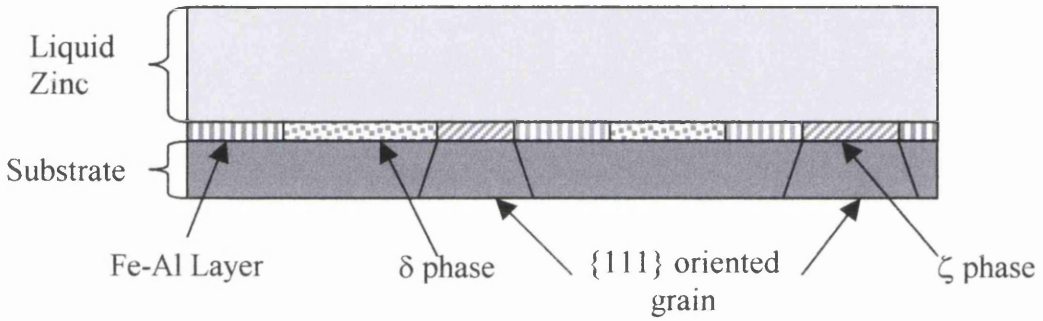

Figure 2.12. Schematic diagram of the initial layer makeup.

When the aluminium content is between 0.135 to 0.15wt%Al_{eff} there is a high enough aluminium content for the Fe-Al layer to cover the majority of the potential nucleation sites. However, the supply of aluminium atoms occurs by long-range diffusion through the liquid and will therefore take its time. Consequently, although it will be able to rapidly lay down a thin inhibition layer the actual growth will take longer. As reported by Guttmann *et al.* (1995) the inhibition layer has an orientation relationship with the substrate and therefore whilst the Fe-Al layer is thin and growing the ζ phase can still rapidly nucleate on grains oriented with {111} in the plane of the sheet. The δ phase does not have this ability of rapid nucleation and is therefore not likely to be present within the initial layer makeup.

Above 0.15wt%Al_{eff} the Fe-Al layer has rapidly covered all of the potential nucleation sites and the nucleation of either the ζ or the δ phase is not possible.

2.9.2 Development and Growth of the Galvanneal Crater

When the strip is galvannealed after dipping, the formation of the Fe/Zn layer will proceed by the processes described previously in section 2.5. However, where the ζ phase has nucleated in an ordered fashion on oriented grains the situation is not as straightforward. Essentially, because of the similar driving forces, the ζ phase should grow at a rate comparative to that of the δ phase and yet it has been observed that only a 1-2μm thick layer of ζ crystals grows during the galvannealing process. One reason proposed by Guttmann *et al.* (1995) suggested that it was due to the 'peculiar grain boundary structure of the ζ phase and the incidence of the atomic structure of the $\alpha_{ferrite}/\zeta$ interface'. Guttmann *et al.* (1995) did not go on to explain clearly what they mean by this or the overall effect that this may have upon crater formation.

However, work done by Inagaki *et al.* (1995) showed that when the aluminium content of the bath was 0.15wt%Al_{eff}, a thin Fe-Al layer was present below the ordered ζ crystals after galvannealing. It is suggested that this thin inhibition layer would restrict the diffusion of iron atoms into the ζ crystals thus retarding their growth. Diffusion through the ζ crystals may also be such that the iron concentration would never be high enough to nucleate the δ phase. The ζ crystals may possibly then act to protect the inhibition layer from the liquid zinc and because formation takes place on grains and not over grain boundaries diffusion into the substrate would be minimal. The exact process by which craters develop is poorly understood and investigative work in this area is almost non-existent.

The final crater consists of an area void of coating with ordered ζ crystals at the base. Below the ordered crystals there may be a very thin inhibition layer and below this a plateau of substrate. The plateau forms because the zinc is not able to diffuse into the substrate and therefore does not transform it to an Fe/Zn alloy. A cross section of an actual crater and an SEM image are shown in the figures 2.13 and 2.14 respectively.

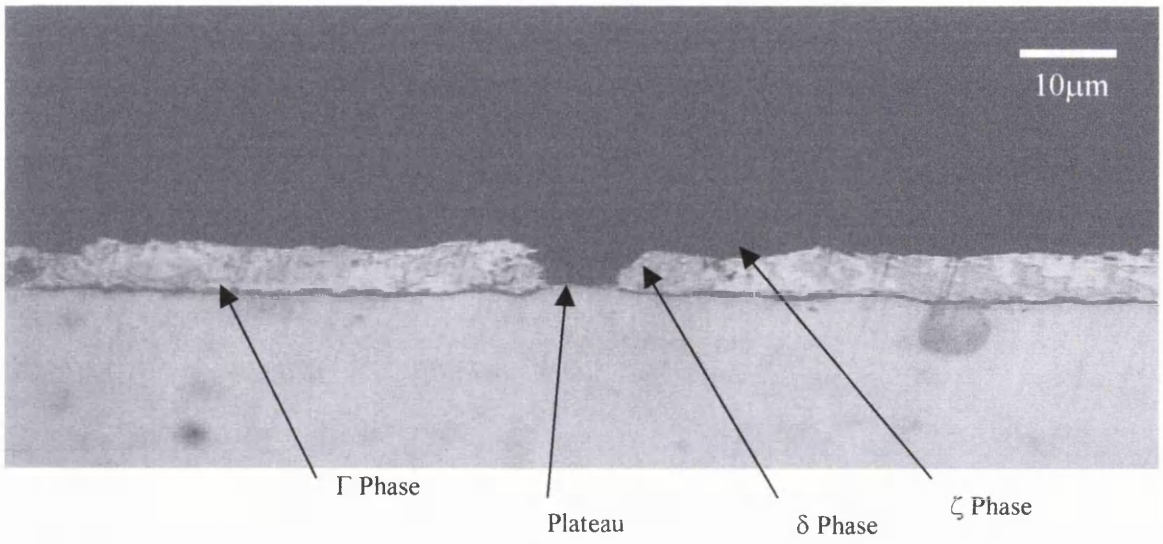

Figure 2.13. Optical image of a galvanneal crater.

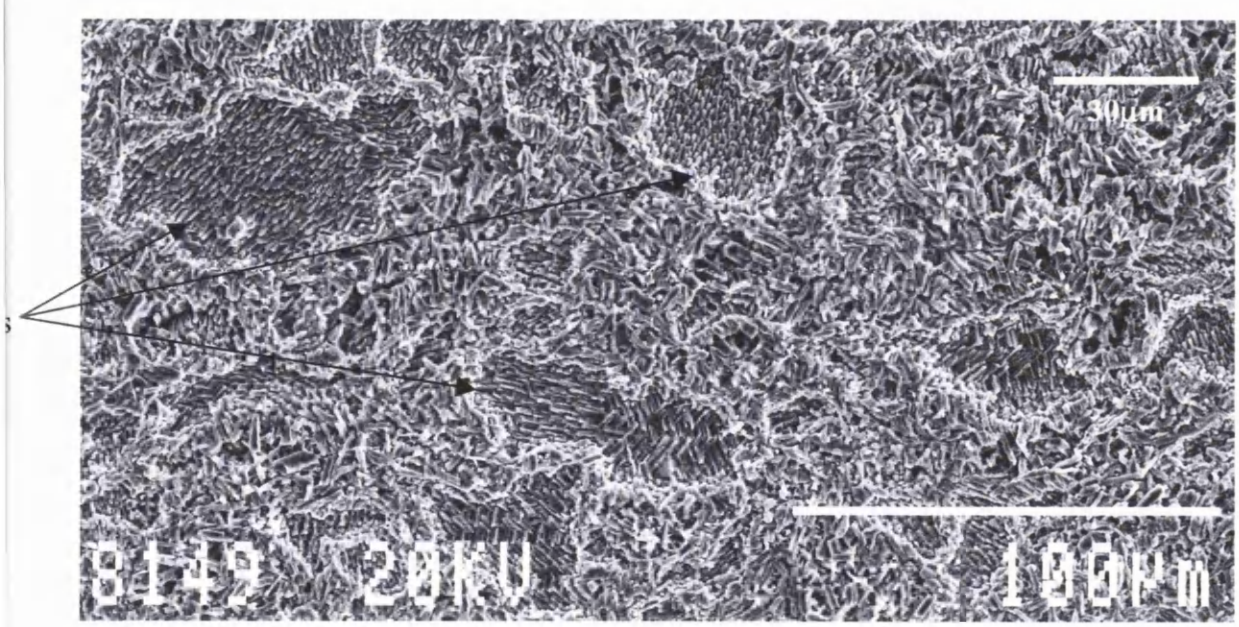

Figure 2.14. SEM image of the galvanneal coating containing craters.

2.9.3 The Effect of Cratering

Current understanding of the effect that craters have upon the properties of the galvanneal product is limited. However, the preliminary work done by Carless (1998) highlighted several important aspects. Comparing a Ti IF steel with a TiNb IF steel

Carless showed that the TiNb IF steel was more susceptible to crater formation than the Ti IF steel. This was primarily thought to be due to the increase in grain size of the TiNb steel leading to more stable crater formation.

Under mechanical testing, it was demonstrated further that the increased crater density had the result of reducing the amount of powdering. However, it is well known that Ti IF steels are much more reactive than TiNb IF steels because of the lack of carbon atoms at the grain boundaries (Jordan, 1998). Therefore, under similar processing conditions the Ti-stabilised steel will inherently have a much more brittle coating than the TiNb steel.

Because of this, Carless (2000) compared the powdering effects of Ti IF and TiNb steels both with similar iron contents in their coatings. He found that in low iron coatings (12wt% or less) the TiNb steel had the better powdering resistance whereas in high iron coatings (12wt% or more) the Ti steel was the best. The reason he proposed for this was that in low iron coatings the weak link is the Γ/steel interface, therefore, when the crater density is high, the plateaux will hinder crack propagation and reduce powdering. In the high iron coatings not only is the coating more brittle but the craters cause an increase in roughness. This then leads to increased friction, greater failure in the brittle δ phase and more powdering.

However, Carless' experimental data did not cover the complete range of iron contents. The iron content was consistently much lower in the TiNb coatings (11-15g/m^2) than in the Ti IF steels (13-21g/m^2). Consequently, the individual influences of iron content and crater density were not completely established and therefore the subject of further work.

However, it was clearly shown that thicker coatings are much less susceptible to crater formation. A possible reason for this could be that there is simply more zinc above the ζ crystals. This excess zinc cannot be absorbed by the growing outbursts and thus the crater remains 'filled in'. In addition, the longer galvannealing time required for the thicker coatings might mean that the outbursts have more chance of

covering over the ζ crystals or that the ζ crystals actually transform to δ. Thicker coatings are also more prone to powdering, although this is more likely to be due to an increase in the thickness of the brittle Γ layer rather than a lower crater density.

In terms of the effect upon paintability and surface appearance, the work of Carless showed that craters were easily masked over by the painting procedures implemented in the automotive industry. Therefore, craters are not of concern with regards to the paintability and final surface appearance of the galvanneal product.

The work of Wright (1998) under ILZRO Project ZC0-29 has shown similar results to those of Carless in that cratering helps to reduce powdering. However, the work of Wright introduces so many other variables that the results are not conclusive.

2.10 PROCESS PARAMETERS INFLUENCING CRATER DEVELOPMENT

From previous work done in the area of galvannealing, it is possible to propose process and substrate parameters that may influence the development of craters and their overall effect on the galvannealing coating.

2.10.1 Grain Size

An increase in the grain size of the substrate may result in larger areas that will be harder for outbursts to mask, thus leading to a higher crater density at the end of the galvannealing process. Grain size modification could be achieved by using substrates with Niobium additions or by annealing the substrate to promote grain growth. This would be an easy and simple way of altering the crater density to assess its overall effect upon formability properties without changing any other parameters. However, work done by Jordan *et al.* (1998) has shown that the grain size has a strong influence on inhibition layer breakdown. Their experiments showed that the time for outburst formation increased from 10 seconds for 15μm grains to 1200 seconds for 85μm grains. These findings would therefore have to be taken into account when manipulating the grain size. In addition, manipulation of the grain size on an

industrial basis may not be possible due to its large influence on the mechanical properties of the steel.

2.10.2 Aluminium Content of the Zinc Bath

Varying the aluminium content of the bath has been shown to have many different effects upon the formation of craters. Increasing the aluminium content will cause a greater and more preferential nucleation of the Fe_2Al_5 inhibition layer. The inhibition layer will not only 'steal' the majority of the sites upon which ζ could preferentially nucleate but also reduces the solubility of iron within the bath and decrease the peritectic temperature. Therefore, the ζ phase will not only be thermodynamically unstable and have no suitable nucleation sites but also may not even have a high enough iron content to be present in the first place. The aluminium content of the bath therefore has a great effect upon crater formation although a high aluminium content will create a thicker inhibition layer leading to longer processing times for a given coating iron content.

2.10.3 Grain Orientation

The ordered ζ phase may form epitaxially on the ferrite grains oriented with {111} in the plane of the sheet due to the low interfacial energy barrier. If there are no correctly oriented grains, the phase will not be able to nucleate as easily, resulting in a lower crater density. Preliminary work done by Carless (2000) showed that abrasion of the surface of the steel with emery paper greatly hindered crater formation. It is proposed that the abraded surface helped to promote the formation of the δ phase rather than the ordered ζ phase.

2.10.4 Annealing Time and Temperature

An increased annealing time or increased annealing temperature will lead to greater recrystallisation of the steel substrate. As a result a higher proportion of properly oriented grains will be present at the surface of the substrate. This will in turn

facilitate the epitaxial nucleation of the ordered ζ crystals and much greater crater formation.

2.10.5 Bath and Strip Entry Temperature

If the bath or strip entry temperature is higher than the aluminium-modified peritectic temperature, the ζ phase is no longer thermodynamically stable and will thus find it much harder to nucleate and grow. However, the temperature at which this occurs would be around 530°C, which from an industrial point of view would mean higher running costs and a much quicker breakdown of the inhibition layer.

2.10.6 Galvanneal Temperature

A galvannealing temperature higher than the peritectic temperature will cause the ζ phase to be no longer thermodynamically stable. However, by the time the strip reaches the galvanneal furnace the ζ phase will have already nucleated and grown. The galvanneal furnace would therefore have to cause the transformation of the ζ phase to the δ phase. The amount of time required for this and its exact nature is not clear and is therefore a definite area for further research.

2.11 CONCLUSIONS OF THE LITERATURE REVIEW

The conclusions of the literature review are as follows:

- The galvanneal coating provides a cheap and effective way of protecting a steel substrate from corrosion.
- The galvanneal coating has both improved weldability and paintability compared to the standard galvanised product.
- Coating failure of the galvanneal product occurs because of the formation of intermetallic phases within the coating.
- Coating failure occurs primarily at the brittle interface between the coating and the substrate.

- The initial formation of the galvanneal coating is the result of competition between different nucleating phases.
- The formation of craters within the galvanneal coating is due to the epitaxial nucleation of ordered crystals upon ferrite grains oriented with {111} in the plane of the sheet.
- It is proposed that the presence of craters within the galvanneal coating helps to prevent coating failure during press forming operations.

3 DERIVATION OF THE GAMODELLER

The following chapter details the development of the GAModeller program, all of which took place as part of this project. The theoretical work of diffusion couples is described in detail together with how they are applicable to the growth of the galvanneal coating. Further explanations include how the process parameters involved with online production have been incorporated into the model.

3.1 INTRODUCTION

Diffusion occurs so as to minimise the Gibbs free energy of the whole system (Porter and Easterling, 1995). If two blocks of the same A-B solid solution, but different compositions are placed together at a sufficiently high temperature inter-diffusion of the A and B atoms will occur so as to reduce the overall energy, figure 3.1.

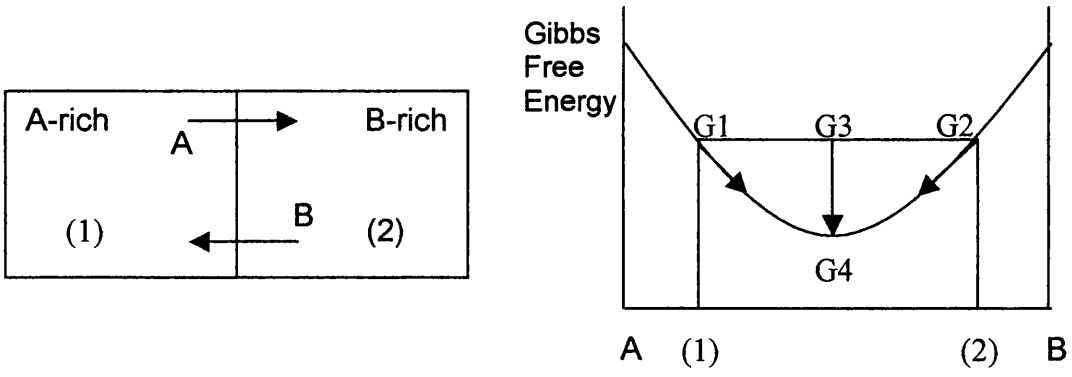

Figure 3.1. Free energy and compositional changes during 'downhill' diffusion.

The free energy of each part of the alloy is given by G1 and G2 and the energy of the overall system by G3. As diffusion occurs so as to eliminate the concentration differences the overall energy decreases to G4, the free energy of a homogeneous alloy. As such the A and B atoms diffusing away from the region of high concentration to that of low concentration achieve the decrease in free energy. Thus movement down a concentration gradient is observed.

However this is not always the case as in alloy systems containing a miscibility gap the free energy curve can have a negative curvature at low temperatures, figure 3.2.

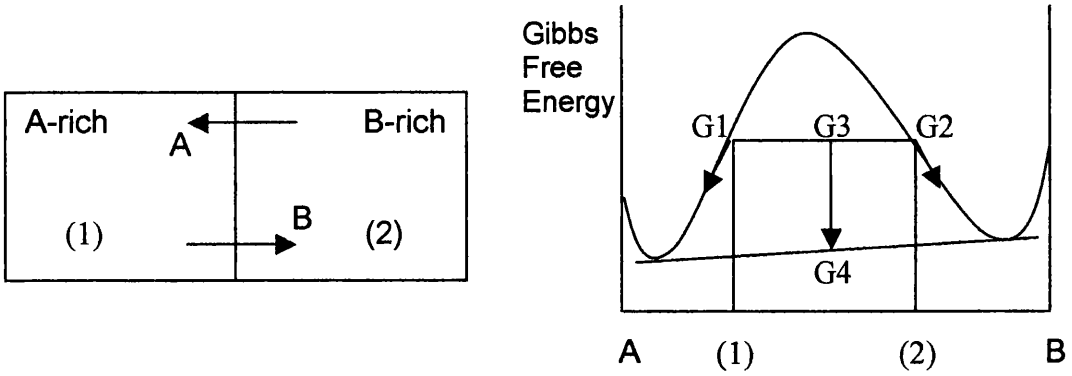

Figure 3.2. Free energy and compositional changes during 'uphill' diffusion.

Again the respective energies of the individual alloys are given by G1 and G2 and the overall energy by G3. In this instance the atoms diffusing towards the regions of high concentration, i.e. uphill, achieve the decrease in overall energy from G3 to G4.

In both instances the A and B atoms are diffusing from regions of high chemical potential to regions of low chemical potential. This change in concentration with energy is defined by the Cahn-Hilliard equation (Cahn & Hilliard, 1958).

$$\frac{\delta c}{\delta t} = \nabla.\left[M\nabla\left(\frac{\delta F}{\delta c} - \varepsilon^2 \nabla^2 c \right) \right] \tag{3.1}$$

where: M is the kinetic coefficient of diffusion (mobility)

c is the concentration

F is the free energy functional

ε is the energy associated with the creation of interfaces

The kinetic coefficient of diffusion, M, is assumed to be independent of the concentration. The parameter ε measures the range of intermolecular interactions and raises the overall free energy through the existence of interfaces between the phases.

In practice 'downhill' diffusion where the chemical potential gradient is along the same direction as the concentration gradient is far more common than 'uphill' diffusion. It is therefore usually assumed that diffusion occurs down concentration gradients. However, it can be seen that this is only true under special circumstances and for this reason it is strictly speaking better to express the driving force for diffusion in terms of a chemical potential gradient (Porter and Easterling, 1995). Diffusion ceases when the chemical potentials of all atoms are the same everywhere and the system is in equilibrium.

However, concentration differences are much easier to measure than chemical potential differences, as a result it is more convenient to relate diffusion to concentration gradients. The remainder of this chapter will therefore use this approach to diffusion.

3.2 DIFFUSION COUPLES

As stated previously, when two metals are placed in intimate contact at an elevated temperature, interdiffusion between the two metals will occur. If the two materials are not completely soluble in each other and do not exhibit any intermediate phases then the model is quite simple. A simplified phase diagram is shown in figure 3.3.

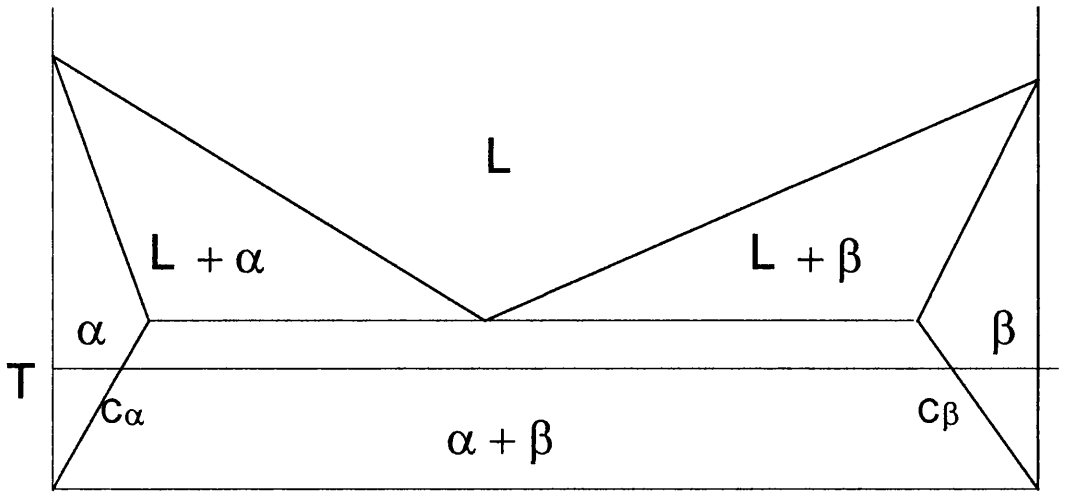

Figure 3.3. Simplified phase diagram.

As the temperature is elevated the A and B atoms diffuse into one another. The concentration of A atoms is shown in figure 3.4. As diffusion occurs the A atoms are slowly replaced by B atoms as the A atoms diffuse into material B and vice versa. After a long enough time at this elevated temperature (T) the two separate blocks of A and B will become one block of $\alpha + \beta$.

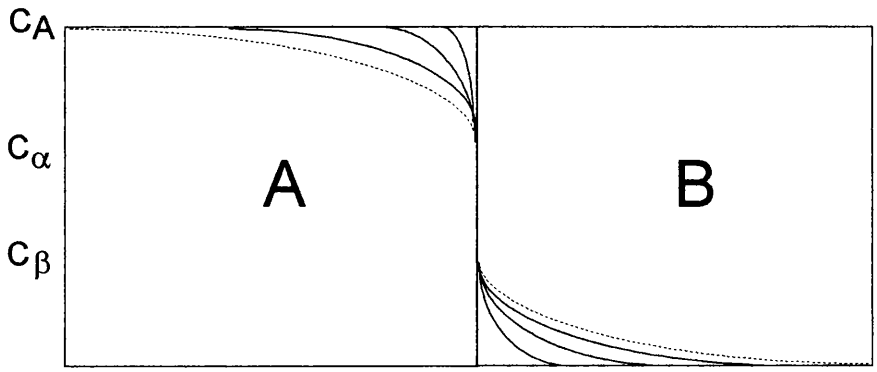

Figure 3.4. Schematic diagram of the concentration of A atoms.

3.2.1 Diffusion Couples with Intermediate Phases

In more complicated systems, such as the Fe-Zn system, intermediate phases form as the diffusional process continues. The phase diagram in figure 3.5 shows a simple binary phase diagram with an intermediate phase.

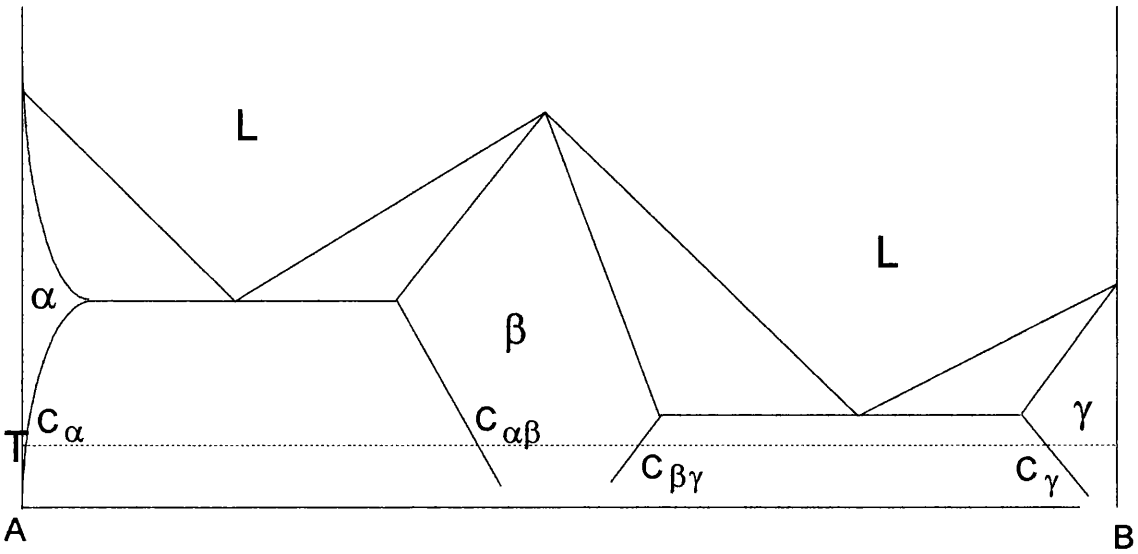

Figure 3.5. Schematic phase diagram exhibiting an intermediate phase.

If a piece of A is placed in contact with a piece of B a thin layer of the intermediate phase β will form between the two terminals of the α and γ phases. The profile across the two materials would be as in figure 3.6

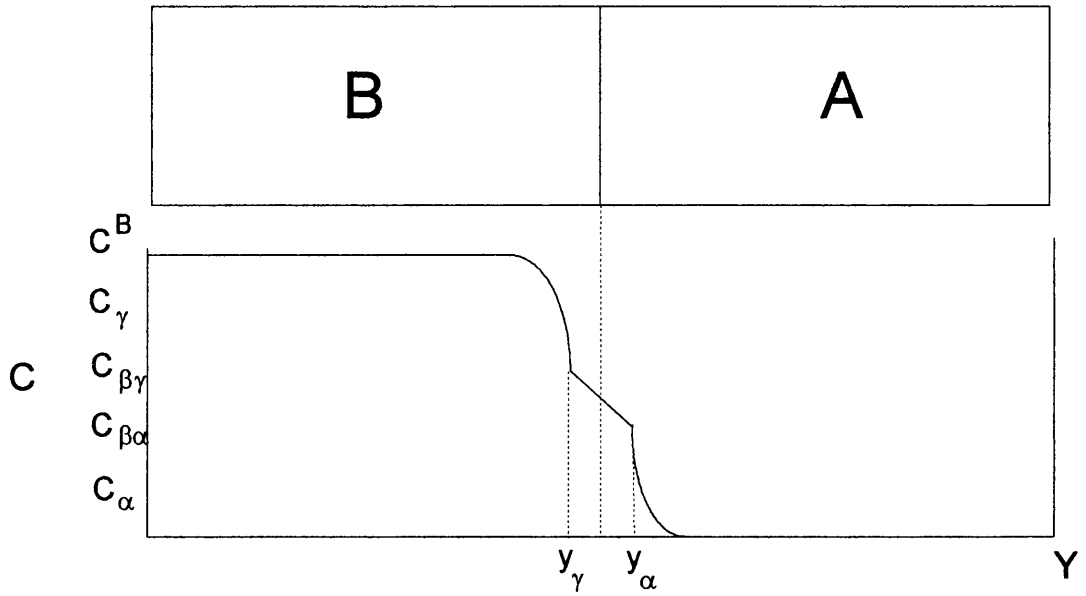

Figure 3.6. Diffusion profile across two materials exhibiting an intermediate phase.

If a pseudo-steady-state condition is assumed within the β layer, then a linear concentration profile exists across the β phase and Fick's First Law, Wilkinson (1997), gives the flux, or flow of atoms:

$$J_\beta = -D_\beta \times \frac{\delta C_\beta}{\delta y} \tag{3.2}$$

where: J_β is the flux or flow of atoms

D_β is the diffusion coefficient

δC_β is the change in concentration

δy is the distance over which the change in concentration takes place.

Applying Fick's Law to the diffusion couple in figure 3.4 the following equation is arrived at:

$$J_\beta = -D_\beta * \frac{(C_{\beta\alpha} - C_{\beta\gamma})}{(y_\alpha - y_\gamma)}$$

$$J_\beta = -D_\beta * \frac{(C_{\beta\gamma} - C_{\beta\alpha})}{L} \tag{3.3}$$

where: J_β is the flux across the β phase

D_β is the diffusion coefficient of the atoms through the β phase

$C_{\beta\gamma}$ is the concentration at the βγ interface

$C_{\beta\alpha}$ is the concentration at the βα interface

L is the time dependent thickness of the intermediate layer.

The motion of each of the interfaces y_α and y_γ is governed by the principle of mass conservation. If the simple phase diagram in figure 3.5 is considered along with what happens if the interface moves by an amount dy_I over a time interval dt then the amount of B atoms that move into the α-phase is equal to J_α*A*dt, where A is the area of the interface. Similarly, the amount moving out of the β-phase is J_β*A*dt. Thus the total build-up of atoms at the interface is equal to $(J_\beta - J_\alpha)$*A*dt. This excess material must go towards creating more of the B rich phase, i.e. the β-phase. As this happens the interface moves by dy_I. The amount of B which is taken up is therefore equal to $(C_\beta - C_\alpha)$*A*dy_I. Therefore, by equating these two terms we can determine the rate of interface motion to be:

$$\frac{dy_I}{dt} = \frac{(J_\beta - J_\alpha)}{(C_\beta - C_\alpha)} \tag{3.4}$$

If this equation is now applied to the diffusion couple with intermediate phases, as shown in figure 3.5, the following equations are arrived at:

$$\frac{dy_\alpha}{dt} = \frac{(J_\beta - J_\alpha)}{(C_{\beta\alpha} - C_\alpha)} \tag{3.5}$$

$$\frac{dy_\gamma}{dt} = \frac{(J_\gamma - J_\beta)}{(C_\gamma - C_{\beta\gamma})} \tag{3.6}$$

When the layer is very thin, J_β must be very large and will dominate the equation. The growth of the layer (dL/dt) is thus given by the difference between the motion of each interface, that is adding equation 3.5 to equation 3.6:

$$\frac{dL}{dt} = \frac{dy_\alpha}{dt} - \frac{dy_\gamma}{dt} \approx \frac{J_\beta}{(C_{\beta\alpha} - C_\alpha)} + \frac{J_\beta}{(C_\gamma - C_{\beta\gamma})} \tag{3.7}$$

If, from equation 3.3, J_β is substituted into the equation, the result is:

$$\frac{dL}{dt} = \frac{D_\beta}{l} * \left(\frac{(C_{\beta\gamma} - C_{\beta\alpha})}{(C_{\beta\alpha} - C_\alpha)} + \frac{(C_{\beta\gamma} - C_{\beta\alpha})}{(C_\gamma - C_{\beta\gamma})} \right) \tag{3.8}$$

If this is then integrated with respect to time the usual parabolic dependence of layer thickness (L) with time is arrived at, namely:

$$L^2 = 2D_\beta t * \left(\frac{(C_{\beta\gamma} - C_{\beta\alpha})}{(C_{\beta\alpha} - C_\alpha)} + \frac{(C_{\beta\gamma} - C_{\beta\alpha})}{(C_\gamma - C_{\beta\gamma})} \right) \tag{3.9}$$

3.3 APPLICATION TO THE GALVANNEALING REACTION

The previous section has shown how the principle of diffusion couples can be applied to the growth of an intermediate phase at elevated temperatures. Applying the theory to the growth of the galvannealing reaction requires an understanding of the concentration differences and diffusion coefficients in the Fe-Zn system, the growth rate constant and the effect of production process parameters.

3.3.1 Concentration Differences on the Fe-Zn Phase Diagram

Equation 3.9 shows that the rate of growth of an intermediate layer is highly dependent upon the concentration differences both within the phase and those either side of it. Figure 3.7 illustrates a schematic diagram of the zinc rich end of the Fe-Zn phase diagram.

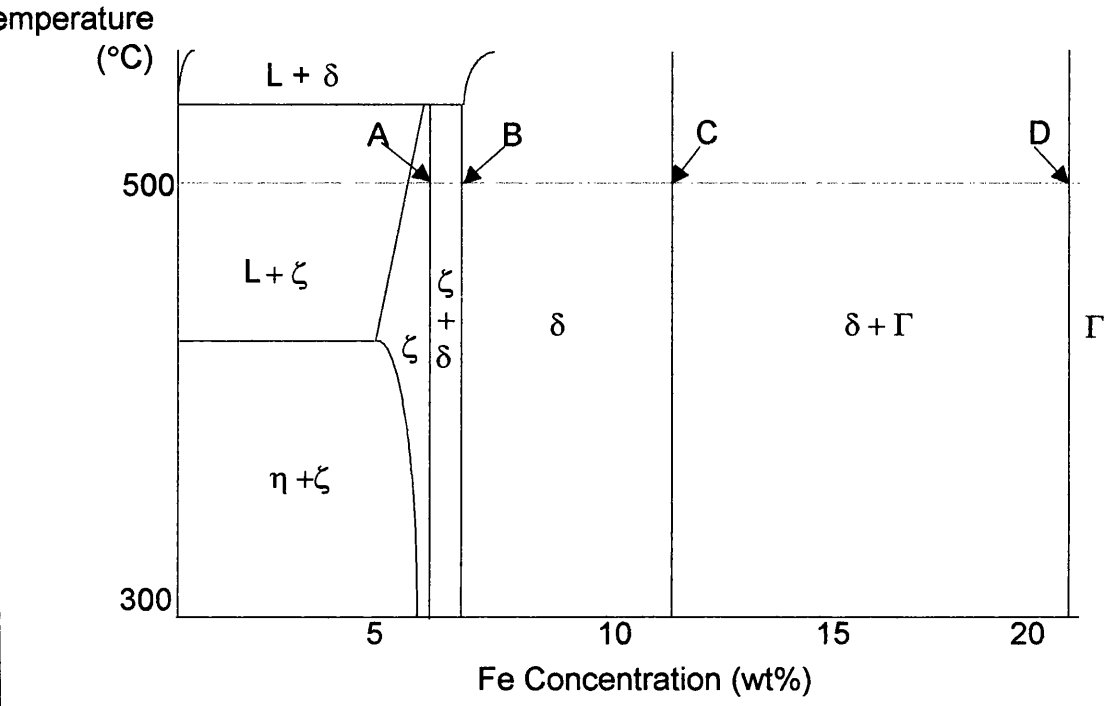

Figure 3.7. Schematic diagram of the zinc rich end of the Fe-Zn phase diagram.

For the δ phase at a galvannealing temperature of 500°C equation 3.9 becomes:

$$L\delta^2 = 2Dt * \left(\frac{(C_{\delta(\delta+\Gamma)} - C_{\delta(\zeta+\delta)})}{(C_{\delta(\zeta+\delta)} - C_{\zeta(\zeta+\delta)})} + \frac{(C_{\delta(\delta+\Gamma)} - C_{\delta(\zeta+\delta)})}{(C_{\Gamma(\delta+\Gamma)} - C_{\delta(\delta+\Gamma)})} \right) \qquad (3.10)$$

However, for easier reading the letters on the phase diagram will be used to represent the boundaries of the different phases, equation 3.10 then becomes:

$$L_\delta^{\,2} = 2Dt * \left(\frac{(C-B)}{(B-A)} + \frac{(C-B)}{(D-C)} \right) \qquad (3.11)$$

where: A = 6.2, B = 7, C = 11.4, D = 21

The same process can be applied to both the ζ and Γ phases. However, from the Fe-Zn phase diagram it is clear to see that the value of some boundaries varies with temperature and must therefore be taken into account when dealing with any type of modelling.

3.3.2 The Diffusion Coefficient of Iron in Zinc

Equation 3.11 shows that the growth rate of an intermediate phase is also dependent upon the diffusion coefficient, D. In the case of the galvannealing reaction this is the diffusion coefficient of iron in zinc that is easily determined from the Arrhenius equation 3.12.

$$D = D_0 * e^{\left(\frac{-Q}{RT}\right)} \qquad (3.12)$$

where: D_o is the pre-exponential factor (m^2/s)

Q is the activation energy for diffusion (J/mol)

R is the molar gas constant (8.314 J/mol K)

T is the temperature in Kelvin (K).

However, the values of Q and D_o are much harder to acquire especially considering the fact that they vary between the different phases. The work of Wakamatsu (1997) as published in the Smithells Metals Reference Book arrived at the following values for D_o and Q.

Table 3.1. Diffusion values of iron in zinc obtained by Wakamatsu *et al.*

Phase	**Pre-Exponential Factor, D_o (m^2/s)**	**Activation Energy, Q (kJ/mol)**
Zeta (ζ)	2.28×10^{-6}	83.3
Delta (δ)	2.82×10^{-7}	80.4
Gamma (Γ)	1.05×10^{-7}	92.1

The values for diffusion coefficients are generally calculated by plating the diffusing species onto the material for which the diffusion coefficient is to be calculated, as shown in figure 3.8.

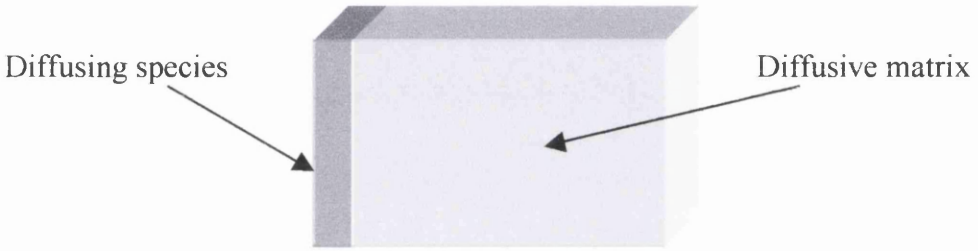

Figure 3.8. Experimental set up for determining diffusion coefficients.

The variation of concentration with distance and time is given by equation 3.13.

$$C(y,t) = \frac{C * \delta}{\sqrt{\pi D t}} \exp\left(\frac{-y^2}{4Dt}\right) \tag{3.13}$$

where: δ is the thickness of the plane initial source

y is distance into the material

C is the initial concentration of the plane initial source

t is the time over which the diffusion takes place

D is the diffusion coefficient

Therefore by plotting the log of the iron content against the distance squared it can be shown that the slope of the graph will be equal to:

$$gradient = \frac{-1}{4Dt} \tag{3.14}$$

Using this approach experimental work, as detailed in section 5.7, was carried out to test and validate the values for D_o and Q as detailed in table 3.1.

3.3.3 Growth Rate Constant

Equation 3.9 stated that:

$$L^2 = 2D_\beta t * \left(\frac{(C_{\beta\gamma} - C_{\beta\alpha})}{(C_{\beta\alpha} - C_\alpha)} + \frac{(C_{\beta\gamma} - C_{\beta\alpha})}{(C_\gamma - C_{\beta\gamma})} \right)$$

This can be greatly simplified to the growth rate equation of kt^n where:

$$k = \sqrt{2D * \left(\frac{(C_{\beta\gamma} - C_{\beta\alpha})}{(C_{\beta\alpha} - C_\alpha)} + \frac{(C_{\beta\gamma} - C_{\beta\alpha})}{(C_\gamma - C_{\beta\gamma})} \right)}$$

and

$$n = 0.5$$

Equation 3.9 therefore becomes:

$$L = kt^{0.5} \tag{3.15}$$

However, the work of Jordan *et al.* (1997) and Onishi *et al.* (1974) has shown that the growth rate constant, n, is not the same for all the phases and is not equal to 0.5. Onishi *et al.* (1974) conducted experiments on iron-zinc diffusion couples heated at temperatures between 210°C and 410°C and concluded that the growth rate constants for the different phases were as follows:

$$n_\zeta = 0.36$$

$$n_\delta = 0.49$$

$$n_\Gamma = 0.23$$

These values show that the δ growth rate constant is still very close to 0.5 but that the values for the ζ and Γ phases are quite considerably lower. This shows that with a value close to 0.5 the growth of the δ phase is diffusion controlled whereas other factors play a part in the growth of the ζ and Γ phases.

The work of Jordan *et al.* (1992) looked at the effect of aluminium additions on the growth rate constant during galvanising and arrived at similar values to those of Onishi *et al.* (1974).

3.3.4 Aluminium Additions

In all commercial galvanising lines aluminium is added to the zinc spelter to create an inhibition layer between the zinc and the substrate. In a galvanising spelter the aluminium level is kept high to prevent the diffusion of iron atoms into the zinc. In a galvannealing spelter the aluminium level is reduced to allow alloying to take place during the subsequent heating of the strip.

In terms of the modelling approach the inhibition layer has the effect of introducing a time delay to the start of the alloying process, the magnitude of which can be attributed mainly to the effective aluminium content of the spelter.

From the work of Guttmann *et al.* (1995), Morimoto *et al.* (1997) Hertveldt *et al.* (1998) and Price (1999) we are able to assess the variation of inhibition layer thickness with the effective aluminium content of the bath.

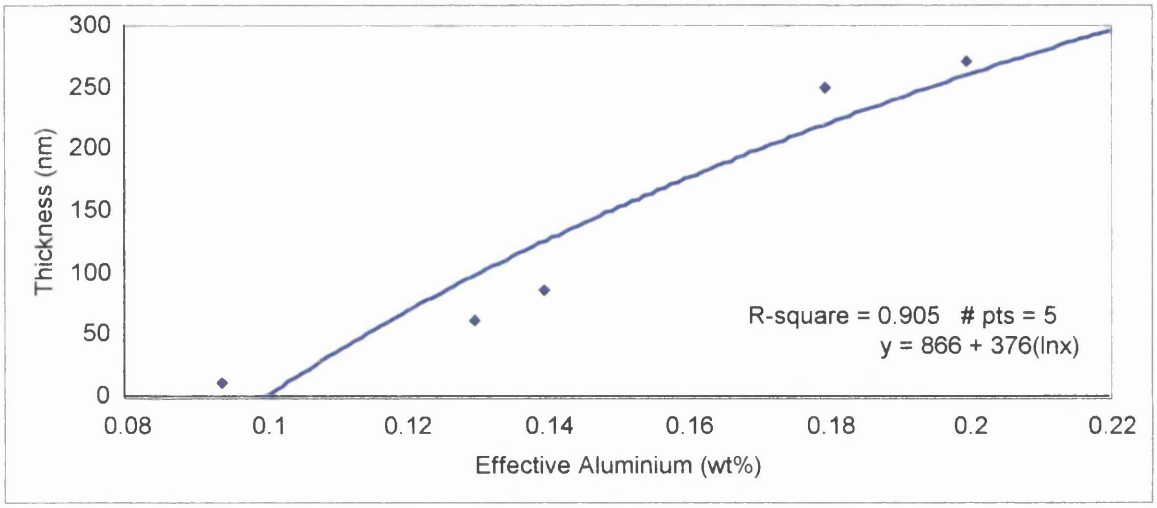

Figure 3.9. Variation of inhibition layer thickness with effective aluminium content.

A logarithmic fit was used to assess the relationship between thickness and effective aluminium. As the effective aluminium content increases, the thickness will eventually level out because the aluminium atoms cannot diffuse to the substrate within the specified time.

The time delay of the inhibition layer was modelled using the concept of the nominal diffusion distance and analysing the diffusion of zinc atoms through the aluminium inhibition layer.

The diffusion into a solid from a fixed surface concentration, C_s, takes the form of equation 3.16.

$$C(y,t) = C_s erfc\left(\frac{y}{2\sqrt{Dt}}\right) \tag{3.16}$$

where: y = the distance through the solid

t = the time interval over which the diffusion takes place

D = the diffusion coefficient of the diffusing atoms through the solid

Figure 3.10 shows a schematic plot of the concentration of atoms diffusing from a surface of fixed concentration.

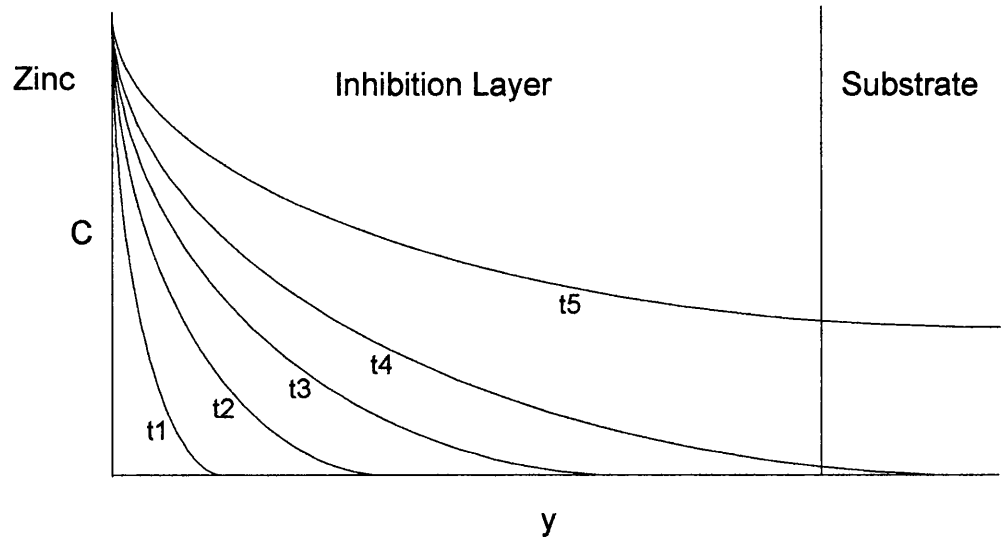

Figure 3.10. Schematic diagram of the diffusion of atoms from a fixed concentration.

Experimental observations have shown that the ζ phase (zinc content 94wt%) is the first to develop and breakthrough the inhibition layer. Therefore, using equation 3.16 and assuming that the spelter concentration is 100wt% zinc it can be shown that:

$$erfc\left(\frac{y}{2\sqrt{Dt}}\right) = 0.94 \tag{3.17}$$

Using the knowledge that erfc = 1 - erf, equation 3.16 becomes:

$$1 - erf\left(\frac{y}{2\sqrt{Dt}}\right) = 0.94 \tag{3.18}$$

Further manipulation of equation 3.18 and the use of error function tables enables the calculation of the time delay before alloying takes place:

$$t = 100 \times \frac{y^2}{D} \tag{3.19}$$

where: t is the time delay before alloying takes place

y is the thickness of the inhibition layer

D is the diffusion coefficient of zinc atoms through aluminium

Using the Arrhenius equation detailed in equation 3.12 it is possible to calculate the value of D from the published values of D_0 and Q in Smithells Reference Book of Metals. Two sets of values from two separate authors are published within this book and detailed in table 3.2.

Table 3.2. Values for D_o and Q for the diffusion of zinc in the inhibition layer.

Set	Authors	D_0 (m^2/s)	Q (kJ/mol)
A	Peterson and Rothman (1997)	3.25×10^{-5}	117.9
B	D. L. Bdke (1997)	2.45×10^{-5}	119.6

Experimental work, as detailed in section 5.7, was carried out to test and validate these values.

3.4 ASSUMPTIONS OF THE MODEL

To facilitate the production of the model certain assumptions were made. The first of these was the use of a single temperature during the galvannealing process. After leaving the bath the strip is heated up to the galvannealing temperature, held for a certain period of time and then cooled. However, the model assumes that the coated strip is instantly at the galvannealing temperature, held for the allotted time and then instantly cooled back down to room temperature.

During the galvannealing process intermetallic formation can sometimes progress through a series of outburst structures occurring at emerging grain boundaries. This leads to local variations within the coating structure. The model assumes that these outburst structures are minimal and that the coating forms in layers of η, ζ, δ and Γ. In addition the model assumes that these layers are present in very small quantities at the start of the galvannealing process. These layers grow during the galvannealing process (Foct *et al.*, 1993) and as such no nucleation stage exists and no energy change is associated with the interfaces between the phases. As these layers grow the

free zinc, η, will be consumed until the intermetallic phases reach the surface of the coating. When the surface is reached the model assumes that the ζ phase will be consumed by the growing δ phase (Lamberigts, 1992 and Mataigne *et al.*, 1995) and that no energy barrier exists to this transformation.

Other assumptions are that due to the thin nature of the coating there is no stirring or mixing within the coating and that the transport of iron through the coating is diffusion controlled. Furthermore, each of the phases is assumed to be homogeneous with identical diffusivity throughout. Finally, as predicted on the iron-zinc phase diagram, no ζ phase exists if the galvannealing temperature is above 530°C.

4 EXPERIMENTAL PROCEDURES

The following chapter details the procedures and equipment utilised during the program of work.

4.1 RHESCA HOT DIP SIMULATOR

The production of online galvanneal samples under varying processing conditions was not possible due to the restrictions of line parameters and production schedules. The production of laboratory controlled galvannealed coatings was therefore carried out on the Rhesca hot dip simulator based at the Engineering Centre for Materials and Manufacturing (ECM^2) in Port Talbot. The Rhesca hot dip simulator consists of three main components, the computer control, the main tower and the satellite furnaces.

The computer control system operates the EuroSimulator™ software package written by Faulk Systems GMBH. The software package enables the user to control and manipulate the other two components of the hot dip simulator. The main tower is made up of four sections, the loading and cooling section, the heating section, the gas wiping section and the zinc spelter. A schematic diagram of the four sections is illustrated in figure 4.1

The satellite furnaces system consists of four independent Kanthal electric resistance furnaces controlled by the computer system. These furnaces enable the preparation of varying spelters separately from the main tower. A photograph of the main tower and the computer control system is shown in figure 4.2.

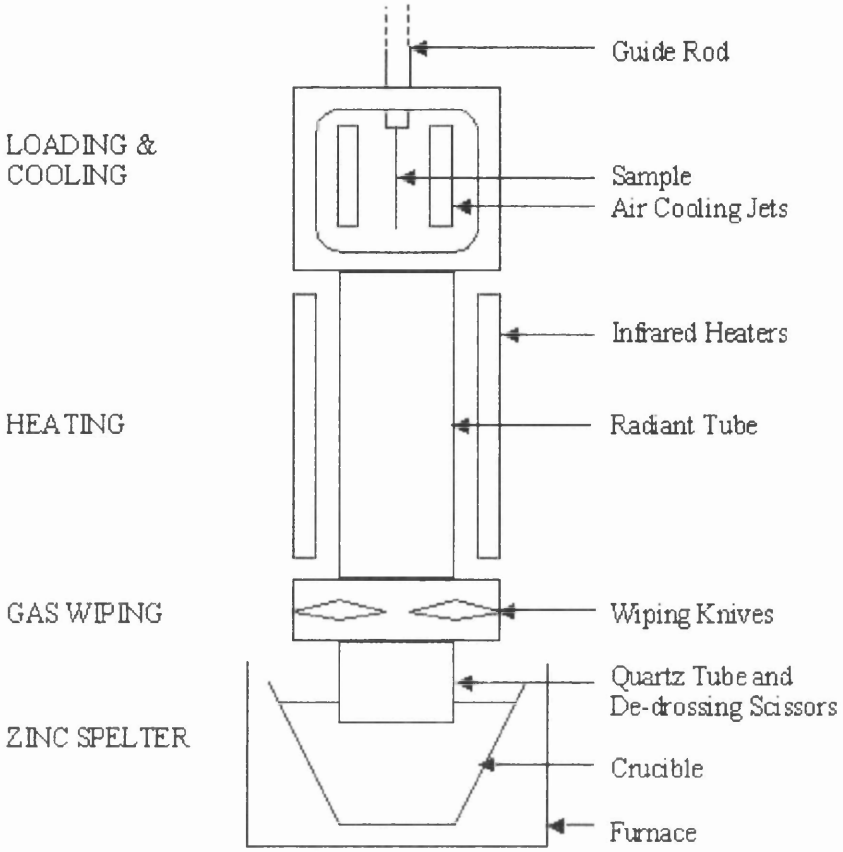

Figure 4.1. Schematic diagram of the Rhesca hot dip simulator at Port Talbot.

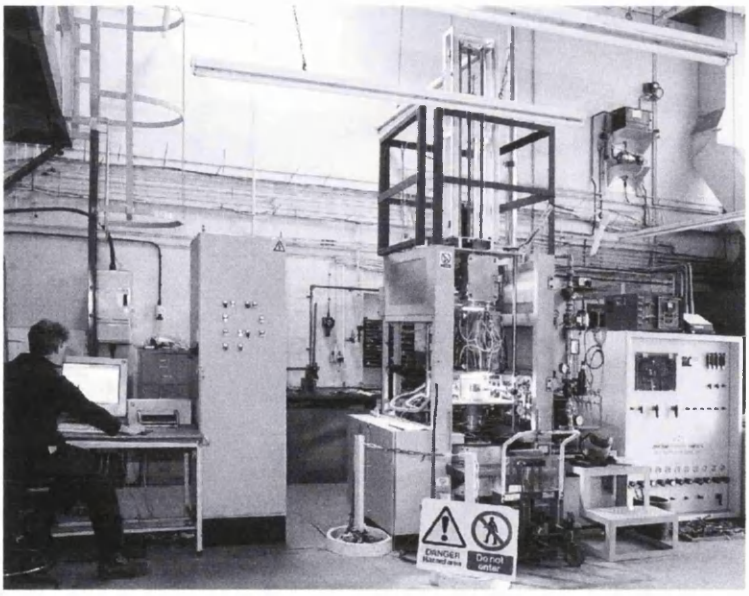

Figure 4.2. Photograph of the Rhesca hot dip simulator based at Port Talbot.

4.1.1 Rhesca Hot Dip Simulator Panels

The panels used in the Rhesca hot dip simulator are produced following the Welsh Technology Centre (WTC) operating procedure PD/MC/01, Laboratory Production of Hot-Dip Products. The panels are cut to a size of 200mm by 105mm using a Morgan Rushworth shear. A process window 65mm by 50mm is punched from the top section of the panel to reduce the amount of uncoated material that needs to be heated. Furthermore, to increase the rigidity and prevent movement during processing beads are pressed along the sides of the panel. Finally, for safety reasons, the corners of the panel are removed. A schematic diagram of a Rhesca hot dip simulator panel is illustrated in figure 4.3.

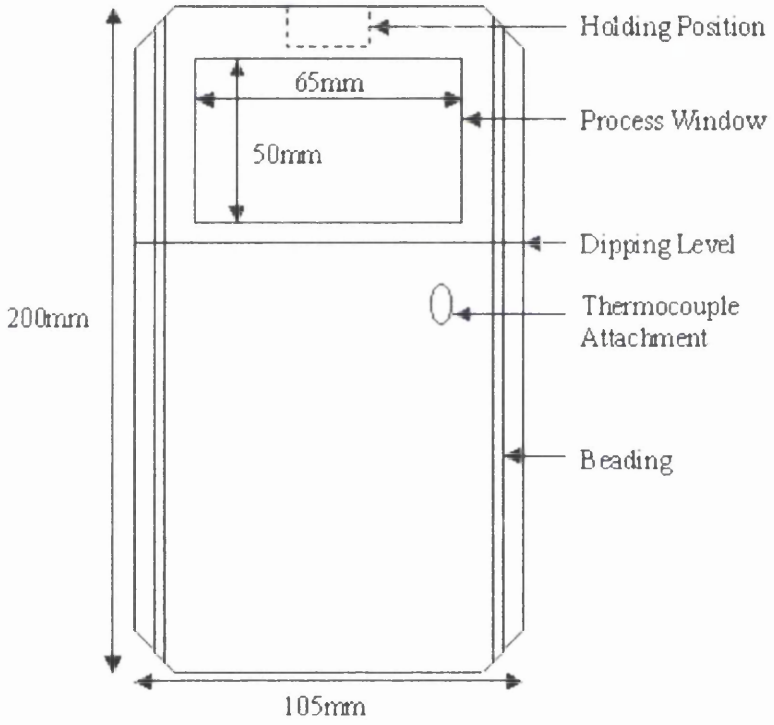

Figure 4.3. Schematic diagram of a HDS panel.

4.1.2 Processing of Rhesca Hot Dip Simulator Panels

The processing of panels was performed under the Welsh Technology Centre operating procedure PD/MC/01, Laboratory Production of Hot-Dip Products. The panel is cleaned with acetone to remove any excess oil before being attached to the

guide rod in the loading section of the main tower. A k-type resistance thermocouple is spot welded to the upper right corner of the panel to enable accurate control and recording of the temperature changes. The door of the loading section is closed and held shut with four wing nuts at each corner to ensure an airtight seal.

To maintain a controlled environment the radiant tube, loading section and the upper part of the quartz tube are placed under vacuum and reduced to a pressure of approximately 30Pa. Once this pressure has been obtained the vacuum is turned off and the pressure returned by purging with a 5 % hydrogen 95% nitrogen gas mix.

Utilising the computer control system a set of instructions are input into the EuroSimulator™ software package detailing the exact specifications of the experiment. These specifications include, but are not limited to:

- annealing temperature
- heating rate
- annealing time
- panel entry temperature
- dipping time
- wiping speed
- wiping pressure
- galvannealing temperature
- galvannealing time
- cooling rate

Upon execution of the program the panel moves down into the radiant tube at a speed of up to 1200 mm/s where it is heated to the specified temperature in the required time by infrared heaters. The panel is held at this temperature for the required period of time before returning to the loading and cooling section. Whilst in this position the operator uses the de-drossing scissors to remove any oxides or dross particles from the surface of the liquid zinc.

In the loading and cooling section the panel is cooled down to the specified temperature by the use of air jets either side of the panel. Upon attaining the required temperature the panel moves down through the radiant tube and into the liquid zinc. Whilst in the liquid zinc the air knives are switched on and nitrogen gas is forced through the nozzles at high speed and pressure. Once the specified dipping time has been achieved the panel is withdrawn from the liquid zinc and through the air knives. The high pressure of the nitrogen gas removes excess zinc from the panel and produces a coating of the required thickness.

If the panel is to have a galvanised coating it is returned back to the loading and cooling section where it is cooled with nitrogen gas back down to room temperature. If a galvanneal coating is to be created the panel stops in the radiant tube where it is heated to the specified temperature in the required time. Upon reaching the specified temperature the panel is held at that temperature for the required period before moving back into the heating and cooling section where it is cooled with nitrogen gas down to room temperature. A typical heating regime for a galvannealed Rhesca hot dip simulator panel is shown in figure 4.4.

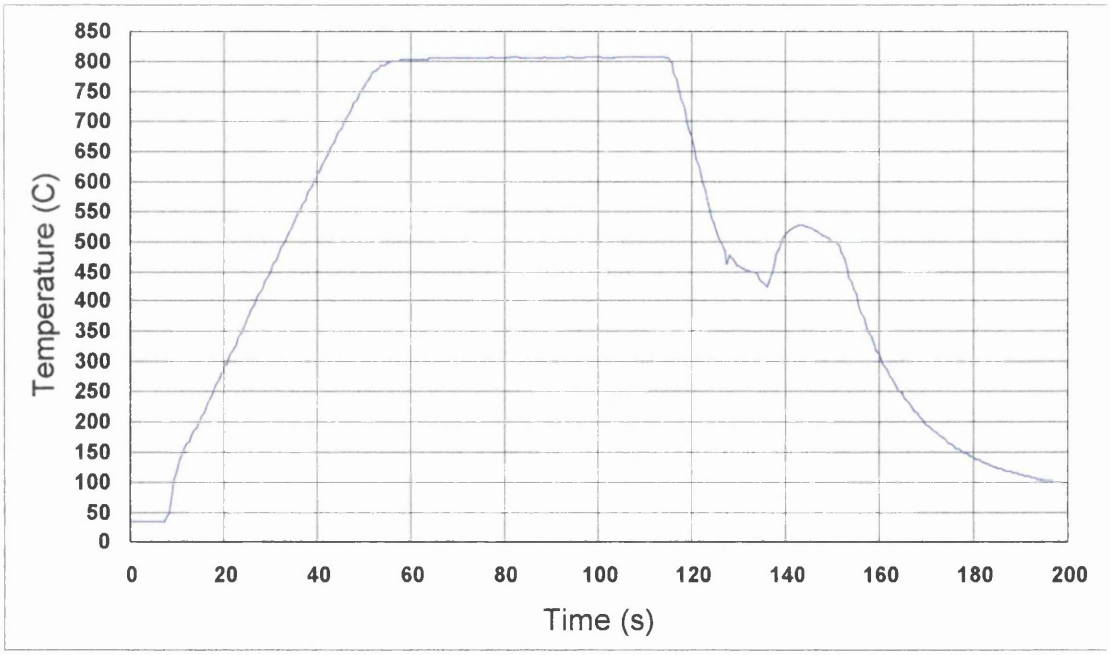

Figure 4.4. Typical heating regime for a galvannealed Rhesca hot dip simulator panel.

4.1.3 Accuracy and Limitations of the Rhesca Hot Dip Simulator

The Rhesca hot dip simulator allows accurate and easy manipulation of the process parameters involved during the commercial production of galvanneal. The temperature control is accurate to ±1°C and the coating thickness accurate to ±2 microns.

However, exact replication of commercial processing conditions is not possible due to the configuration of the Rhesca hot dip simulator. The main difference is the use of infrared heating lamps on the Rhesca hot dip simulator compared to a mixture of gas and induction heating used on most galvanising lines. In addition the continuous movement of the steel substrate within the zinc spelter during the dipping process cannot be simulated on the Rhesca hot dip simulator.

4.2 COATING AND SPELTER ANALYSIS

The chemical composition of both the galvanneal coating and the zinc spelter of the Rhesca hot dip simulator can have profound effects upon the coatings physical properties and characteristics. An accurate measurement of both of these parameters was carried out using Inductively Coupled Plasma Spectrophotometry (ICP).

Identification of the phases under the optical microscope was achieved by etching the polished samples with a Kilpatrick solution for a few seconds. This resulted in the ζ phase showing up as yellowy brown colour, the δ phase a blue colour and the Γ phase a dark brown colour.

4.3 CRATER DENSITY MEASUREMENTS

To assess and quantatively measure the crater coverage 10mm by 10mm sections were punched from the samples produced on the Rhesca hot dip simulator. These were analysed in a Scanning Electron Microscope (SEM) using the Welsh Technology Centre operating procedure CP/03/OP/02, General Operation of the JEOL 840A SEM. Ten images of each sample were taken from random points on the

surface at a magnification of 300x. This degree of magnification allowed an area of 125,000μm^2 to be analysed per image and still enable easy identification of the craters present.

The images taken were then loaded into the KS300 image analysis software package. Once loaded the craters present within the surface of the sample were manually identified and the outer perimeter of them drawn around. After identifying all the craters the software package calculated the actual crater coverage both in μm^2 and percentage of the image. Once all ten images had been analysed an average was obtained for the total crater coverage of the sample.

4.4 POWDERING TESTS

To assess the effect that craters have upon the coating failure mechanisms of the galvanneal coating 55mm discs were punched and de-burred from the processed panels. These discs were then processed according to the Welsh Technology Centre operating procedures PE/SE/02, Procedure for the 55mm to 33mm Cup Draw Powdering Tests, and PE/SE/03, Procedure for the Weight Loss Powdering Test.

Each disc was ultra-sonically cleaned in an acetone bath for three minutes and then accurately weighed using a Sartorius electronic balance, accurate to ±0.0001g. If the effect of lubrication was also to be analysed a coating of the commercially available Quaker P20K2 oil was applied to both sides of the disc. In addition both sides of the disc were covered with a sheet of acetate.

Deformation of the disc into a cup shape was achieved on an Erichsen Press where a 32mm diameter punch was used with a punch speed of 1mm/s and a blank holder force of 1kN. The starting disc and formed cup are shown in figure 4.5.

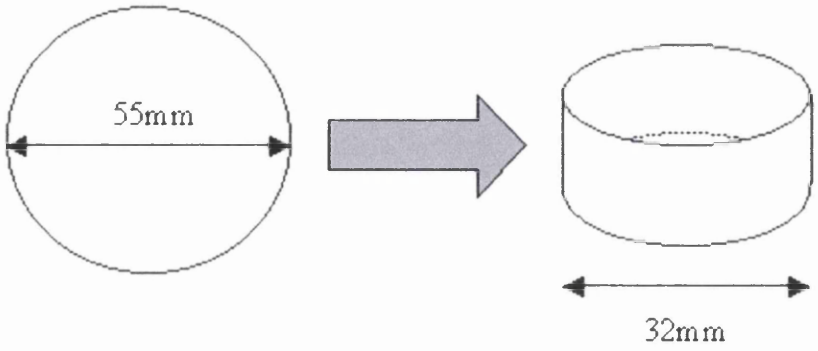

Figure 4.5. Starting disc and formed cup.

After deformation the cup was again ultra-sonically cleaned and 3M Scotch Brand Tape was applied to the outer surface of the cup. Upon removal of the tape the formed cup was then re-weighed on the Sartorious electronic balance. The difference in weight from the first weighing was then equal to the amount of coating that had become detached from the substrate during pressing.

4.5 ELECTRON BACKSCATTER DIFFRACTION

To assess and evaluate the influence of the underlying steel grain structure on the development of the galvanneal coating the process of electron backscatter diffraction (EBSD) was utilised.

4.5.1 EBSD Apparatus

The EBSD apparatus consists of five main components:

- SEM
- Diffraction (video) camera interfaced to a phosphor screen
- Camera control/diffraction pattern processor unit
- Computer
- Dedicated software to control data acquisition and processing

The electron beam from the SEM impinges upon the surface of the specimen at an angle of approximately 20°. This produces a diffraction pattern from the interaction between the electrons and the crystal lattice of the steel substrate.

The diffraction pattern is produced on the phosphor screen and is then turned into a digital image by the diffraction video camera. The digital image is then passed into the camera control/diffraction pattern processor unit where the image is further enhanced to produce a cleaner and more defined diffraction pattern. This diffraction pattern is then inputted into the computer where further analysis using a dedicated software package is carried out to calculate the orientation of the crystal lattice at the point being analysed. The electron beam is then moved an operator determined step-size and the process is repeated. This continues over a selected area to produce an orientation map of the specimen. A schematic diagram of the EBSD set-up is shown in figure 4.6.

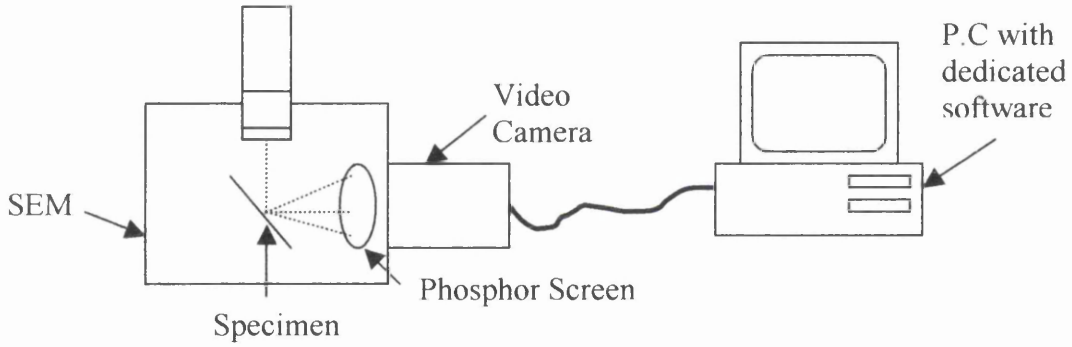

Figure 4.6. Schematic Diagram of the Electron Backscatter Diffraction Set-up.

4.5.2 Sample Preparation for EBSD Analysis

Samples for EBSD were taken as close to the thermocouple as was practically possible to ensure accurate temperature readings. The surface analysed was also that to which the thermocouple had been attached. A total of 4096 measurements were taken with each sample using a step size of approximately 3 microns. This allowed for an area approximately 192 microns squared to be analysed which is the equivalent of approximately 370 grains.

To produce a distinct clear image a cross-section of the sample to be analysed was mounted in a conductive resin and polished to an almost mirror finish using standard polishing techniques. The final preparation of the sample involved polishing with colloidal silica. Colloidal silica was used because it produces a very good mirror finish without causing severe deformation of the surface as would occur with diamond paste.

5 EXPERIMENTAL PROGRAMME

The following chapter details the materials used and the experimental work carried out to achieve the stated objectives.

5.1 OBJECTIVES

The primary objective of the project was to,

'investigate the iron-zinc coating constitution and crater evolution in galvanneal .'

Achieving this objective was accomplished through a series of five sequential experimental investigations.

1. Critical assessment of a quantative technique for analysing crater coverage in the galvanneal coating.
2. Investigation into the influence of process parameters on the crater coverage of the galvanneal coating produced on the Rhesca hot dip simulator.
3. Investigation into the characteristics, formation and development of craters within the galvanneal coating produced on the Rhesca hot dip simulator.
4. Investigation into the effect of craters upon the coating failure mechanism of the galvanneal coating produced on the Rhesca hot dip simulator.
5. Development and testing of a model, based on diffusion couples, to predict the coating constitution of the galvanneal coating produced on the Rhesca hot dip simulator.

5.2 MATERIALS

A titanium-niobium stabilised interstitial free (TiNb) steel produced at the Corus steelworks in Port Talbot was used for the vast majority of the experimental work. The steel was hot and cold rolled at the Port Talbot steelworks and obtained just prior to processing on the ZODIAC galvanising line at the Corus steelworks in Llanwern. The chemical composition of the steel is shown in table 5.1.

Table 5.1. Chemical analysis of TiNb IF steel.

Element	wt%
Carbon	0.002
Silicon	0.001
Manganese	0.160
Phosphorous	0.013
Sulphur	0.009
Nickel	0.018
Copper	0.010
Tin	0.001
Nitrogen	0.002
Sol. Aluminium	0.032
Chromium	0.011
Molybdenum	0.001
Niobium	0.016
Titanium	0.030
Vanadium	0.001

5.3 EXPERIMENTAL INVESTIGATION ONE

Critical assessment of a quantative technique for analysing crater coverage in the galvanneal coating.

Due to the extensive use of the technique for measuring crater coverage, as detailed in section 4.3, it was necessary to assess its accuracy and repeatability. This was achieved through four sets of work which were designed to determine:

1. The accuracy and repeatability of identifying and marking the edge of a single crater (Single Crater Analysis).
2. The accuracy and repeatability of identifying and marking all the craters within a single image (Single Image Analysis).

3. The variation of crater coverage over a single sample (Single Sample Analysis).
4. The variation of crater coverage between two sets of ten images from the same sample (Single Sample Double Image Analysis).

5.3.1 Single Crater Analysis

To assess the accuracy of identifying and marking individual craters a single crater was identified within an image of the galvanneal coating and the perimeter of the crater was drawn around ten times over a five-day period. The KS300 image analysis package was then utilised to calculate both the area and the perimeter of the crater each time.

5.3.2 Single Image Analysis

To assess the accuracy and consistently of identifying craters within a single image an image of the galvanneal coating, at a magnification of 300x, was loaded into the KS300 image analysis package. The craters within the image were then identified and drawn around on seven different occasions over a five-day period. The KS300 image analysis package was then utilised to calculate the crater coverage, total perimeter and number of craters for each of the seven measurements.

5.3.3 Single Sample Analysis

To assess the variation of crater coverage over a single sample ten images from random points over a sample were loaded into the KS300 image analysis package. The craters within each image were identified and the crater coverage calculated.

5.3.4 Single Sample Multiple Image Analysis

To assess the accuracy of taking ten images per sample ten sets of ten images were taken at random locations over the surface of a single sample. The craters within each

image were identified and the average crater coverage of each of the ten sets was calculated. The variation between the ten sets of images was then calculated.

5.4 EXPERIMENTAL INVESTIGATION TWO

Investigation into the influence of process parameters on the crater coverage of the galvanneal coating produced on the Rhesca hot dip simulator.

In order to gain a certain degree of control over the formation of craters within the galvanneal coating it was necessary to determine the influence that process parameters had upon the formation of craters. To achieve this three sets of experimental work were carried out:

1. A preliminary investigation into the effect of processing parameters upon the formation of craters within the galvanneal coating.
2. A partial statistically designed experiment analysing the interaction between four of the main temperature effects
3. A full statistically designed experiment analysing the interaction between three temperature effects.

5.4.1 Preliminary Investigation into Process Parameter Effects

Based upon both the literature review and previous work the initial experiment analysed four main process parameters, the spelter temperature, the heating rate to 500°C after dipping, the effective aluminium and the galvannealing temperature. The standard processing conditions utilised during this experiment are shown in table 5.2

Table 5.2. Standard conditions for preliminary investigation.

Process Parameter	Value
Annealing Temperature (°C)	800
Annealing Time (s)	60
Strip Entry Temperature (°C)	10°C above spelter
Spelter Temperature (°C)	455
Heating Rate to 500°C (°C/s)	50
Galvannealing Time (s)	8
Galvannealing Temp (°C)	510
Eff. Al of Spelter (wt%)	0.94
Coating Thickness (microns)	8
Iron Content (wt%)	10

The process parameters to be investigated were then modified around these standard conditions and carried out in duplicate. The variation of the process parameters is shown in table 5.3.

Table 5.3. Variation in process parameters for preliminary investigation.

Process Parameter	Variation
Spelter Temperature (°C)	430, 440, 450, 460
Heating Rate to 500°C (°C/s)	2, 4, 8, 12, 15
Eff. Al of Spelter (wt%)	0.10, 0.12, 0.14, 0.16, 0.18
Galvannealing Temperature (°C)	440, 510, 520, 530, 550

5.4.2 Partial Statistical Interaction Analysis

Following on from the previous work eight panels of galvannealed TiNb IF steel were produced on the Rhesca hot dip simulator to investigate the effects of annealing temperature, strip entry temperature, spelter temperature and galvannealing temperature upon crater formation. Table 5.4 shows the process conditions used for each of the panels.

Table 5.4. Process parameters for partial statistical interaction analysis.

Process Parameter	1	2	3	4	5	6	7	8
Annealing Temperature (°C)	780	850	780	850	850	780	850	780
Strip Entry Temperature (°C)	460	460	480	460	480	480	480	460
Spelter Temperature (°C)	460	480	480	480	460	480	460	460
Galvannealing Temperature (°C)	510	510	510	500	500	500	510	500
Heating Rate to GA Temp (°C/s)	10	10	10	4	4	4	10	4
GA Time (s)	8	8	8	2	2	2	8	2

The effective aluminium content of the spelter was maintained at 0.108 wt% and the samples were all annealed for 60 seconds at the respective temperatures. To ensure each of the samples was galvannealed to the same degree, even though different galvannealing temperatures were used, the galvannealing time and heating rate were modified as shown.

5.4.3 Full Statistical Interaction Analysis

As a result of the work accomplished a full statistical interaction analysis of the annealing temperature and the strip entry temperature was carried out. Furthermore, an interaction between the crater coverage and the lowest temperature reached after dipping (TAD) was suspected. The temperature after dipping (TAD) was therefore included within the full statistical interaction analysis experiment along with the strip entry temperature and annealing temperature. Table 5.5 shows the process conditions utilised during the experiment.

Table 5.5. Process parameters for statistical interaction analysis.

Process Parameter	1	2	3	4	5	6	7	8
Strip Entry Temperature (°C)	480	480	480	480	430	430	430	430
Temperature After Dipping (°C)	440	440	410	410	440	440	410	410
Annealing Temperature (°C)	900	700	900	700	900	700	900	700

All of the conditions shown in table 5.5 were carried out in triplicate. The temperature of the spelter was held at 460°C and the effective aluminium content at 0.108 wt%. The annealing for all the samples was carried out for sixty seconds and the galvannealing conditions were maintained at 500°C for 10 seconds.

As well as investigating the effects of strip entry temperature, temperature after dipping and annealing temperature an additional set of work was carried out on the effect of the aluminium content of the spelter upon crater formation. This involved using two levels of effective aluminium content, 0.1wt% and 0.113wt%. The annealing temperature and strip entry temperature were modified between the high and low states with the temperature after dipping maintained at the low state.

5.5 EXPERIMENTAL INVESTIGATION THREE

Investigation into the characteristics, formation and development of craters within the galvanneal coating produced on the Rhesca hot dip simulator.

Under similar processing conditions craters are observed within the galvanneal coating but not within the galvanised coating. Therefore, to further investigate the formation of craters within the galvanneal coating and how they develop during the galvannealing process panels of TiNb IF steel were galvannealed on the Rhesca hot dip simulator for varying degrees of time. Using the results from section 5.4 the process conditions utilised during this experiment were manipulated to enhance the crater formation within the coating and are shown in table 5.6. In order to investigate the formation of both ordered and disordered craters two different effective aluminium contents and strip entry temperatures were utilised.

To further understand the formation of craters within the galvanneal coating a marker was placed within the samples that went through the coating and down to the substrate. Images of the coating surface were taken at specific points around the marker using the JEOL 810A SEM. The coating was then removed with inhibited hydrochloric acid and the exposed substrate etched with 5% Nital for twenty seconds.

Images of the underlying substrate were then taken at the same specified points around the marker that the coating images had been taken.

Table 5.6. Process conditions for crater development experiment.

Process Parameter	Value (ordered)	Value (disordered)
Annealing Temperature (°C)	900	900
Annealing Time (s)	60	60
Strip Entry Temperature (°C)	465	455
Spelter Temperature (°C)	460	460
Effective Aluminium (wt%)	0.1	0.113
Heating Rate (°C/s)	50	50
Galvannealing Temp (°C)	500	500
Galvannealing Time (s)	0 to 14	0 to 14

In addition to the SEM images, optical and EBSD work was also carried out upon the underlying substrate on samples that had been annealed at 700°C and 900°C on the Rhesca hot dip simulator but which had not undergone any form of dipping

Finally, over 4,000 craters were measured to obtain a size distribution of craters within the galvanneal coating.

5.6 EXPERIMENTAL INVESTIGATION FOUR

Investigation into the effects of craters upon the coating failure mechanism of the galvanneal coating produced on the Rhesca hot dip simulator.

Previous work (Carless, 1999) has suggested that the presence of craters within the galvanneal coating may help to reduce the amount of powdering experienced during deformation procedures. Work from the previous investigation showed how the annealing temperature affected both the crater coverage of the galvanneal coating and the microstructure of the underlying substrate. Manipulation of both the annealing temperature and the galvannealing temperature facilitated the production of samples

with both high and low annealing temperature and high and low crater coverage. This would therefore enable the effects of the annealing temperature and the crater coverage to be investigated both separately and in conjunction with each other. In addition the effect of iron content and coating weight upon both the powdering and flaking properties of the coating was also investigated.

Furthermore, the formed cups were also analysed under the scanning electron microscope to investigate how both the coating and craters had performed during deformation. Images were taken from inside and outside of the cup at the locations shown in figure 5.1.

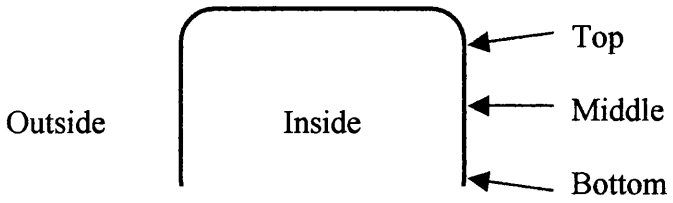

Figure 5.1. Schematic diagram of sampling positions.

Further investigative work was also carried out on the underlying substrate by dissolving the overlying galvanneal coating with inhibited hydrochloric acid. Images of the underlying substrate were then taken from the outside of the cup at the locations shown in figure 5.1

5.7 EXPERIMENTAL INVESTIGATION FIVE

Development and testing of a model, based on diffusion couples, to predict the coating constitution of the galvanneal coating produced on the Rhesca hot dip simulator.

The principle of diffusion couples was utilised to produce a model to predict the formation of the galvanneal coating. One of the main parameters that needed to be determined in order for the model to work was the diffusion co-efficient of iron in zinc. This was calculated by SEM elemental mapping of the iron content of a low aluminium galvanneal coating that had been galvannealed for ten seconds at 500°C.

By plotting the log of the iron concentration against the square of the distance into the coating, as detailed in section 3.2.2, the diffusion coefficients for the different phases could be determined. The results obtained could then be compared to the published values of D_o and Q as detailed in table 3.1.

For ease of use and portability the GAModeller was created in the Microsoft Visual Basic™ programming language (see appendix A). This enabled the production of an easy to use graphical user interface (GUI) as well as the rapid calculation and graphical representation of the coating constitution.

Once this initial stage was completed final testing and validation of the model was achieved by producing panels of galvannealed TiNb IF steel on the Rhesca hot dip simulator under the conditions shown in table 5.7.

Table 5.7. Process parameters used for GAModeller testing.

Process Parameter	**Value**
Annealing Temperature (°C)	800
Annealing Time (s)	60
Strip Entry Temperature (°C)	465
Spelter Temperature (°C)	455
Coating Thickness (microns)	20

The effective aluminium of the spelter, the galvannealing temperature and galvannealing time were all then varied for each panel, as shown in table 5.8.

The coating constitution of the panels was then analysed using X-Ray Diffraction (Angeli *et al.*, 1993). The two sets of published values for D_o and Q of zinc in aluminium, as detailed in section 3.2.4, were then individually used within the GAModeller and the results compared with the XRD work to see which set gave the best results.

Table 5.8. Variation of process parameters for GAModeller testing.

Panel ID	Eff Al.	Galv. Temp	Galv. Time
GAM1	0.108	506	4
GAM2	0.108	534	20
GAM3	0.108	410	3
GAM4	0.108	417	8
GAM5	0.108	446	18
GAM6	0.108	556	6
GAM7	0.108	577	16
GAM8	0.108	489	20
GAM9	0.108	546	14
GAM10	0.108	585	18
GAM11	0.108	565	5
GAM12	0.12	476	1
GAM13	0.12	540	2
GAM14	0.12	561	16
GAM15	0.12	508	16
GAM16	0.12	440	7
GAM17	0.12	440	7
GAM18	0.12	451	11
GAM19	0.12	451	11
GAM20	0.12	491	6
GAM21	0.12	578	4
GAM22	0.12	483	16
GAM23	0.12	596	4
GAM24	0.12	596	4
GAM25	0.14	553	11
GAM26	0.14	485	17
GAM27	0.14	405	4
GAM28	0.14	496	8
GAM29	0.14	450	2
GAM30	0.14	452	4
GAM31	0.14	544	1
GAM32	0.14	544	1
GAM33	0.14	576	2
GAM34	0.14	488	7
GAM35	0.14	591	12
GAM36	0.14	483	20
GAM37	0.14	414	8
GAM38	0.16	482	19
GAM39	0.16	419	11
GAM40	0.16	412	1
GAM41	0.16	409	12
GAM42	0.16	563	5
GAM43	0.16	573	6
GAM44	0.16	428	16
GAM45	0.16	505	17
GAM46	0.16	440	18
GAM47	0.16	413	13
GAM48	0.108	506	4

6 RESULTS AND DISCUSSION

The following chapter contains the experimental results and discussion for each of the individual investigations.

6.1 EXPERIMENTAL INVESTIGATION ONE

Critical assessment of a quantative technique for analysing crater coverage in the galvanneal coating.

Due to the extensive use of this technique, and as stated in section 5.3, this investigation was carried out to determine the errors involved with using the KS300 image analysis package to measure the crater coverage within the galvanneal coating.

6.1.1 Single Crater Analysis

Table 6.1 details the results from the single crater analysis that was carried out to determine the accuracy of identifying and marking the edge of a single crater using the KS300 image analysis package.

From the ten measurements carried out the average area of the single crater was calculated as 851.7μm^2 and the average perimeter 182.8 microns. The smallest area was 828μm^2 and the largest area 876μm^2. The largest perimeter measured was 190 microns and the smallest 177 microns. Over the ten images taken the standard deviation for the area was 16.7μm^2 and for the perimeter 4.4 microns. For three standard deviations the variation of the area for the ten measurements was ±5.9% of the average and for the perimeter ±7.3% of the average.

Table 6.1. Experimental results from single crater analysis

Measurement	Area (μm^2)	Perimeter (μm)
1	835	180
2	859	177
3	846	176
4	836	187
5	855	185
6	874	190
7	843	182
8	876	188
9	865	182
10	828	181
Average	851.7	182.8
σ	$\pm$16.7	$\pm$4.4
3σ	$\pm$50.1	$\pm$13.2
% of Average	$\pm$5.9	$\pm$7.3

Analysis of the results and figure 6.1 show that the size of the measured area is not proportional to the size of the perimeter. For example, although measurement ten gives the smallest area it does not give the smallest perimeter. Figure 6.1 shows the relationship between the measured area and the measured perimeter. A general trend is observed whereby an increase in the perimeter results in an increase in the area. However, a large amount of scatter is observed within the data, as shown by the low R^2 value.

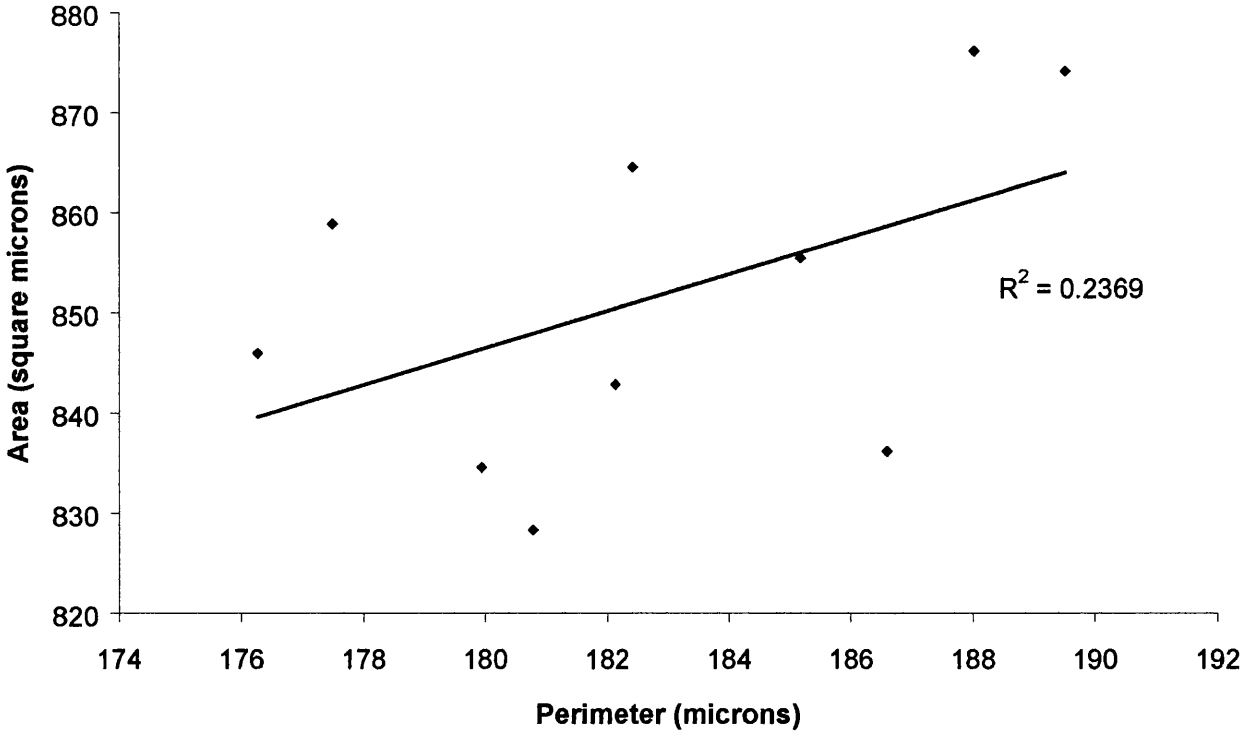

Figure 6.1. Correlation of measured crater area and perimeter for single crater analysis.

The results from this investigation have shown that the KS300 image analysis technique is sufficiently accurate in consistently determining and calculating the area of an individual crater. The large scatter observed in figure 6.1 is explained by the very rough and irregular shape of the representative crater used to carry out the investigation. While defining the edge of the crater with the image analysis package small corners of the crater may be omitted thus varying the relationship between the measured area and the measured perimeter.

6.1.2 Single Image Analysis

Table 6.2 details the experimental results obtained by taking a single image of the galvanneal coating and determining its crater density. This was carried out to determine the accuracy of identifying and measuring craters within the galvanneal coating using the KS300 image analysis package.

The average total area of crater coverage was 9599.0μm² or 7.84% of the total image and ranged from as low as 8492μm² to as high as 10624μm². The total perimeter of all the measured craters was on average 3049.7μm ranging from 2901μm to 3305μm. Furthermore, the strong positive correlation between the total perimeter and the area is shown in figure 6.2. An R^2 value of 0.6867 shows considerably less scatter than the correlation for the single image analysis shown in figure 6.1. In addition, the number of craters measured is seen to vary from as low as fifteen craters to as high as nineteen craters over the seven measurements.

Table 6.2. Experimental results from single image analysis

Measurement	Area (μm^2)	Area (%)	Total Perimeter (μm)	Number of Craters
1	8880	7.3	2901	15
2	10268	8.4	3067	16
3	9584	7.8	2903	15
4	9369	7.7	3125	17
5	10624	8.7	3305	17
6	8492	6.9	2829	15
7	9976	8.2	3218	19
Average	9599.0	7.84	3049.7	16.3
σ	±700.6	±0.57	±165.5	±1.4
3σ	±2101.8	±1.71	±496.5	±4.2
% of Average	±21.9	±21.90	±16.3	±25.5

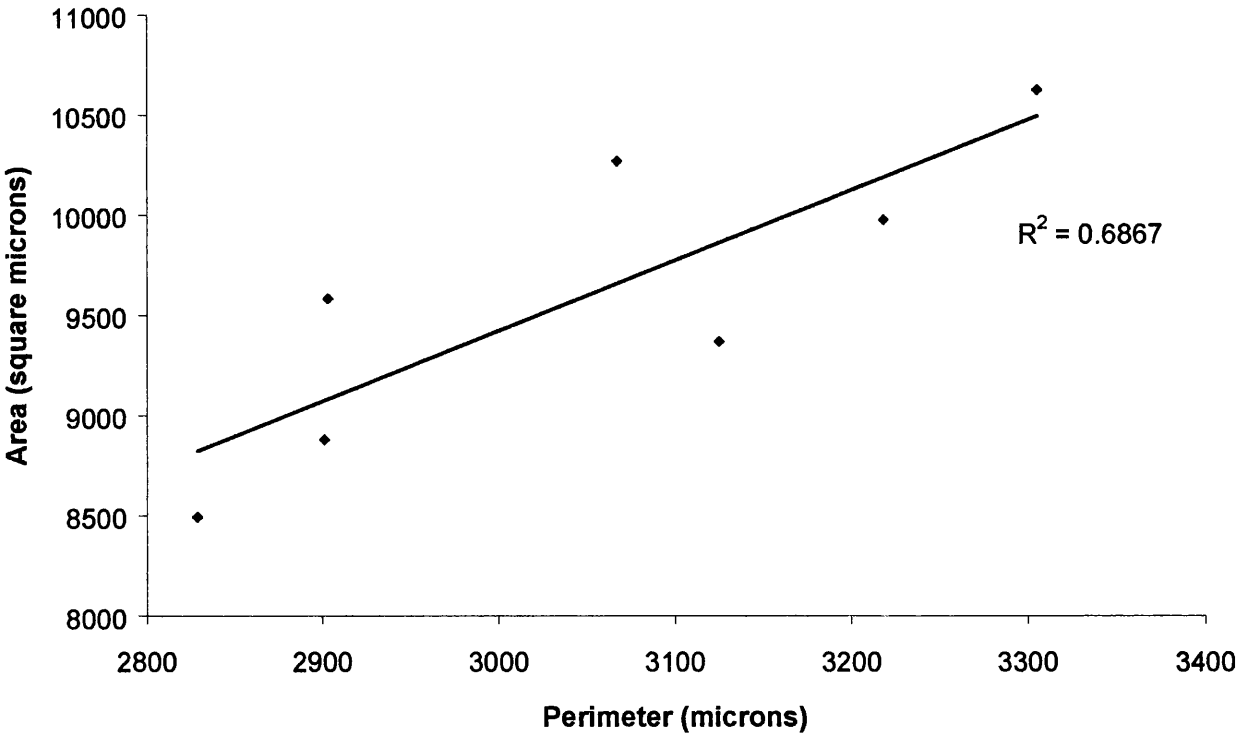

Figure 6.2. Correlation between total perimeter and measured area for the single sample analysis.

6.1.3 Single Sample Analysis

Table 6.3 details the experimental results from the single sample analysis whereby ten images from different areas of the sample were taken and the crater coverage analysed. This was carried out to determine the variation of crater coverage over a single sample.

The average total area covered by craters was 7817.6 μm^2 or 6.39%. This varied from as low as 4798μm^2 in image four to as high as 16524μm^2 in image six. This large variation between images produced a standard deviation of $\pm$3328.4μm^2 or $\pm$127.73% of the average for three standard deviations.

Table 6.3. Experimental results from single sample analysis

Image No.	Area (μm^2)	Area (%)
1	9743	8.0
2	6732	5.5
3	5484	4.5
4	4798	3.9
5	9913	8.1
6	16524	13.5
7	6973	5.7
8	5422	4.4
9	6156	5.0
10	6431	5.3
Average	7817.6	6.39
σ	±3328.3	±2.72
3σ	±9984.9	±8.16
% of Average	±127.7	±127.7

The results from this investigation show the large variation in crater coverage across the single sample analysed. The results also illustrate the fact that taking a single image does not give an accurate indication of the crater coverage of the whole sample.

6.1.4 Single Sample Multiple Image Analysis

Table 6.4 details the experimental results from the single sample multiple image analysis. Ten sets of ten images were analysed for crater coverage and the average coverage calculated from each set. This was carried out to determine whether or not taking ten images would give an accurate representation of the crater coverage.

The average of all one hundred images was 9.8% coverage with the individual sets ranging from as low as 9.5% to as high as 10.0%. This range of values equates to a standard distribution value of just 0.2%.

Table 6.4. Experimental results for single sample multiple image analysis

Set	Average Area Coverage (%)
1	10.0
2	9.7
3	9.8
4	9.8
5	9.9
6	9.5
7	9.6
8	9.8
9	9.5
10	10.1
Average	9.77
σ	0.21
3σ	0.63
±% of Average	6.54

6.1.5 Discussion

The results from table 6.1 show that the errors associated with identifying and marking the edge of a crater are minimal. For three standard deviations the variation of the area for the ten measurements was just ±5.9% of the average and for the perimeter just ±7.3% of the average. The lack of correlation between the measured perimeter and the measured area in figure 6.1 is a result of the rough and irregular shape of the crater used in the investigation. While determining the edge of a crater it is possible to miss out parts of the crater thus affecting the relationship between the perimeter and the area.

When the results from the single image are analysed, table 6.2, it is clear to see that a moderate error is experienced. The different measurements for the total crater coverage for a single image varied from as low as 8492μm^2 to as high as 10624μm^2. For three standard deviations this was equal to ±2101.8μm^2 or ±21.9% of the average.

This moderate error is associated with the problem of consistently identifying what is and what is not a crater. This is illustrated firstly by the variation in the actual number of craters identified for each measurement and secondly by the fact that the measurement with the highest number of craters does not have the highest crater coverage. For example a comparison between measurements two and seven shows that although measurement seven identified 19 craters and crater coverage of 9976μm^2 measurement two identified just 16 craters but had a coverage of 10268μm^2. The improved correlation observed in figure 6.2 between the total perimeter and the total area, as compared to figure 6.1, is explained by the fact that taking measurements from several craters masks the error associated with determining the exact edge.

Table 6.3 shows the results from the single sample analysis whereby ten surface images were taken from a single sample and analysed for crater coverage. The results show a large variation in the crater coverage across the images going from as low as 4798μm^2 to as high as 16524μm^2. For three standard deviations this equates to $\pm$9984.9μm^2 or $\pm$127.7% of the average. This shows that across a single sample of galvanneal there is considerable variation in the crater coverage and that when measuring the coverage of a sample it is not possible to measure just a single image.

The results from the single sample multiple image analysis whereby ten sets of ten images were taken from a single sample of galvanneal are shown in table 6.4. The variation between the ten sets of images is seen to be negligible and over three standard deviations the variation in crater coverage is just $\pm$0.6μm^2 or $\pm$6.54% of the average. These results show that by taking ten images of the surface of the galvanneal coating a true representation of the crater coverage can be achieved.

6.1.6 Summary

This investigation has developed and tested a technique for identifying and measuring craters within the galvanneal coating. The technique of measuring the crater coverage within the galvanneal coating by taking ten SEM images of the surface and using an image analysis package has proved to be satisfactory. Care and attention needs to be exercised when identifying craters and although time consuming the technique gives

valuable information about crater size and morphology as well as an error of just ±6.54%.

6.2 EXPERIMENTAL INVESTIGATION TWO

Investigation into the influence of process parameters on the crater coverage of the galvanneal coating produced on the Rhesca hot dip simulator.

As stated in section 5.4 this experimental investigation was carried out to gain greater understanding of the influence of process parameters upon the crater coverage within the galvanneal coating. During this investigation the manipulation of the various process parameters resulted in a change in the morphology of the craters that were observed. Whereas previously just an ordered structure had been observed at the base of the crater during the investigation a more random and disordered structure was also observed, figure 6.22. The different craters will now be referred to as ordered craters for those with an ordered structure at their base and disordered craters for those with a random and disordered structure at their base. During the preliminary and partial investigation just the total crater coverage was measured, including both the ordered and disordered craters. However, with the full statistical analysis the ordered and disordered craters were treated as separate features in an attempt to discover the reason behind the change in morphology.

6.2.1 Preliminary Investigation into Process Parameter Effects

Figure 6.3 details the experimental results from the preliminary investigation into the effect of process parameters upon the formation of craters within the galvanneal coating.

Consistently low crater coverage was observed for the majority of the samples except for those with high effective aluminium content and in one instance when the spelter temperature was at 460°C. The highest crater coverage was approximately 12% and occurred when the effective aluminium content was 0.127wt%. Variation of the heating rate from 2°C s^{-1} to 15°C s^{-1} under these process conditions consistently gave zero crater coverage. A similar result was also experienced when the galvannealing temperature increased from 440°C to 550°C. In addition, modification of the spelter temperature from 430°C to 460°C had no influence upon crater coverage.

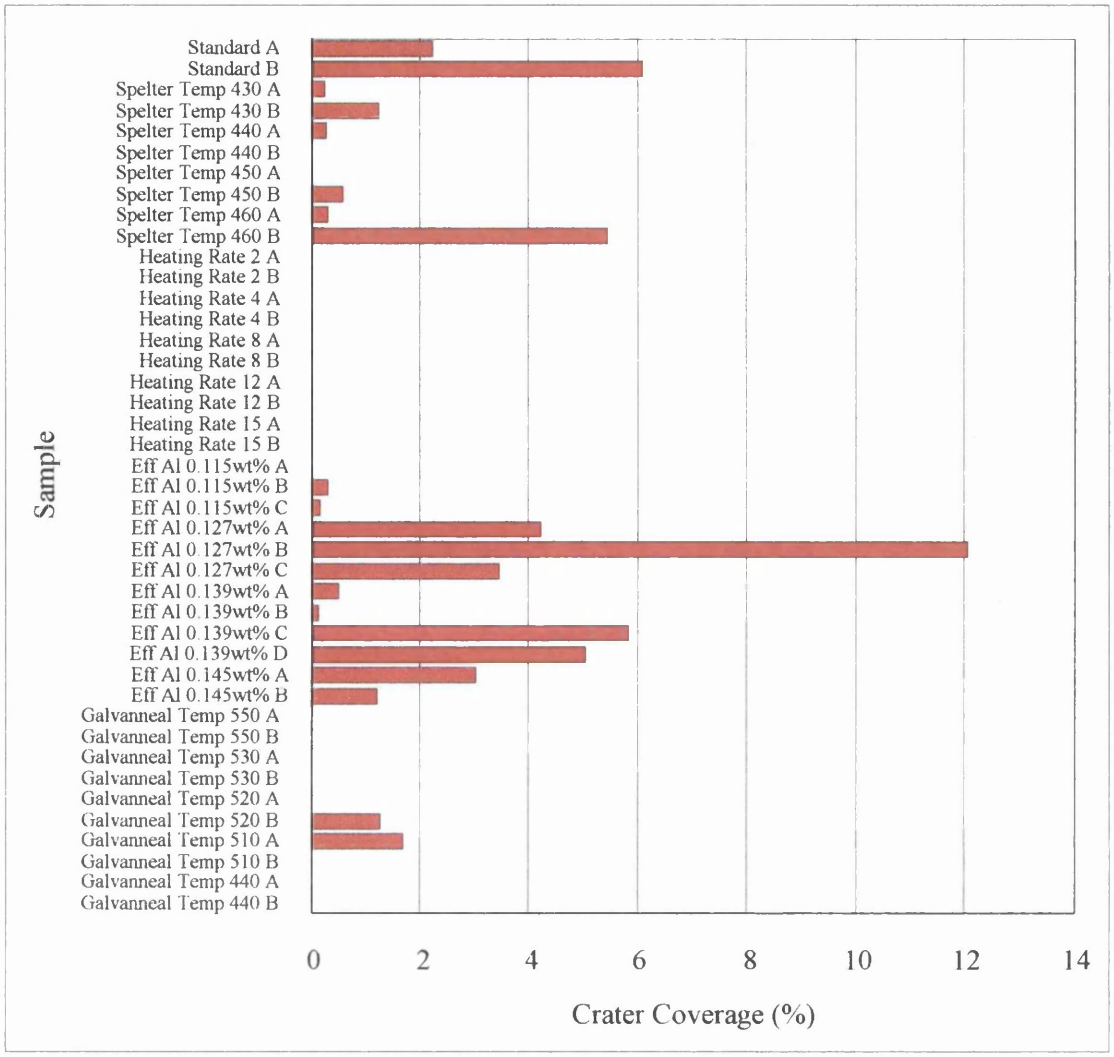

Figure 6.3. Experimental results from preliminary investigation.

6.2.2 Partial Statistical Interaction Analysis

Figures 6.4 to 6.7 chart the experimental data from the partial statistical interaction analysis carried out to further investigate the influence of process parameters upon the formation of craters within the galvanneal coating.

To keep the legends on the graphs to an acceptable size the following key code has been used:

ANN = Annealing temperature BT = Bath/Spelter temperature

GAT = Galvannealing temperature SET = Strip entry temperature

TAD = Temperature after dipping

Figure 6.4 shows the zero correlation between the bath temperature and the crater coverage within the samples. A galvannealing temperature of 500°C (as ○,◇ in figure 6.4) produces samples with a greater crater coverage compared to a galvannealing temperature of 510°C (as □, △ in figure 6.4).

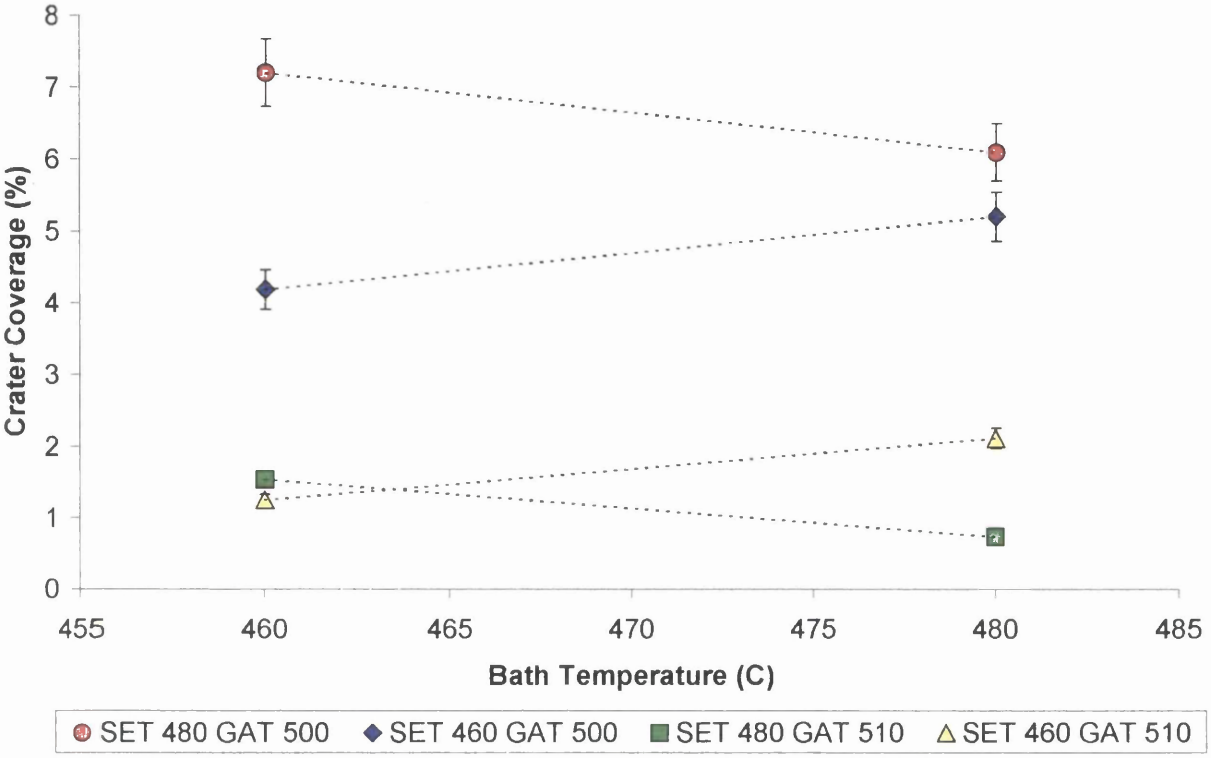

Figure 6.4. The effect of bath temperature upon crater coverage.

Figure 6.5 illustrates a strong positive correlation between the annealing temperature of the sample and the crater coverage. In all cases an increase in the annealing temperature produces an increase in the crater coverage of the sample. The average gradient for all the lines is equal to 0.0136 and represents a 0.0136 increase in the percentage crater coverage for each 1°C increase in annealing temperature. It can also be seen that a galvannealing temperature of 500°C (as ○, ◇ in figure 6.5) produces higher crater coverage than a galvannealing temperature of 510°C (as △, □ in figure 6.5).

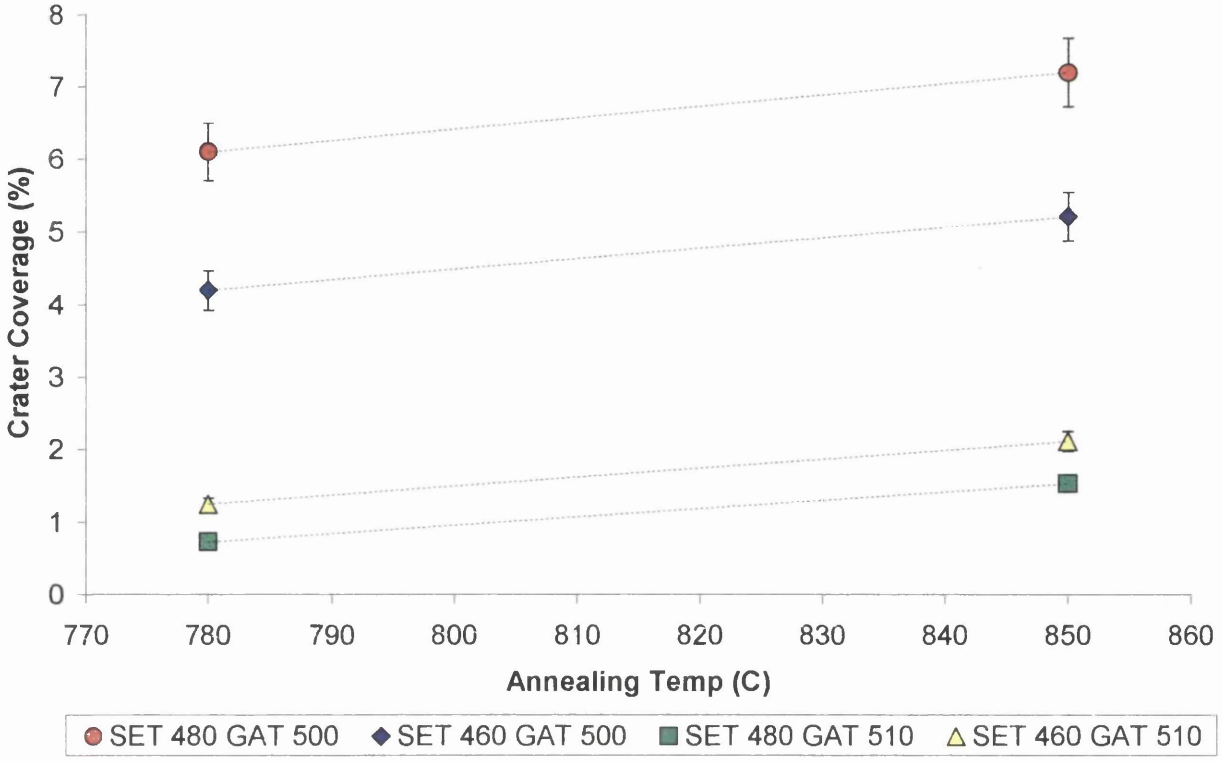

Figure 6.5. The effect of annealing temperature upon crater coverage.

Figure 6.6 illustrates the relationship between the strip entry temperature and the crater coverage of the samples analysed. When the galvannealing temperature is at 500°C (as ○, ◇ in figure 6.6) the overall crater coverage is greater, in addition an increase in the strip entry temperature results in an increase in the crater coverage. The average gradient of the two lines is equal to 0.097 and represents a 0.097 increase in the percentage crater coverage for each 1°C increase in the strip entry temperature.

However, when the galvannealing temperature is at 510°C (as △, □ in figure 6.6) an overall lower crater coverage is seen and an increase in the strip entry temperature leads to a decrease in the crater coverage. The average gradient of the two lines is equal to –0.028 and represents a 0.028 decrease in the percentage crater coverage for each 1°C increase in the strip entry temperature.

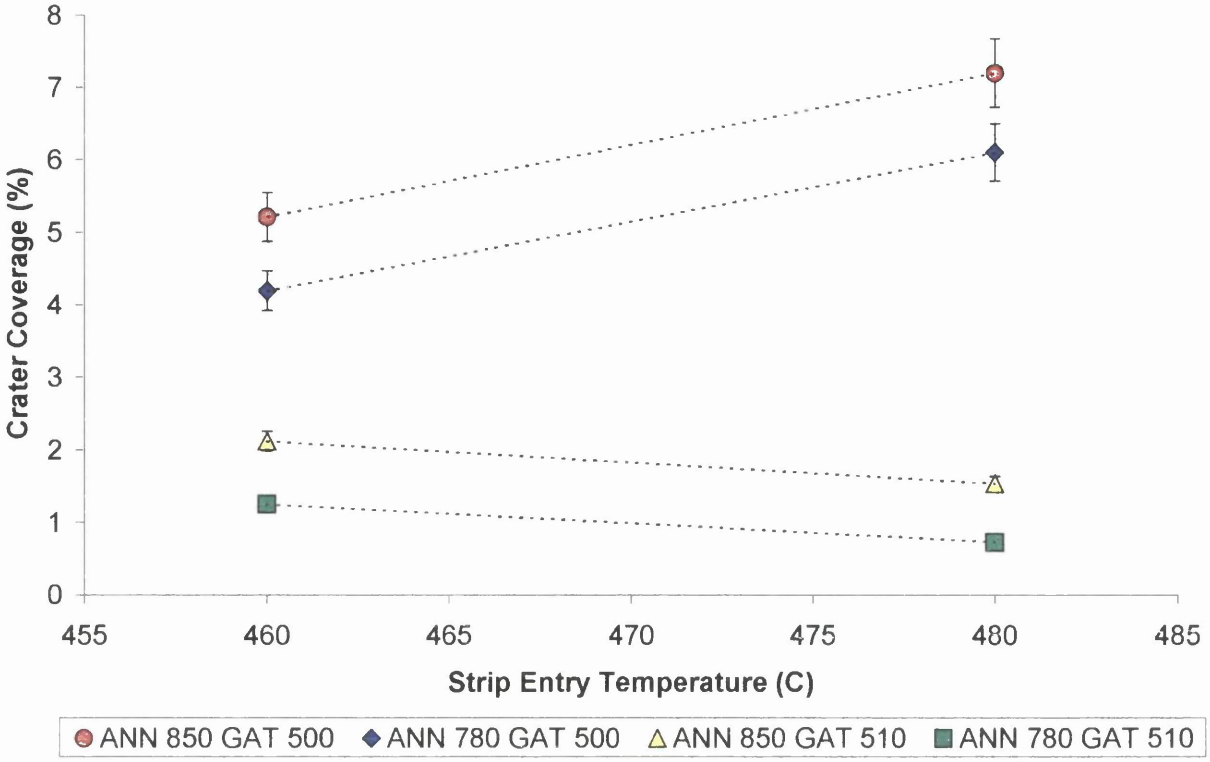

Figure 6.6. The effect of strip entry temperature upon crater coverage.

Figure 6.7 shows the strong correlation between the galvannealing temperature and the crater coverage of the samples analysed. It can be clearly seen that an increase in the galvannealing temperature results in a decrease in the crater coverage. However, the degree to which the crater coverage decreases appears to be dependent upon the strip entry temperature. With a strip entry temperature of 480°C the average gradient of the lines is equal to -0.552 and represents a 0.552 decrease in the percentage crater coverage for each 1°C increase in the galvannealing temperature. However, with a strip entry temperature of 460°C the average gradient of the lines is –0.302 and represents a 0.302 decrease in the percentage crater coverage for each 1°C increase in strip entry temperature.

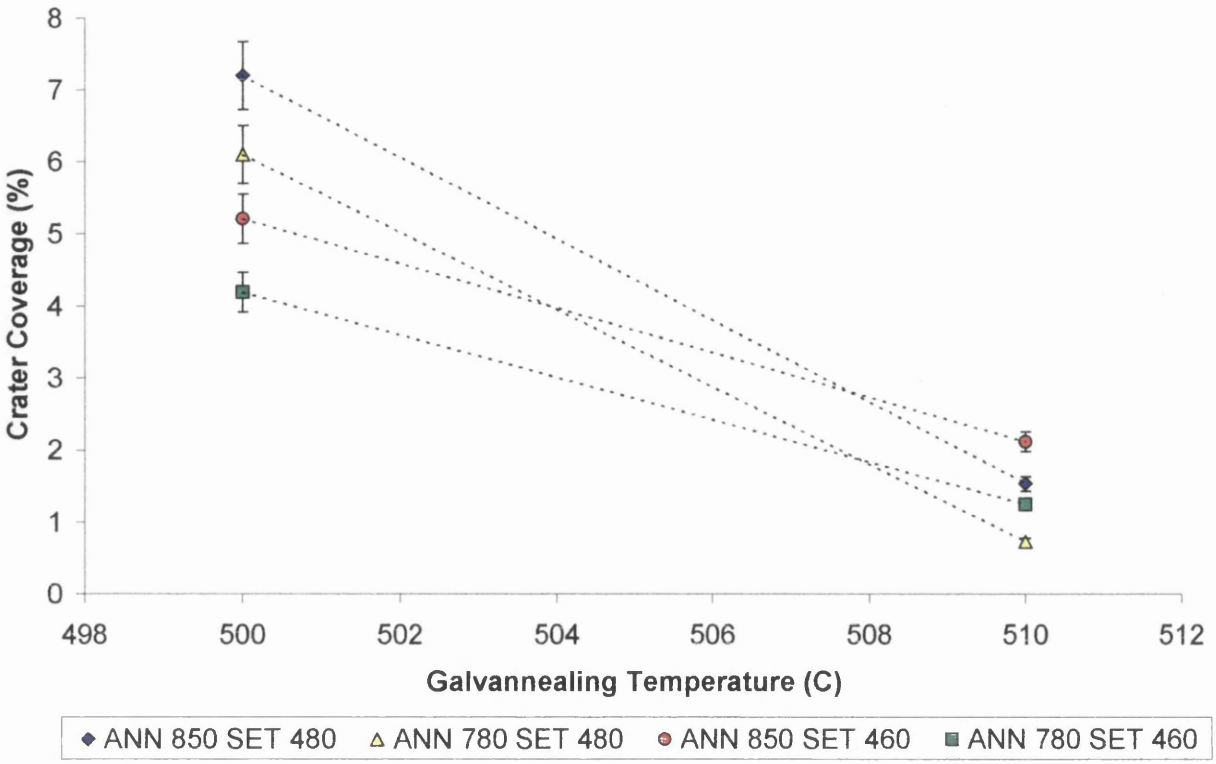

Figure 6.7. The effect of galvannealing temperature upon crater coverage.

6.2.3 Full Statistical Interaction Analysis

Figures 6.8 to 6.17 detail the experimental results obtained from the full statistical interaction analysis.

Strip Entry Temperature (SET)

Figure 6.8 shows the effect of strip entry temperature upon the ordered crater coverage within the galvanneal coating produced on the Rhesca hot dip simulator. When a high annealing temperature of 900°C is utilised (as ○, □ in figure 6.8) it can be seen that an increase in the strip entry temperature leads to an increase in the ordered crater coverage. However, when a low annealing temperature of 700°C is used (as ◇, △ in figure 6.8) the coverage of ordered craters remains zero even when the strip entry is increased.

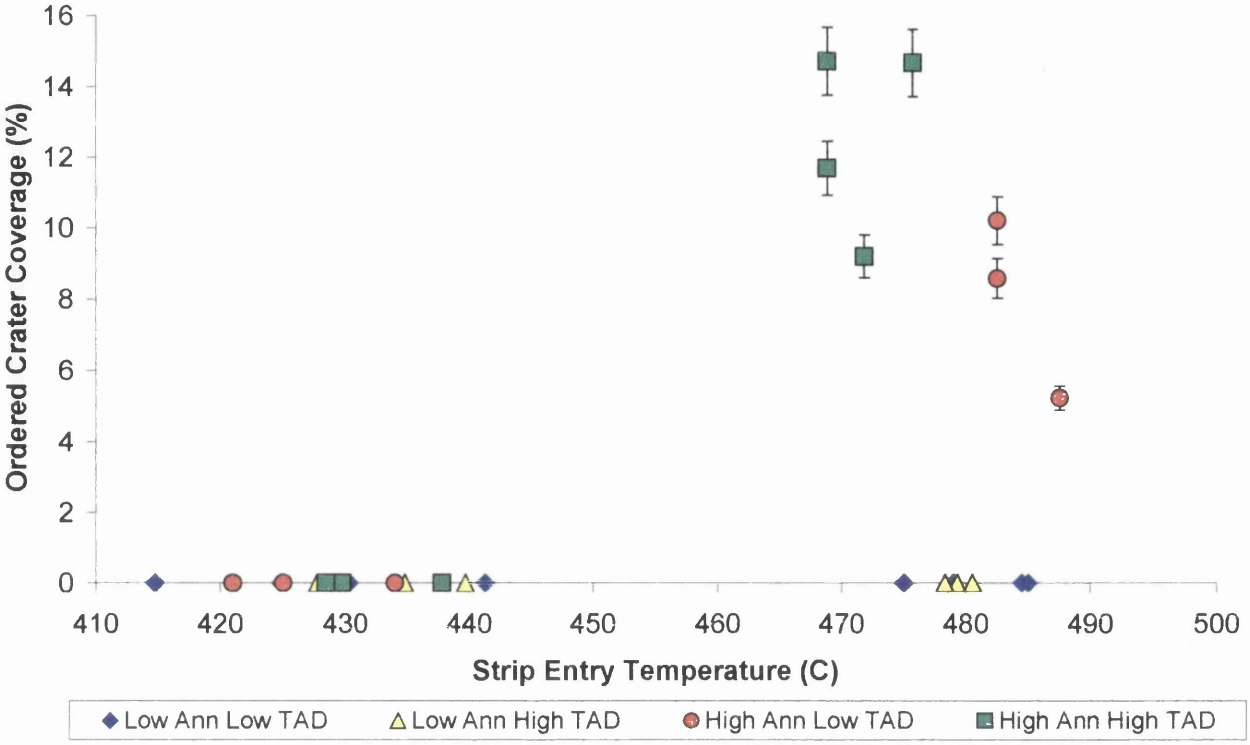

Figure 6.8. The effect of strip entry temperature upon ordered crater coverage.

Figure 6.9 illustrates the effect of strip entry temperature upon the coverage of disordered craters within the galvanneal coating produced on the Rhesca hot dip simulator. When a high annealing temperature is used (as ○, □ in figure 6.9) an increase in the strip entry temperature results in a decrease in the coverage of disordered craters. When a low annealing temperature is used (as ◇, △ in figure 6.9) the coverage of disordered craters is unaffected by the variation in strip entry temperature.

Figure 6.10 shows the effect of strip entry temperature upon the combined crater coverage of both disordered and ordered craters. A high annealing temperature (as ○, □ in figure 6.10) produces a higher crater coverage compared to a low annealing temperature (as ◇, △ in figure 6.10). Modifying the strip entry temperature has no effect upon the total crater coverage within the galvanneal coating.

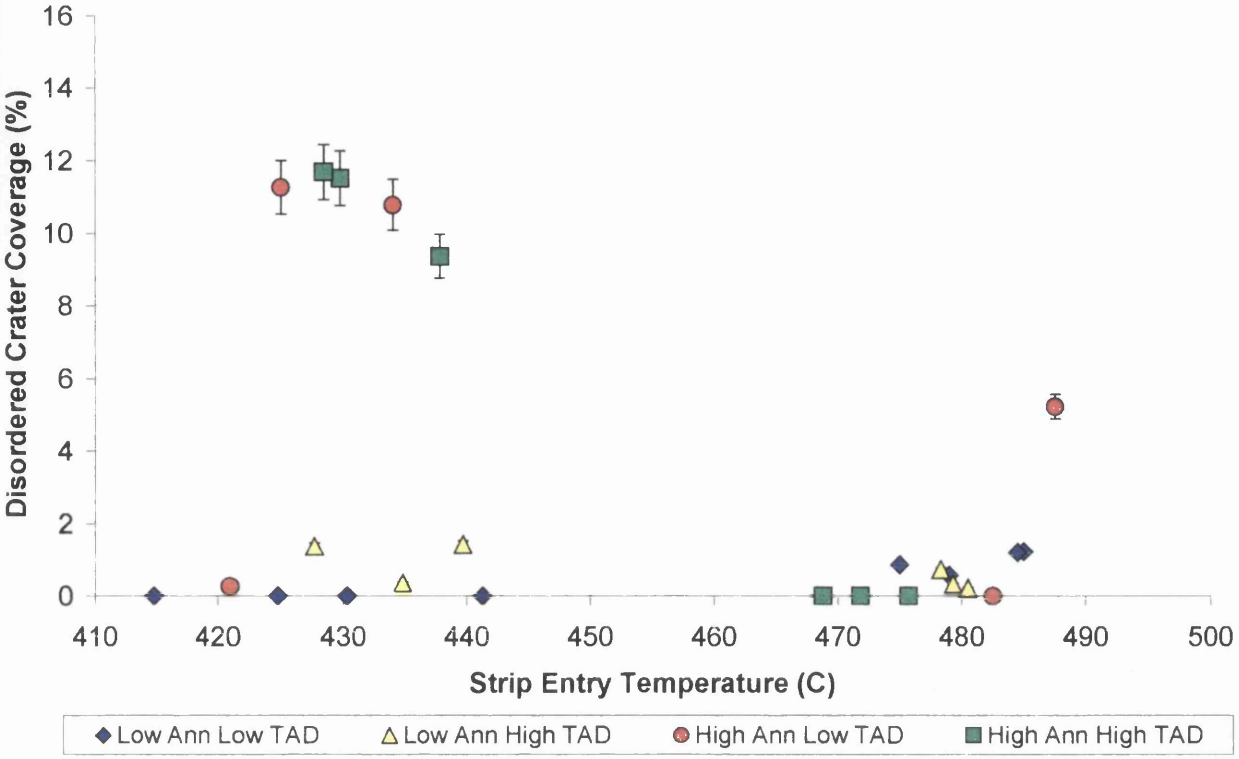

Figure 6.9. The effect of strip entry temperature upon disordered crater coverage.

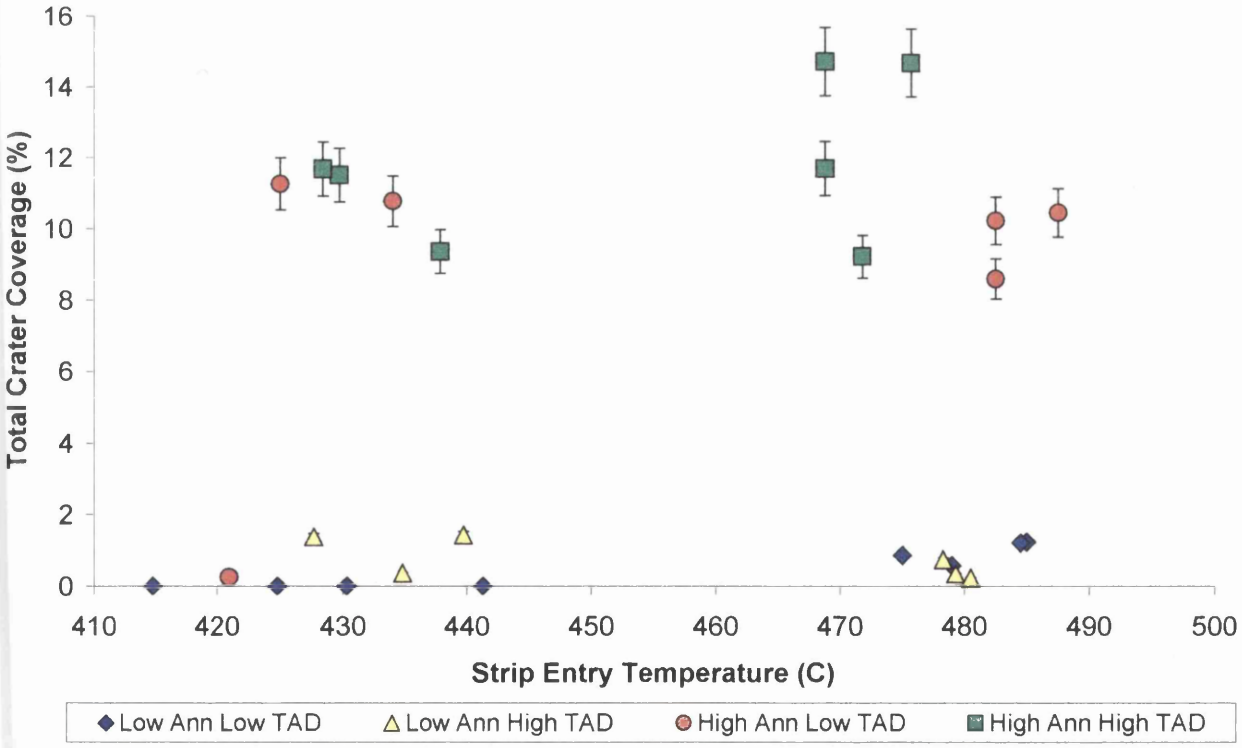

Figure 6.10. The effect of strip entry temperature upon total crater coverage.

Annealing Temperature

Figure 6.11 shows the influence of annealing temperature on the coverage of ordered craters within the galvanneal coating. A definite strong positive relationship can be observed whereby an increase in the annealing temperature from 700°C to 900°C produces an increase in the crater coverage. The highest crater coverage is experienced with samples with both a high annealing temperature and a high strip entry temperature (as □, △ in figure 6.11).

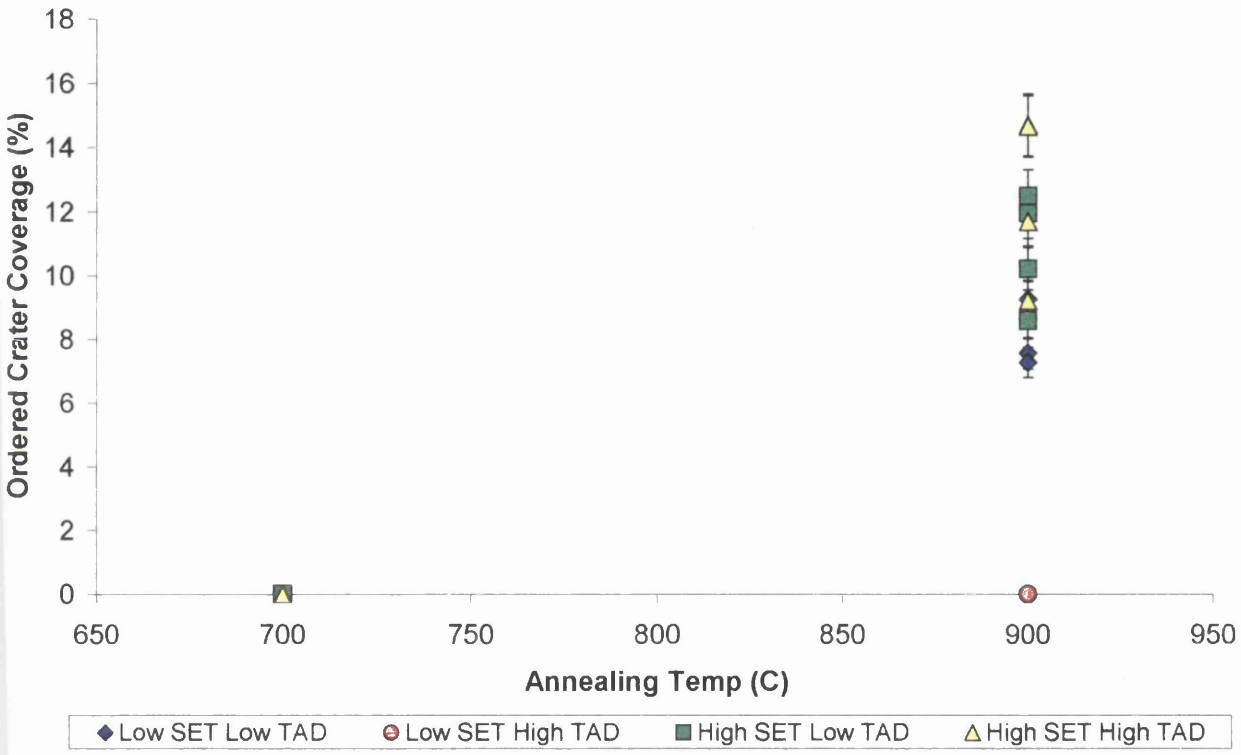

Figure 6.11. The effect of annealing temperature upon ordered crater coverage.

Figure 6.12 details the effect of annealing temperature upon the coverage of disordered craters within the galvanneal coating. An increase in the annealing temperature combined with a low strip entry temperature produces an increase in the disordered crater coverage (as ◇, ○ in figure 6.12). When the strip entry temperature is high (as □, △ in figure 6.12) the increase in annealing temperature has no effect upon the disordered crater coverage.

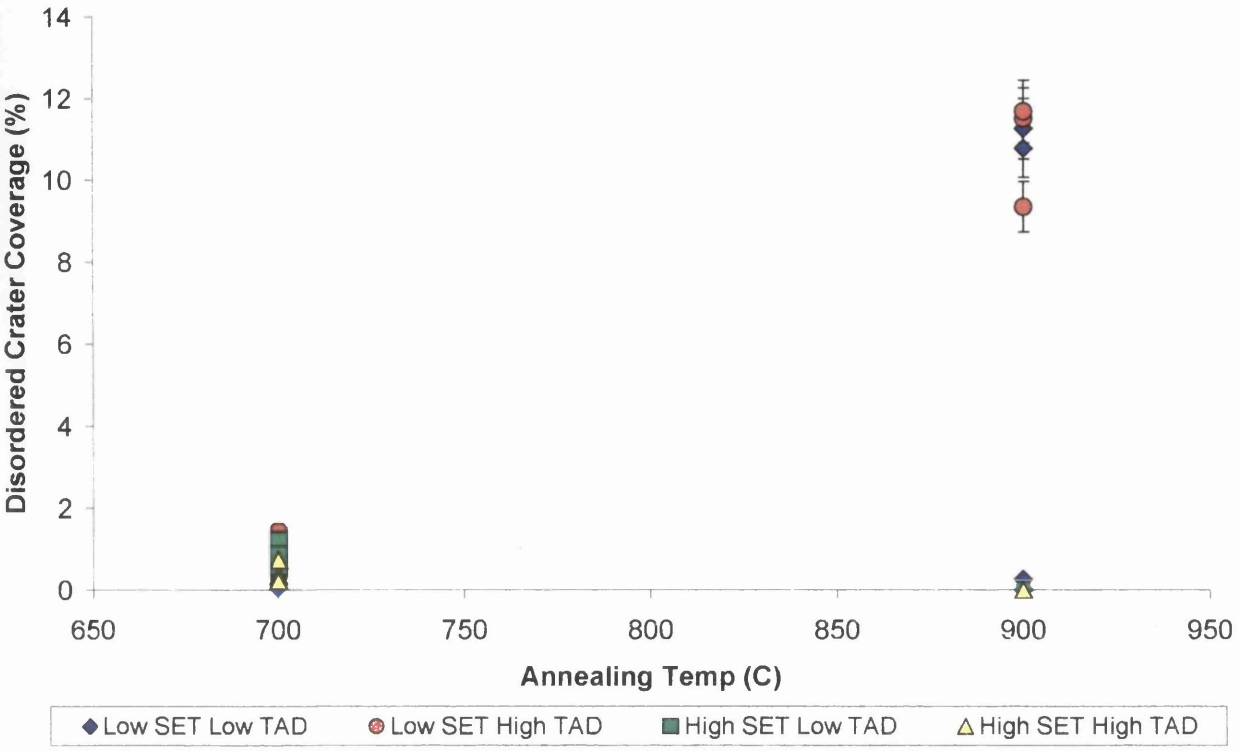

Figure 6.12. The effect of annealing temperature upon disordered crater coverage.

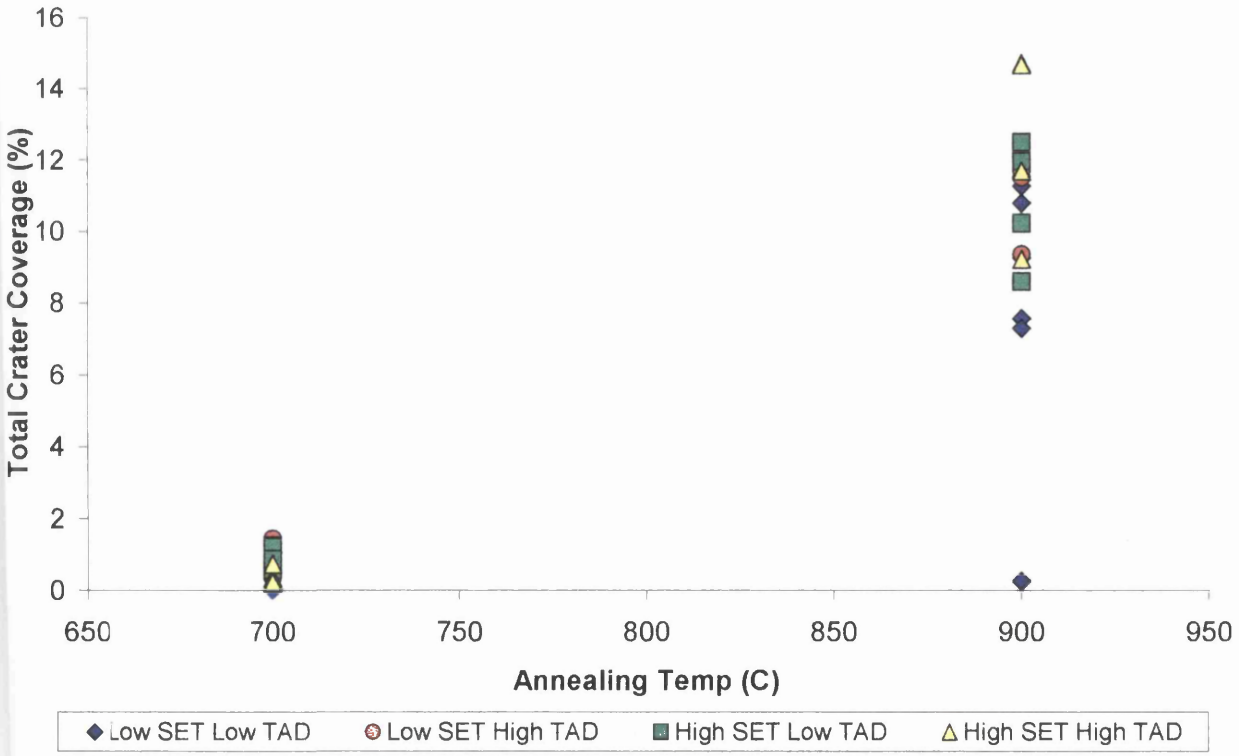

Figure 6.13. The effect of annealing temperature upon total crater coverage.

Figure 6.13 illustrates the influence of annealing temperature upon the total crater coverage. A strong positive relationship is defined whereby an increase in the annealing temperature from 700°C to 900°C produces an increase in the total crater coverage.

Temperature After Dipping (TAD)

Figure 6.14 illustrates the negligible effect that the temperature after dipping has upon the coverage of ordered crater within the galvanneal coating. The highest ordered crater coverage is experienced with samples processed with both a high annealing temperature and a high strip entry temperature (as □ in figure 6.14). All other processing conditions produced zero ordered crater coverage.

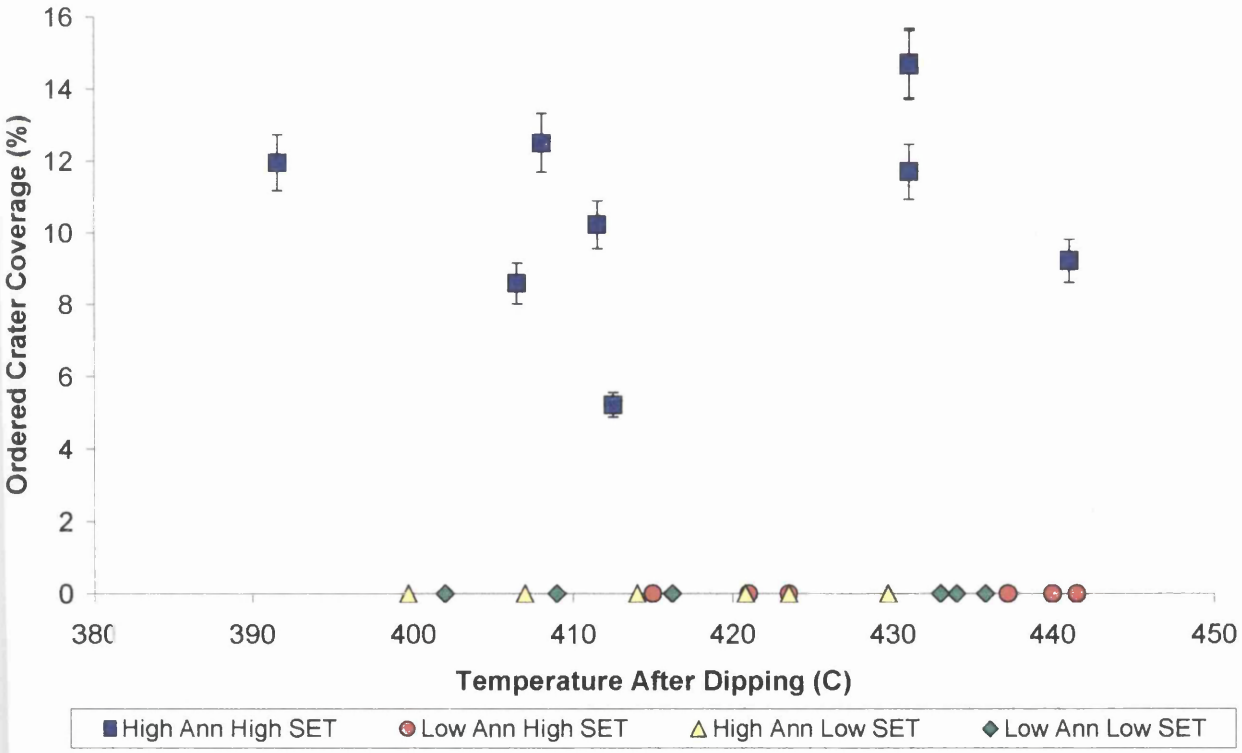

Figure 6.14. The effect of temperature after dipping upon ordered crater coverage.

Figure 6.15 illustrates the effect of temperature after dipping upon disordered crater coverage within the galvanneal coating. The highest disordered crater coverage occurs when a high annealing temperature is combined with a low strip entry

temperature (as △ in figure 6.15). All other conditions produce very low disordered crater coverage and the influence of temperature after dipping is seen to be negligible.

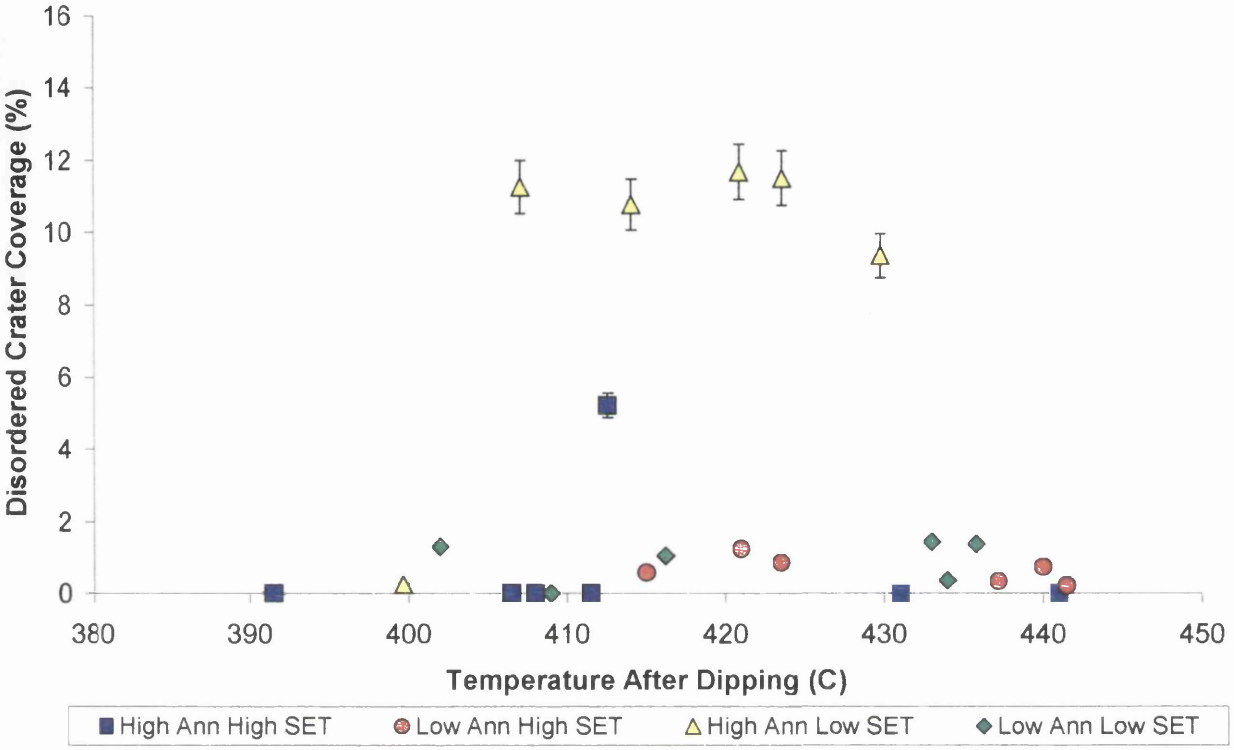

Figure 6.15. The effect of temperature after dipping upon disordered crater coverage.

Figure 6.16 shows the negligible effect of temperature after dipping upon the total crater coverage. The highest crater coverage occurs when a high annealing temperature is utilised (as □, △ in figure 6.16).

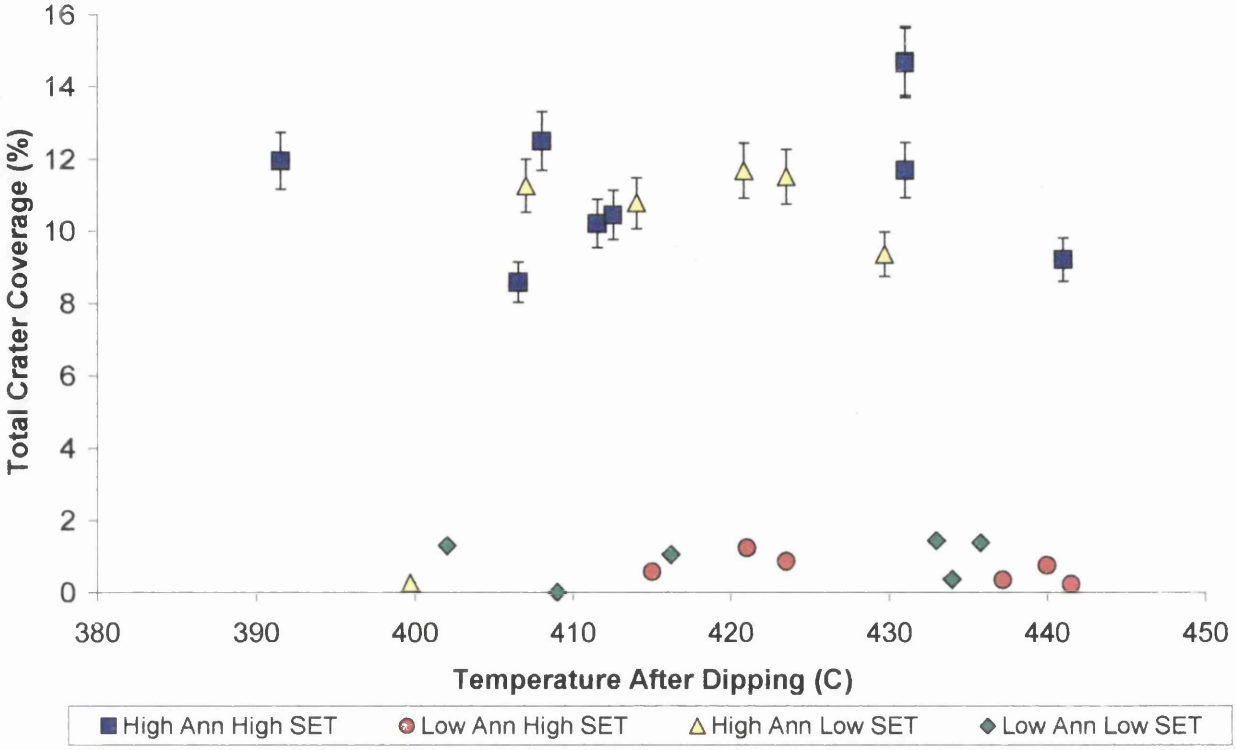

Figure 6.16. The effect of temperature after dipping upon total crater coverage.

Effective Aluminium Content

Figure 6.17 illustrates the influence that the effective aluminium content of the spelter has upon the coverage of ordered craters within the galvanneal coating. An increase in the effective aluminium content from 0.1wt% to 0.113wt% led to a decrease in the ordered crater coverage for those samples with a high annealing temperature (as ◇, △ in figure 6.17). Of these the biggest decrease was seen when a high annealing temperature was used in conjunction with a low strip entry temperature (as ◇ in figure 6.17).

When a low annealing temperature was utilised zero crater coverage was experienced at effective aluminium contents of both 0.1wt% and 0.113wt% (as ○ in figure 6.17).

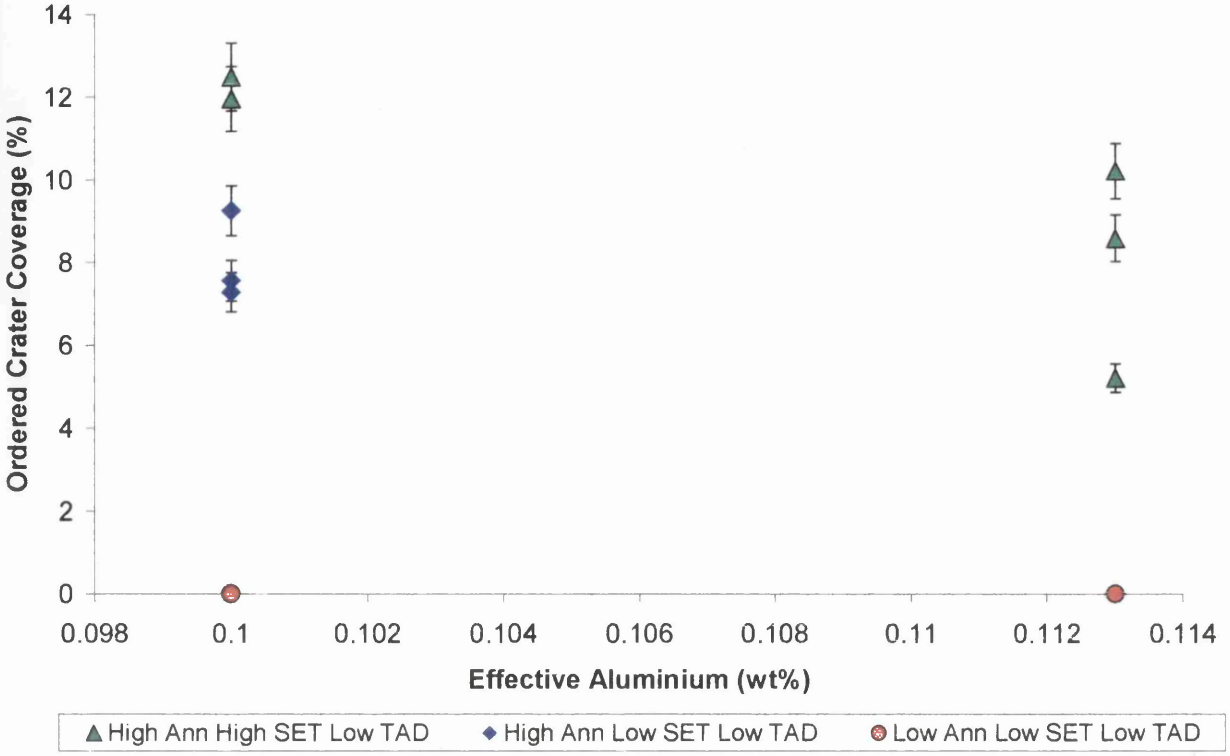

Figure 6.17. The influence of effective aluminium content upon ordered crater coverage.

The influence of effective aluminium content upon the formation of disordered craters within the galvanneal coating is shown in figure 6.18. Overall an increase in the effective aluminium content from 0.1wt% to 0.113wt% produces an increase in the disordered crater coverage. The greatest increase is seen when a high annealing temperature is used in conjunction with a low strip entry temperature (as ◇ in figure 6.18).

Figure 6.19 shows the influence of effective aluminium content upon the total crater coverage of the galvanneal coating. An increase in the effective aluminium content of the spelter has negligible effect upon the total crater coverage.

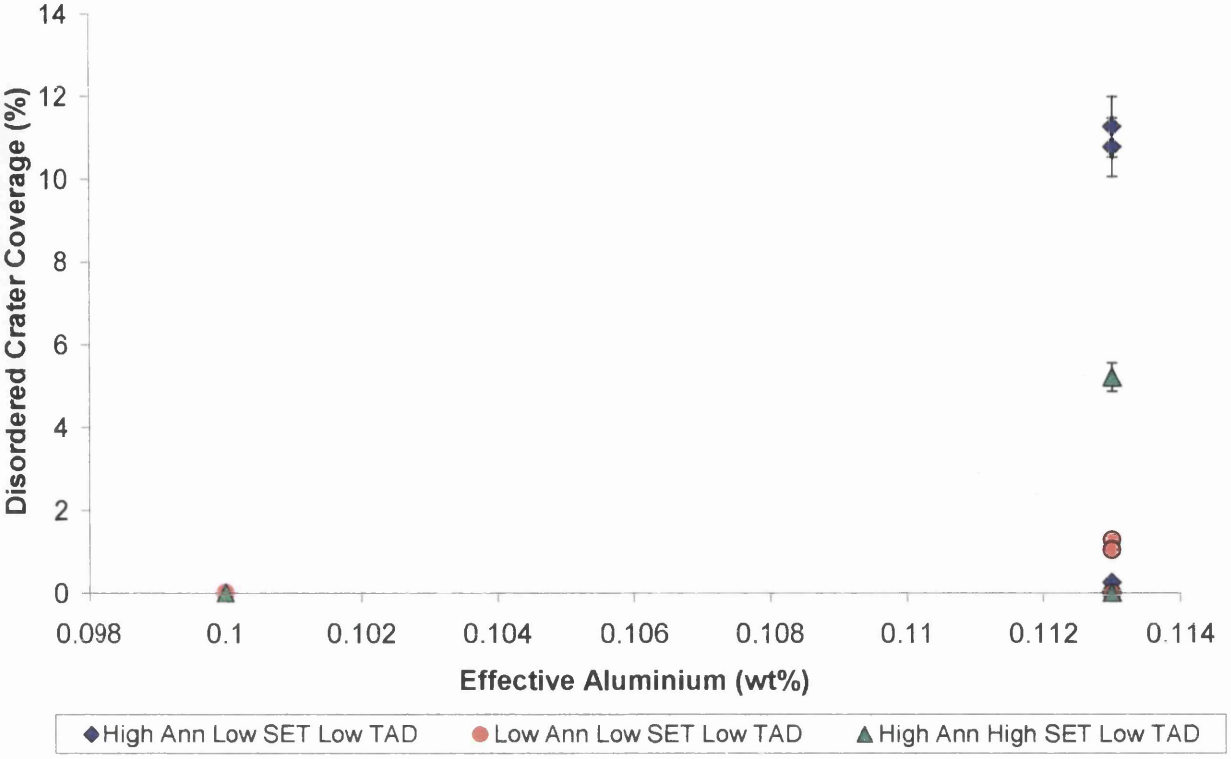

Figure 6.18. The influence of effective aluminium content upon disordered crater coverage.

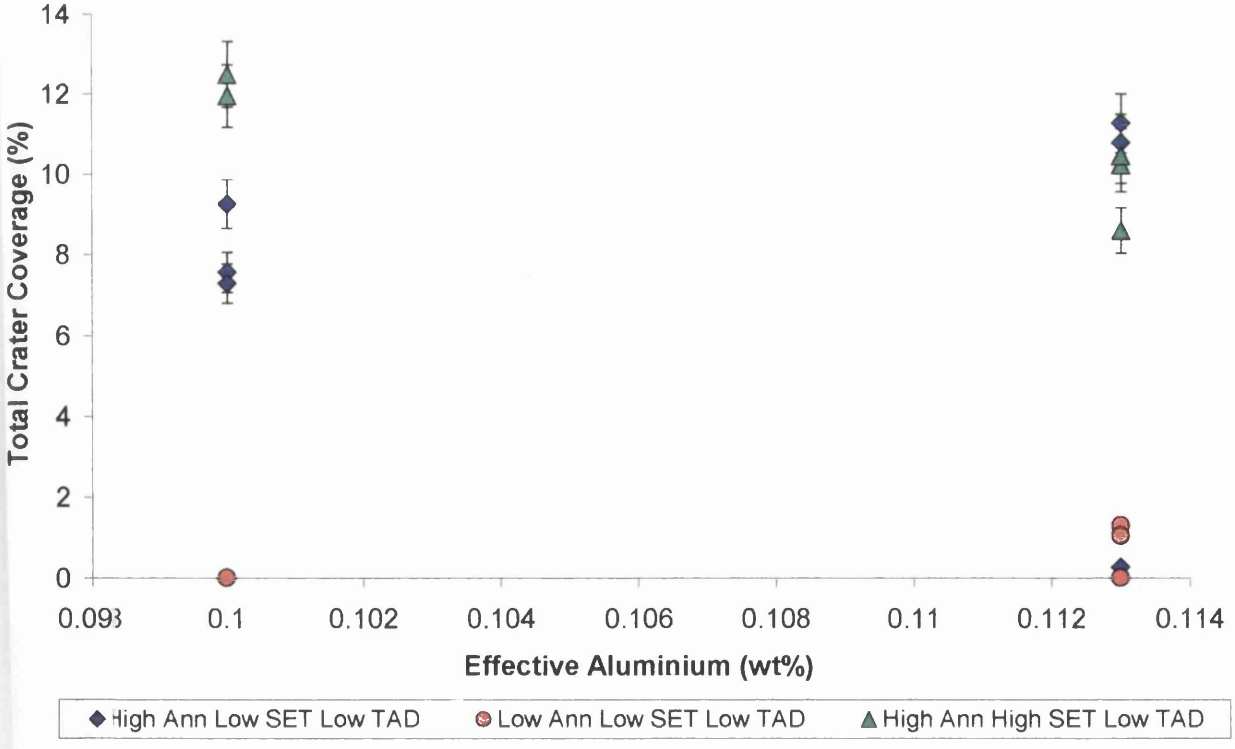

Figure 6.19. The influence of effective aluminium content upon total crater coverage.

6.2.4 Discussion

The effect of numerous process parameters upon the crater coverage within the galvanneal coating were analysed by this investigation. Each of these process parameters will be discussed in turn.

Annealing Temperature

Figures 6.5 and 6.13 show the effect of annealing temperature upon the overall crater coverage within the galvanneal coating. Over the range of 700°C to 900°C an increase in the annealing temperature leads to an increase in the overall crater coverage. An increase in the annealing temperature creates greater recrystallisation of the cold rolled microstructure. This in turn produces a greater proportion of {111} oriented grains upon which, as stated by Carless (2000), craters can nucleate.

In addition figures 6.11 and 6.12 show the effect of annealing temperature upon ordered and disordered craters. In both cases an increase in the annealing temperature from 700°C to 900°C shows an increase in the coverage. This illustrates the fact that both ordered and disordered craters nucleate upon {111} oriented grains.

Galvannealing Temperature

The effect of galvannealing temperature upon the coverage of craters within the galvanneal coating is shown in figure 6.7. A strong correlation is observed whereby an increase in the galvannealing temperature produces a decrease in the crater coverage. The reasoning behind this is clear when the iron-zinc equilibrium phase diagram, figure 2.9, is analysed. At the zinc rich end of the phase diagram a peritectic transformation is observed at 530°C. Above this temperature the ξ phase is no longer permissible under equilibrium conditions. Furthermore, due to the curve of the Liquid/(L+ζ) phase boundary and for a given iron content, the closer the galvannealing temperature gets to the peritectic temperature the less abundant the ζ phase becomes.

The exact effect that this will have upon the craters within the coating is unclear. If the ordered ξ crystals at the base of the crater form within the bath the higher galvannealing temperature may cause them to become unstable and remelt. If however the ordered ξ crystals form during the galvannealing process the higher temperature may hinder their formation. In either case a lower crater coverage, as shown in figure 6.7, would occur at a higher galvannealing temperature.

Effective Aluminium

Figures 6.17, 6.18 and 6.19 illustrate the relationship between the effective aluminium content of the spelter and the crater coverage within the galvanneal coating. When a high annealing temperature is used analysis of the ordered craters shows a negative correlation between the effective aluminium and the crater coverage. When a low annealing temperature is used zero ordered crater coverage is observed at both effective aluminium levels. In addition the greatest effect is observed when a high effective aluminium is combined with a low strip entry temperature. However when the disordered crater coverage is analysed a positive relationship is observed between the effective aluminium and the crater coverage. Combining both relationships it can be seen that the overall crater coverage is unaffected by the change in effective aluminium.

This change in morphology as a result of the change in effective aluminium is explained by the fact that when the effective aluminium level is higher than 0.1wt% the δ phase becomes the thermodynamically favoured phase (Tang, 1998). The random δ phase therefore nucleates preferentially upon the {111} oriented grains instead of the ordered ξ crystals. In addition, the increase in effective aluminium content would produce a thicker inhibition layer that would loose its orientation relationship with the underlying substrate (Guttmann *et al*, 1995). This would also promote the nucleation of the random δ phase, as the ordered ξ phase prefers to nucleate epitaxially. Furthermore because the total coverage is unaffected by the effective aluminium it can also be stated that over the range of concentrations used the effective aluminium does not affect the availability of sites upon which craters can form.

Strip Entry Temperature

Figures 6.6, 6.8, 6.9 and 6.10 show the relationship between the strip entry temperature and the crater coverage within the galvanneal coating. Figure 6.8 shows the positive correlation between the strip entry temperature and the ordered craters within the galvanneal coating. However, figure 6.9 shows the negative correlation between the strip entry temperature and the disordered craters. Combining both the ordered and the disordered crater coverage in figure 6.10 it can be seen that zero correlation exists between the overall crater coverage and the strip entry temperature.

This illustrates that the strip entry temperature affects only the morphology of the craters and not the overall coverage. Furthermore, it also suggests that the initial formation of craters happens during the very first moments of dipping where the strip entry temperature has the greatest influence. The reasoning behind this variation in morphology with strip entry temperature is that when the temperature is high the iron atoms within the strip are more active and thus more able to escape from the strip, equation 2.4. This results in an increase in the iron content next to the strip and an overall reduction in the local effective aluminium. This makes the ξ phase the thermodynamically stable phase thus resulting in ordered craters. At a lower strip entry temperature the iron dissolution is less, the local effective aluminium higher and the δ phase the thermodynamically stable phase. In addition because the total coverage is unaffected by the strip entry temperature it can also be stated that over the range of temperatures used the strip entry temperature does not affect the number of sites upon which craters can form.

Bath Temperature

The zero correlation between the bath temperature and the crater coverage is shown in figure 6.4 and helps to further support the notion that the initial formation of the craters occurs during the first few moments of dipping. Due to the high thermal conductivity of steel and the density of the zinc bath the steel strip will rapidly attain the same temperature as the bath. If crater formation was occurring throughout the

dipping process a correlation between the bath temperature and the crater coverage would be expected.

Temperature After Dipping

Figures 6.14, 6.15 and 6.16 illustrate the zero correlation observed between the temperature after dipping and the crater coverage within the galvanneal coating. Zero correlation is observed for the ordered craters, disordered craters and the total coverage. This lack of correlation shows that the formation and growth of the craters within the galvanneal coating does not occur after the strip has left the spelter.

6.2.5 Summary

This investigation has shown that the main process parameters with the greatest influence upon overall crater formation are the annealing and galvannealing temperature. An increase in the annealing temperature leads to an increase in the overall crater coverage whereas an increase in the galvannealing temperature leads to a decrease in overall crater coverage. Alteration of the crater morphology is achieved by modifying the strip entry temperature or the effective aluminium content of the spelter. Increasing the strip entry temperature leads to a more ordered morphology whereas increasing the effective aluminium creates a disordered morphology. No effect on crater coverage or morphology was observed by changing the temperature after dipping. Table 6.5 summarises the overall effects of the different process parameters upon craters within the galvanneal coating.

Table 6.5. Summary of process parameter effects.

Increasing Process Parameter	**Ordered Craters**	**Disordered Craters**	**Overall Crater Coverage**
Annealing Temperature	↑	↑	↑
Galvannealing Temperature	↓	↓	↓
Strip Entry Temperature	↑	↓	↔
Effective Aluminium	↓	↑	↔
Spelter Temperature	↔	↔	↔
Temperature After Dipping	↔	↔	↔

(↑ = Increase, ↓ = Decrease, ↔ = No Change)

6.3 EXPERIMENTAL INVESTIGATION THREE

Investigation into the characteristics, formation and development of craters within the galvanneal coating produced on the Rhesca hot dip simulator.

As stated in section 5.5 craters are not observed within the galvanised coating but develop during the galvannealing process. This investigation was designed to explain how craters form during the change from a galvanised to a galvannealed coating.

6.3.1 Size Distribution of Craters

The size distribution of over 4,000 craters is shown in figure 6.20. The mode of the distribution is the 33 to 47 square microns and, if the crater was circular, equates to a diameter of approximately 7μm. The largest crater measured, but which does not appear in figure 6.20, was 2949 square microns that, if the crater was circular, equates to a diameter of approximately 30μm.

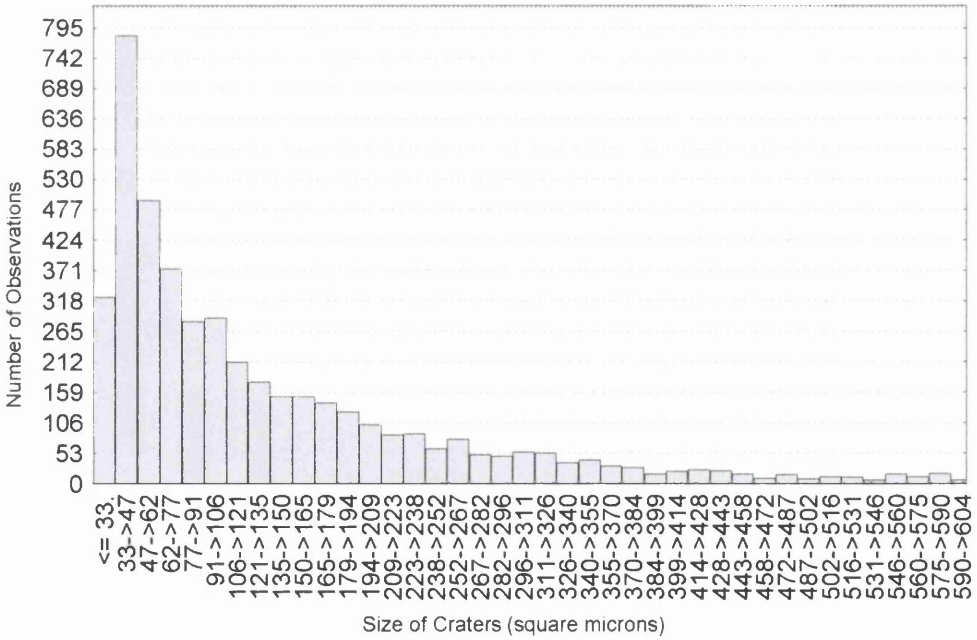

Figure 6.20. Size distribution of craters within the galvanneal coating.

6.3.2 Formation of Ordered Craters

The formation of ordered craters as the coating develops from a galvanised to a galvannealed coating is shown in figure 6.21. The initial formation of the galvanneal coating is shown in figure 6.21a where the emergence of ζ crystals at the surface is observed. Figure 6.21b shows the initial formation of the lip of the crater as the galvannealing process continues. This lip becomes more pronounced and ordered ζ crystals are observed at the base of the crater after further galvannealing, figures 6.21c and 6.21d. In figure 6.21e the normal galvanneal coating is almost formed with a few columnar ζ crystals at the surface of the coating. The edge of the crater is truly defined and the ordered ζ crystals are observed at its base. Finally, figure 6.21f shows the zero-ζ galvannealed coating with a predominantly δ structure at the surface. The craters are easily seen within the coating and consist of ordered craters at their base.

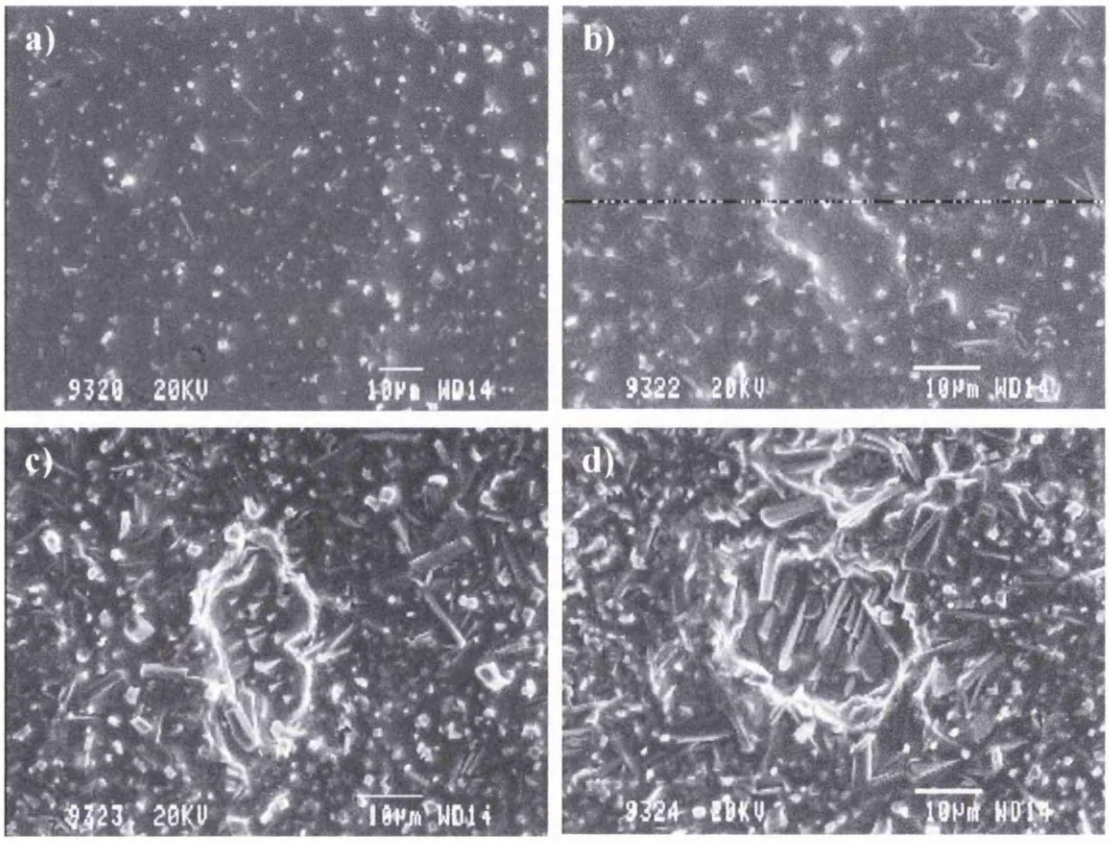

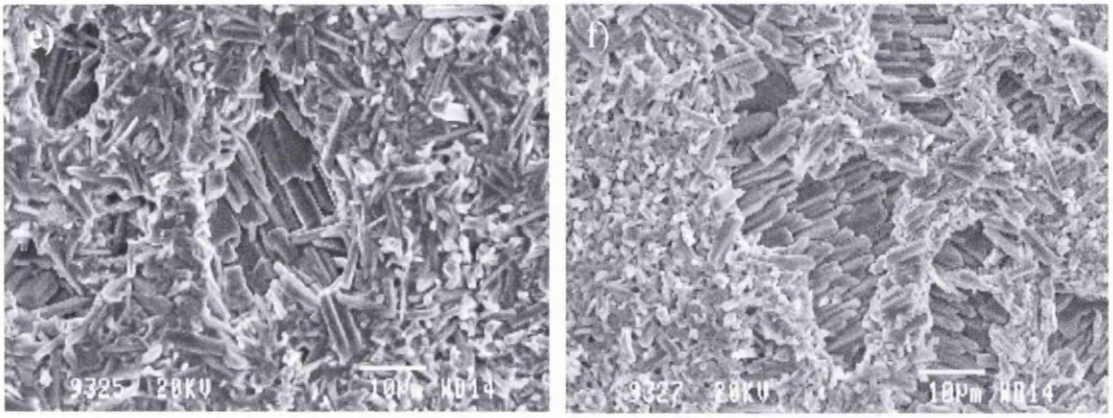

Figure 6.21. SEM images of the formation of ordered craters.

6.3.3 Formation of Disordered Craters

Figures 6.22 shows the formation of disordered craters as the coating develops from a galvanised coating to a galvannealed coating. Figure 6.22a shows the initial stages of the change from the galvanised to the galvannealed coating. Within the figure can be seen the emergence of ζ crystals on the surface of the coating along with the initial lip and dip of the crater.

In figure 6.22b the lip of the crater has become more defined and the emergence of ζ crystals more pronounced. The size of the emerging ζ crystals within the crater remains unchanged even though those crystals within the normal coating are growing.

As the galvannealing process continues, figure 6.22c, the ξ crystals within the normal coating continue to grow and the first presence of the δ phase is observed. All of the free zinc at the base of the crater has gone and been replaced with a microstructure whose size is comparable to that seen at the base of the crater in figure 6.22b. The edge of the crater is now completely defined.

In figure 6.22d the normal coating has now almost completely transformed to the δ phase. The microstructure at the base of the crater has changed very little during the continuation of the galvannealing process and contains a mixture of both ζ and δ.

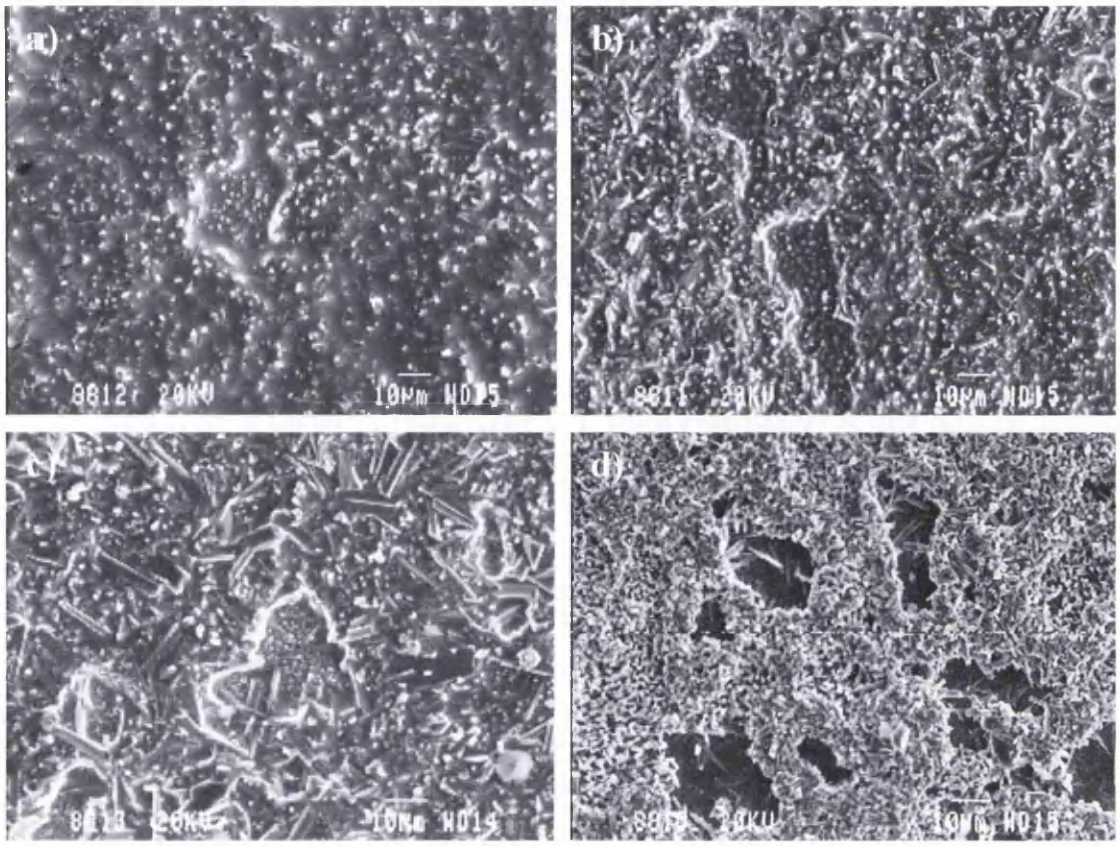

Figure 6.22. SEM images of the formation of disordered craters.

In addition, figure 6.23 shows the variation of the iron content at the different stages of galvannealing for both the surface of the normal coating and that of the disordered crater. Initially we can see that in stages one and two the iron content of the crater is slightly higher than that of the normal coating. During stages three and four the iron content of the crater rapidly increases up to nearly 43%. In contrast the iron content of the coating only gradually increases up to approximately 6%.

Elemental mapping of both ordered and disordered craters is shown in figure 6.24. A high iron content is observed within the disordered crater whereas the ordered crater has an almost identical coating constitution to the normal coating. Zero correlation is observed between the aluminium content and the location of the craters.

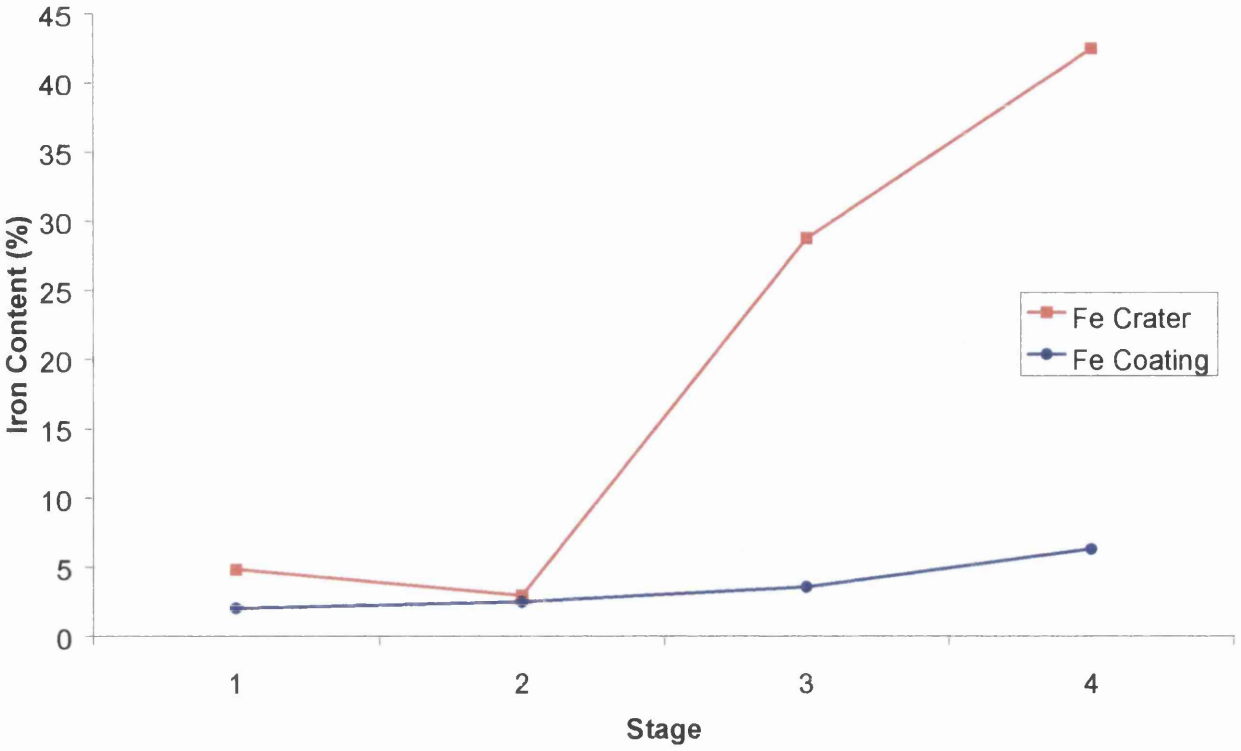

Figure 6.23. Variation of the iron content at the coating and disordered crater surface.

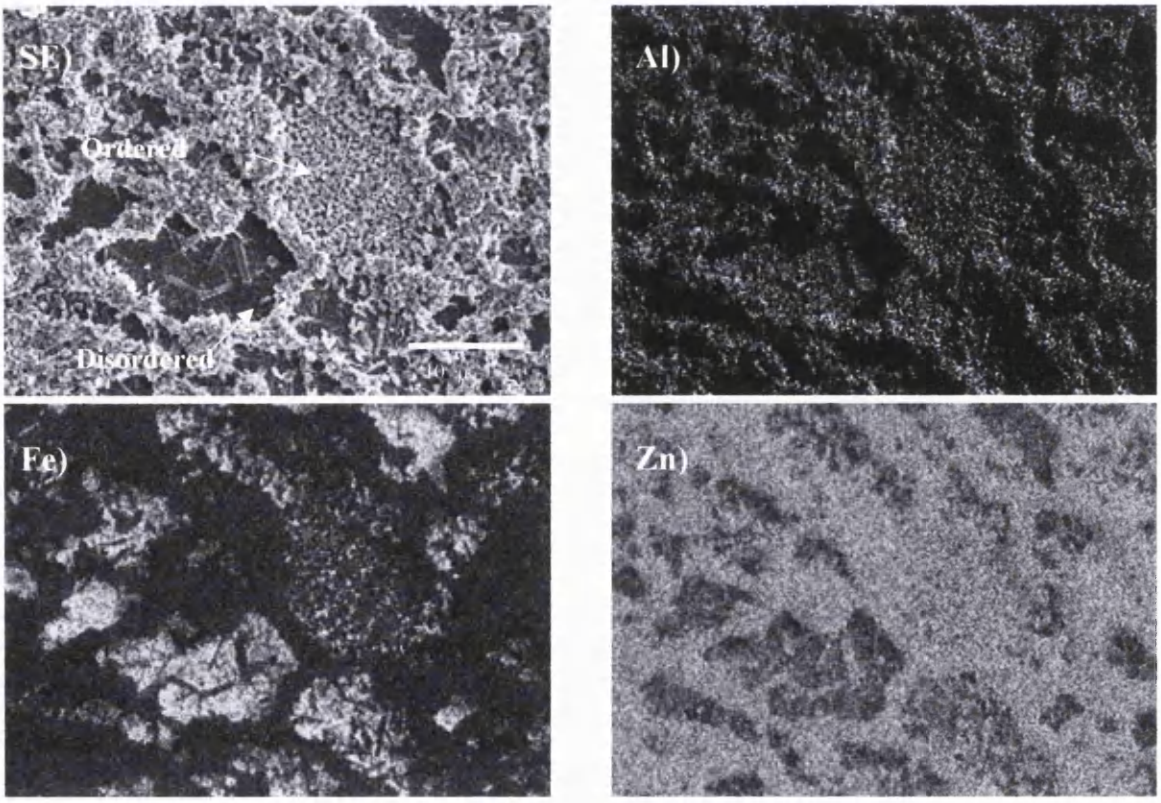

Figure 6.24. Elemental mapping of ordered and disordered craters.

6.3.4 Underlying Substrate

Figures 6.25a and 6.25b show the optical images of the TiNb IF steel substrate annealed at 700°C and 900°C respectively. When annealed at 700°C, figure 6.25a, the deformed grains from the cold rolling process are still evident within the microstructure. However, when annealed at 900°C, figure 6.25b, no deformed grains are observed and instead the structure consists of recrystallised equiaxed grains.

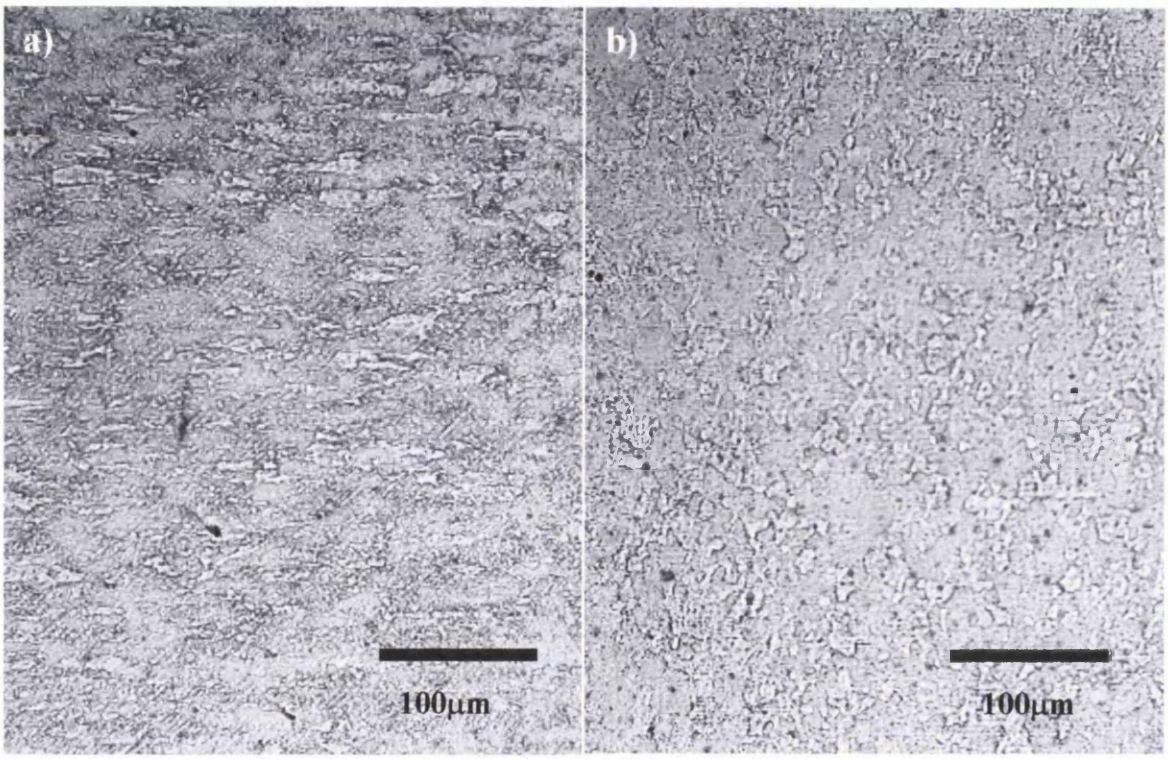

Figure 6.25. Optical images of the substrate annealed at a) 700°C and b) 900°C.

Further work was also carried out on the annealed substrates using Electron BackScatter Diffraction (EBSD). Figure 6.26 shows the inverse pole figures for the normal direction obtained for the substrates annealed at 700°C and 900°C. A higher annealing temperature of 900°C produces a grain texture containing a greater proportion of grains with {111} oriented in the plane of the sheet.

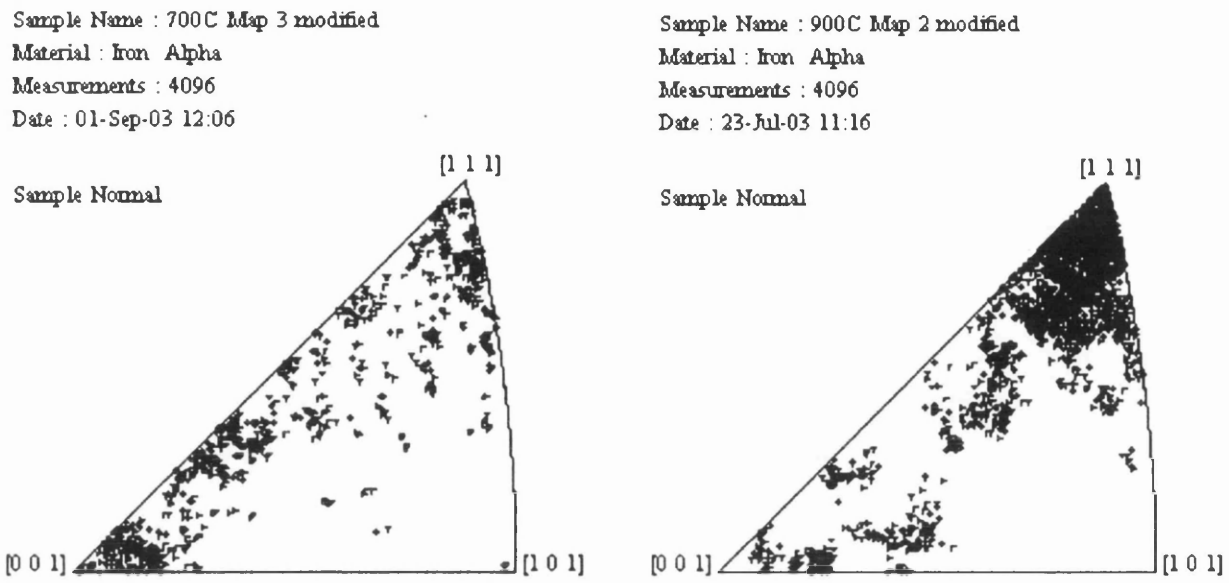

Figure 6.26. EBSD inverse pole figures for substrates annealed at 700°C and 900°C

By removing the coating, as described in section 5.5, it has been possible to correlate the association between the underlying substrate and craters within the galvanneal coating. Figures 6.27a to figure 6.27c each show the galvanneal coating together with the substrate that is directly beneath. In all of the figures direct matching between the edges of the crater and grain boundaries within the underlying substrate can be seen. Within these grain boundaries a lighter plateau is observed which matches the areas covered by the ordered crystals.

However, by comparing figure 6.27 with the optical image in figure 6.25b it can be clearly seen that the SEM image does not reveal all of the grain boundaries. For identical annealing conditions the average grain size in figure 6.25b is approximately 10μm whereas in figure 6.27 the 'grain' size is approximately 50μm. Closer examination between grains two and three in figure 6.27 shows the variation of crystal orientation over what initially appears to be a single 'grain'. Within this single 'grain' can be seen the very faint outline of a grain boundary corresponding to the same position at which the variation in crystal structure occurs.

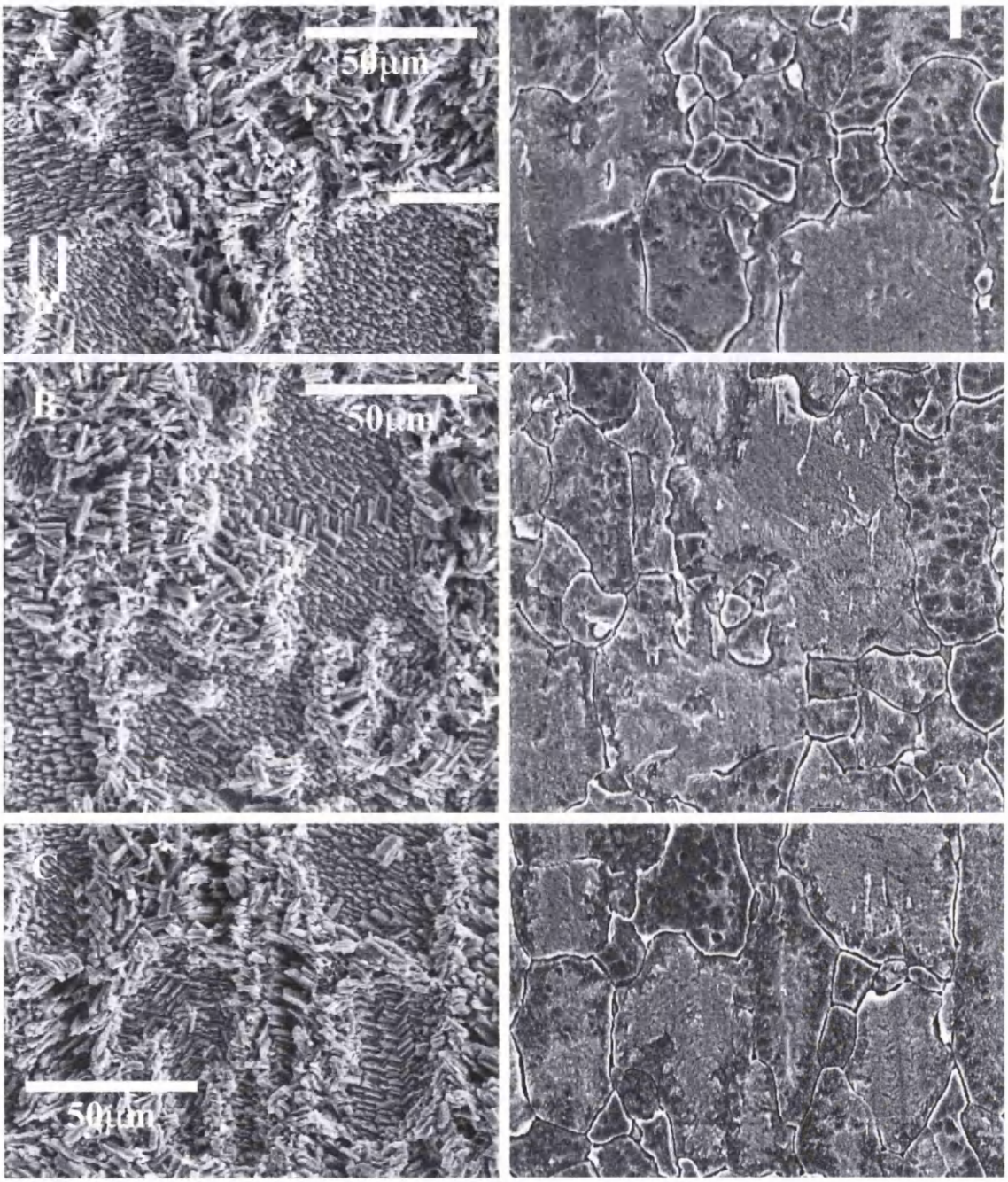

Figure 6.27. SEM images of the galvanneal coating and underlying substrate.

6.3.5 Discussion

This investigation, coupled with investigation two, was carried out to determine how craters form and then develop during the galvannealing process. Both ordered and disordered craters were investigated together with the influence of the underlying substrate.

Formation and Development of Ordered Galvanneal Craters

As detailed by Carless (2001), Inagaki (1995) and Guttmann (1995) the formation of craters takes place upon {111} oriented grains. This has been confirmed by the results from investigation two that show an increase in the numbers of craters as a result of an increase in annealing temperature. In addition, figure 6.27 shows that craters are not confined to just a single {111} oriented grain and can actually form over several {111} oriented grains so long as they are contiguous. Furthermore, if no {111} oriented grains are available then zero crater coverage will be experienced regardless of what any other process parameter is set to.

The effect of strip entry temperature and effective aluminium on the crater coverage illustrates the notion that the ordered ζ crystals form during the initial stages of the dipping process. Upon entering the bath the zinc near the strip becomes super-saturated with iron. From this super-saturation both the inhibition layer and iron-zinc intermetallics can form. Where the inhibition layer nucleates upon a {111} oriented grain an orientation relationship develops between the grain and the inhibition layer (Guttmann *et al.*, 1995). Furthermore where a {111} grain exists the ordered ζ crystals are able to nucleate on top of the oriented inhibition layer. Where a suitable nucleation site does not exist or where concentration and thermal variations prevent nucleation the standard initial layer forms. This consists of an Fe_2Al_5 inhibition layer and possibly random ζ or δ intermetallics. Figure 6.28 shows a schematic diagram of the initial layer formation.

The lack of influence of both the bath temperature and the temperature after dipping upon the crater coverage shows that after the initial nucleation very little happens until the strip reaches the galvannealing furnace.

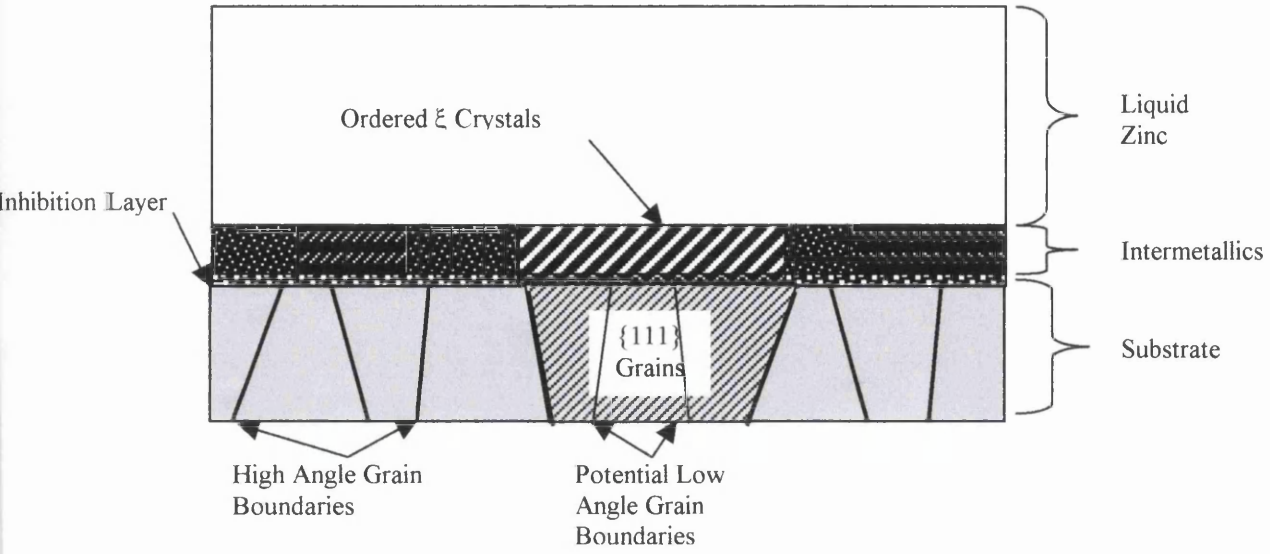

Figure 6.28. Schematic diagram of the initial layer formation.

Upon reaching the furnace the galvannealing process begins. Where the ordered ζ crystals have not formed the liquid zinc penetrates the inhibition layer and reacts with the iron diffusing from the substrate. This results in the formation of the iron-zinc intermetallics ζ, δ and Γ. Figure 6.27 shows that the grain boundaries between {111} and non-{111} are high angle boundaries. These high angle grain boundaries provide rapid transport routes for iron out of and zinc into the substrate. The rapid movement of iron out of the substrate leads to the formation of outburst structures and, as shown in figure 6.21b, results in the initial lip of the crater.

Where ordered ζ crystals (>94wt% Zn) have formed upon {111} oriented grains zinc penetration into the inhibition layer is restricted and the inhibition layer remains intact. Furthermore, the persistence of the inhibition layer prevents the diffusion of iron atoms into the ordered ζ crystals, restricting their growth and maintaining the zinc above them as liquid. If however a higher galvannealing temperature is used the ordered ζ crystals become unstable and the inhibition layer breaks down. This results in the development of a normal galvanneal coating and, as shown in figure 6.7, a reduction in the crater coverage. Figure 6.29 illustrates a schematic diagram of the initial stages of galvannealing.

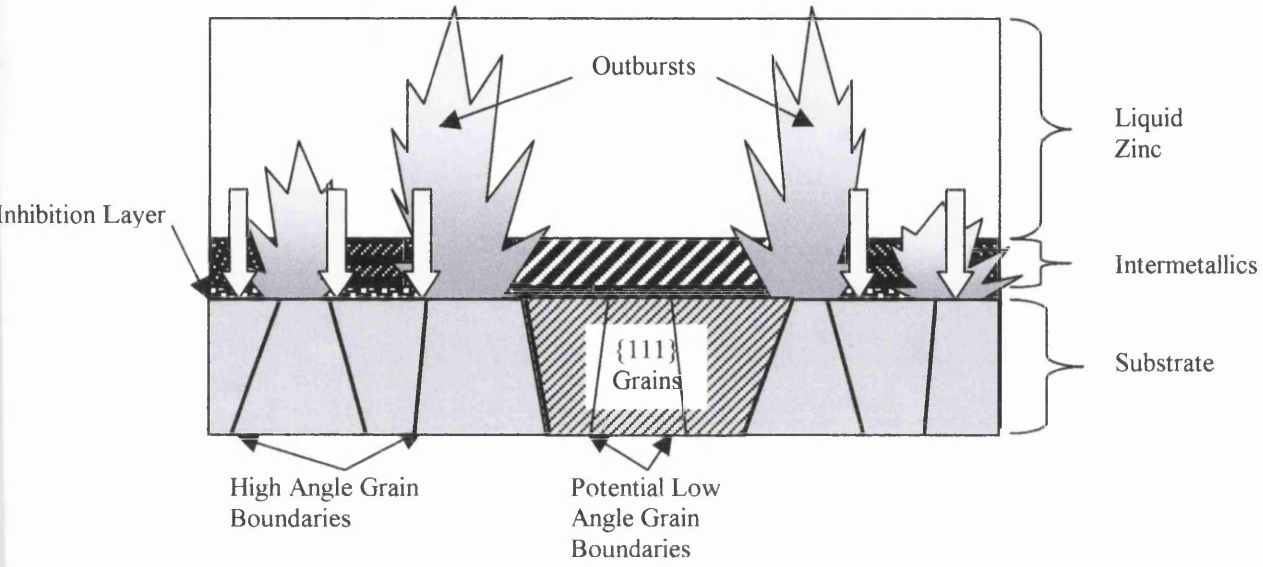

Figure 6.29. Schematic diagram of the initial stages of galvannealing.

Where the ordered ζ crystals have not formed the normal coating will continue to develop during the galvannealing process. Where the ordered ζ crystals have formed the zinc above them remains liquid and is therefore subsequently drawn into the adjacent galvanneal coating, figure 6.21. In addition the persistence of the inhibition layer beneath the ordered ζ crystals limits their growth by restricting the flow of iron into them. Figure 6.30 shows a schematic diagram of the coating and crater development.

Intermetallics

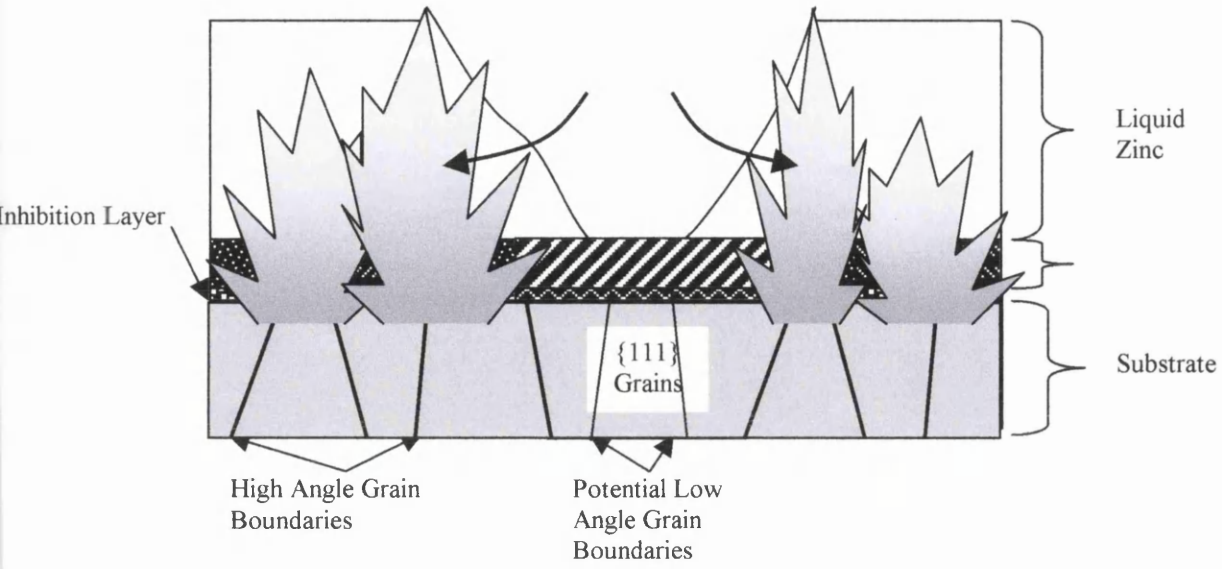

Figure 6.30. Schematic diagram of the coating and crater development.

By the end of the galvannealing process the normal coating consists of the δ phase and a continuous layer of the Γ phase at the substrate. Where craters have formed the liquid zinc has been drawn into the adjacent coating and the ordered ζ crystals at the base are clearly visible, figure 6.21. In addition because no diffusion into the substrate has occurred a plateau of steel now existed below the ordered ζ crystals. Figure 6.31 shows a schematic diagram of the fully developed coating and crater.

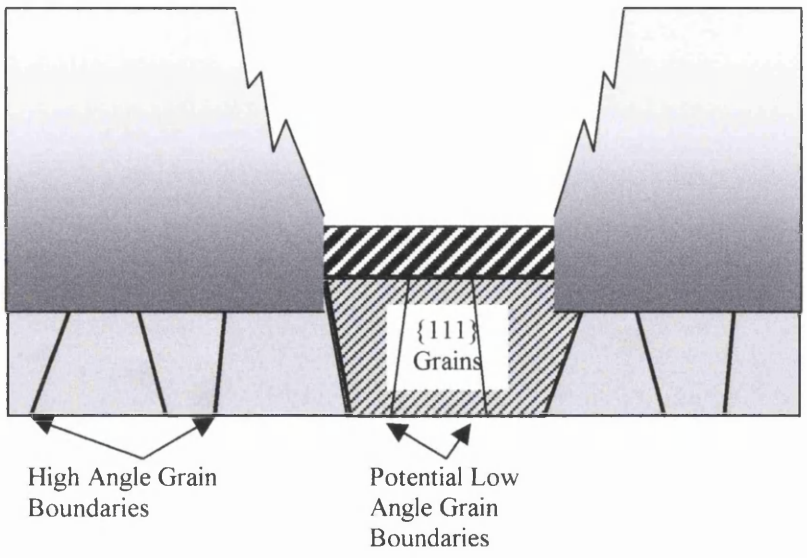

Figure 6.31. Schematic diagram of the fully developed coating and crater.

As with ordered craters and illustrated by figure 6.12, disordered craters also form upon {111} oriented grains. The influence of strip entry temperature and effective aluminium shows that the initial nucleation of the disordered craters occurs during the first few moments of dipping. Either the lower strip entry temperature or the higher effective aluminium content will result in the degree of iron super-saturation near the surface of the strip being lower. Any nucleation of iron-zinc intermetallics upon the {111} oriented grains will therefore be considerably thinner and of a different morphology. Even so, the process by which the disordered craters form is identical to that of the ordered craters. The only difference is that during the galvannealing process the base of the crater increases in iron content, figures 6.23 and 6.24. This increase in iron content is not observed within the ζ crystals at the base of an ordered crater. This increase in iron content is partly attributed to the morphology of the crystals at the base of the disordered structure. The δ phase exists over a much larger range of iron contents compared to the ζ phase. As a result, iron can more easily diffuse into the base of the crater without the need for a change in morphology. In addition, as the liquid zinc is drawn into the surrounding coating any measurement of the base of the crater may also start to include the underlying substrate thus leading to a further increase in the iron content.

6.3.6 Summary

This investigation has revealed how craters form as the coating develops from a galvanised coating to a galvannealed coating. It has shown that during the galvannealing process the zinc above the crater moves into the surrounding coating revealing either the ordered or disordered crystals at the base. It has also been shown how a higher annealing temperature modifies the crystallographic structure of the underlying substrate to create more nucleation sites upon which the craters can form. In addition the investigation has shown how craters form within the confines of high angle grain boundaries and yet are able to form over low angle grain boundaries.

6.4 EXPERIMENTAL INVESTIGATION FOUR

Investigation into the effects of craters upon the coating failure mechanism of the galvanneal coating produced on the Rhesca hot dip simulator.

As stated in section 5.6 it has been suggested that the presence of craters within the galvanneal coating may help to reduce the amount of powdering experienced during press forming operations. The following experimental investigation was designed to determine the influence that craters may have upon the galvanneal coating.

6.4.1 Powdering and Flaking Analysis

In order to ensure that any variations in powdering were due solely to the presence of craters and not a variation in coating weight or iron content a coating analysis using ICP was carried out. Figures 6.32 and 6.33 illustrate the variation of powdering and flaking over the range of coating iron contents produced in the investigation.

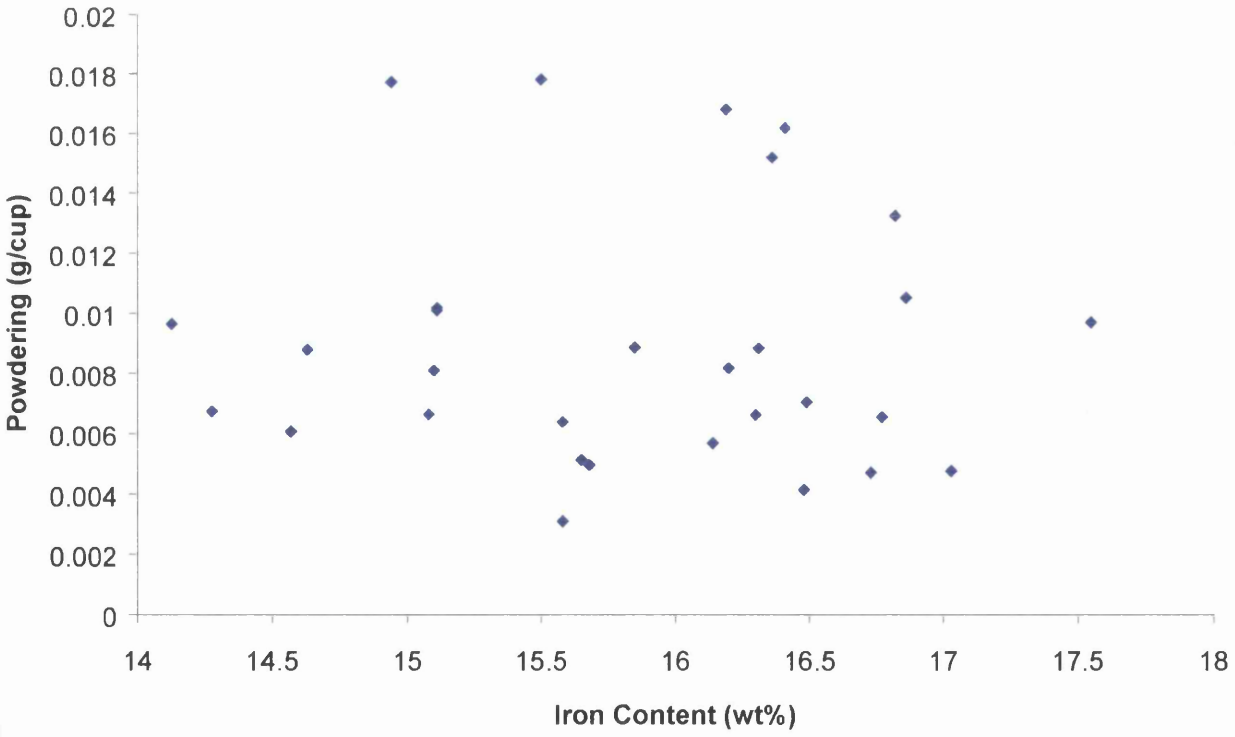

Figure 6.32. The effect of coating iron content on powdering.

Figure 6.32 shows the variation of powdering with iron content. Over the range of iron contents examined zero correlation was observed between the amount of powdering that occurs and the iron content of the coating.

Figure 6.33 shows the variation of flaking with iron content. Over the range of iron contents examined zero correlation was observed between the amount of flaking that occurs and the iron content of the coating. Furthermore, by comparing figures 6.32 and 6.33 it is clear to see that the application of the 3M scotch tape leads to a greater degree of coating loss.

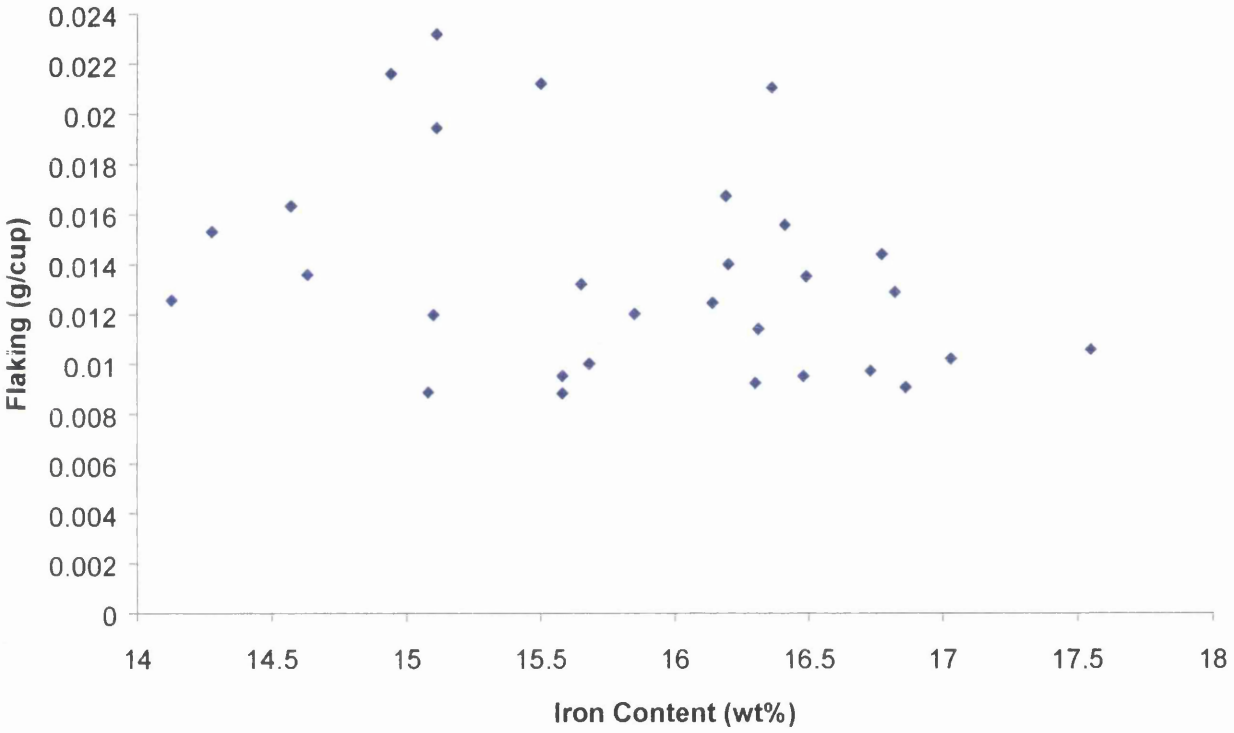

Figure 6.33. The effect of coating iron content on flaking.

The variation of coating loss with coating weight is shown in figures 6.34 and 6.35. Figure 6.34 illustrates the effect of coating weight on the powdering properties of the coating. A positive relationship is observed whereby an increase in the coating weight leads to an increase in the amount of powdering.

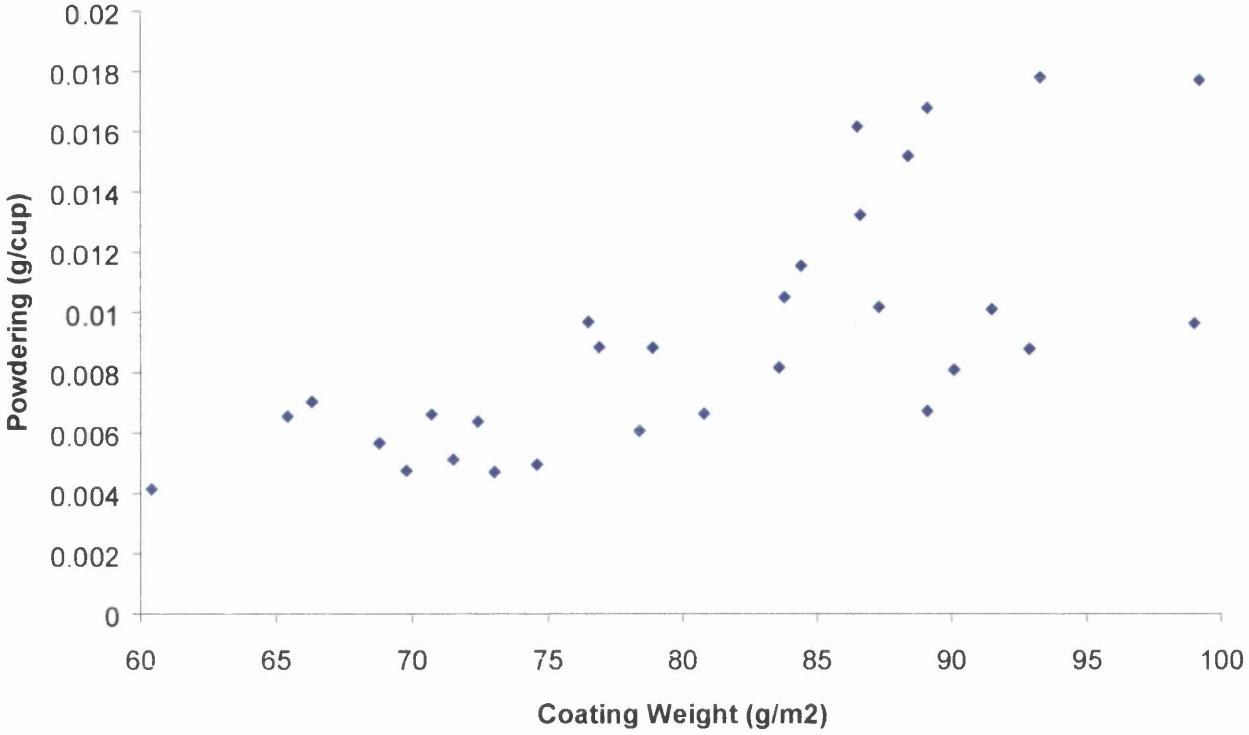

Figure 6.34. The effect of coating weight upon powdering.

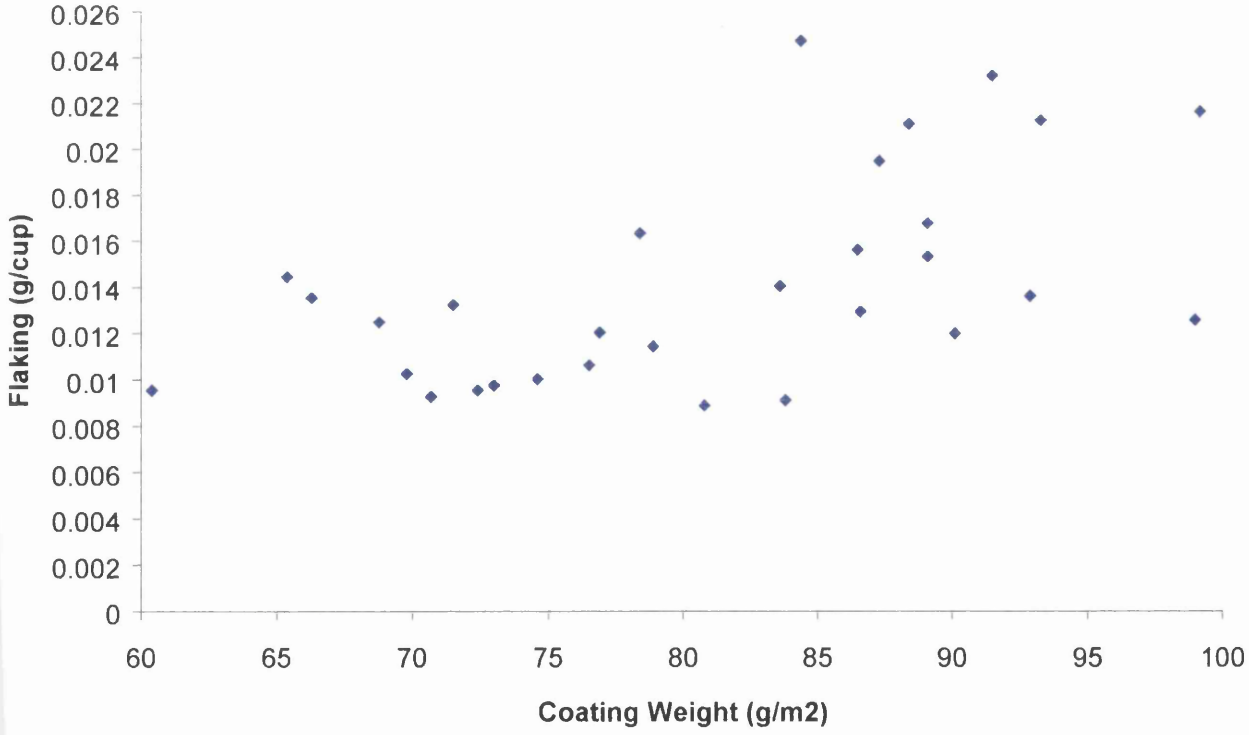

Figure 6.35. The effect of coating weight upon flaking.

Figure 6.35 shows the samples that have had the 3M scotch tape applied to the outer surface of the cup. Over the range of coating weights investigated a positive correlation is observed between the coating weight and the amount of flaking.

Incorporating the coating weight with the amount of coating failure it is possible to calculate the percentage of coating that has failed during the cup forming operation. The following equation was utilised to calculate the percentage powdering that had occurred for each of the samples.

$$\%loss = \frac{CL}{(AoD * CW)} * 100 \qquad (6.1)$$

where: CL is the coating loss in grams per cup

AoD is the Area of Disc = 1.8835×10^{-3} m^2

CW is the coating weight in grams per metre squared

A similar equation was utilised for the amount of flaking that had occurred during the press forming operation. The only difference was that the coating weight of the sample was reduced by the amount of powdering that had occurred. It should also be noted that the area of the disc has been reduced to incorporate the fact that all of the coating loss occurs at only the walls of the cup.

Figure 6.36 shows the variation of powdering when just the crater coverage is included. The amount of crater coverage varied from 0% to 14.7% and the percentage of coating loss varied from 3.4% to 10.5%. The distribution shows an initial decrease in the amount of powdering to about four percent coating loss at around six percent coverage. The distribution then increases up to about five percent coating loss at around twelve percent coverage before levelling out.

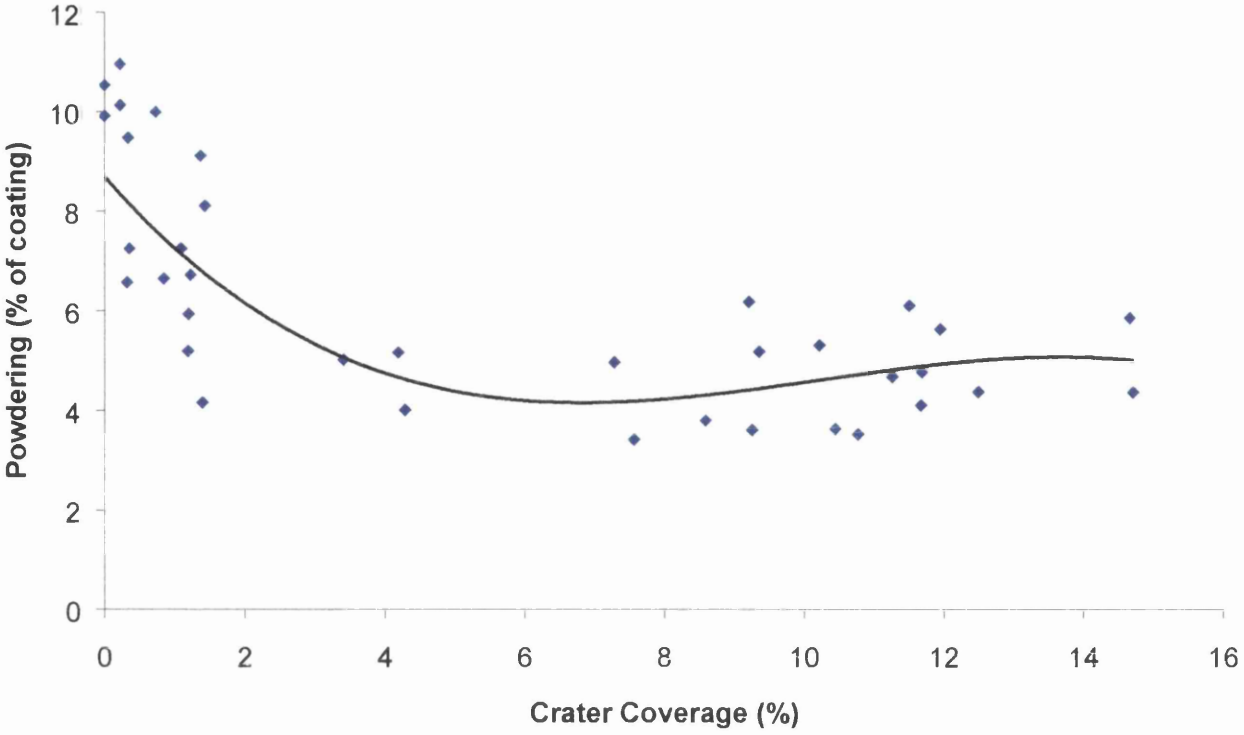

Figure 6.36. Variation of powdering with just crater coverage.

However, if the annealing temperature is included, figure 6.37, it can be seen that it is actually the increased annealing temperature that has resulted in the decrease in powdering rather than the presence of the craters within the coating. At the lower crater coverage it can be seen that the 900°C annealed substrate produces a lower coating loss than the 700°C annealed substrate. In addition, at the higher crater coverage with the 900°C annealing temperature it can be seen that from approximately 7% to 15% the amount of powdering does not vary as the crater coverage increases.

The variation of flaking with crater coverage and annealing temperature is shown in figure 6.38. It can be seen that there is zero correlation between the amount of flaking that has occurred and the crater coverage. Furthermore, if the samples annealed at 900°C are analysed an actual increase in the amount of flaking from approximately 5% to 10% is observed as the crater coverage increases.

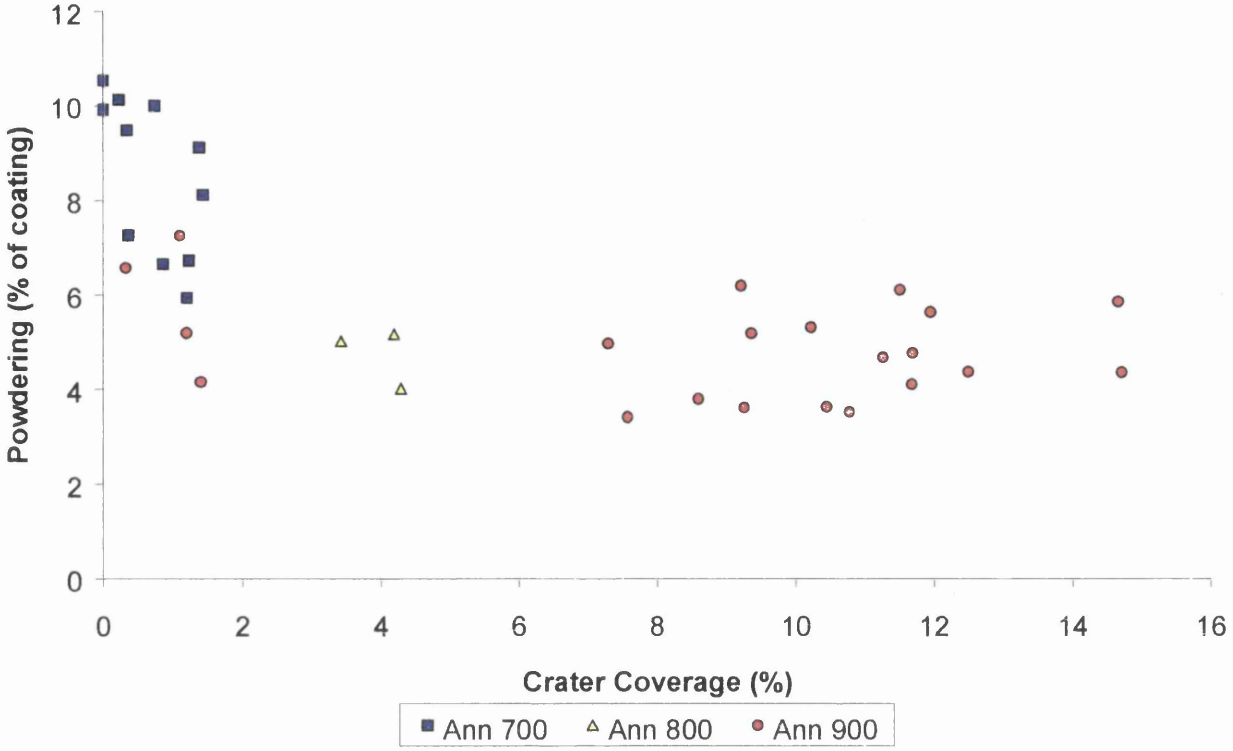

Figure 6.37. Variation of powdering with crater coverage and annealing temperature.

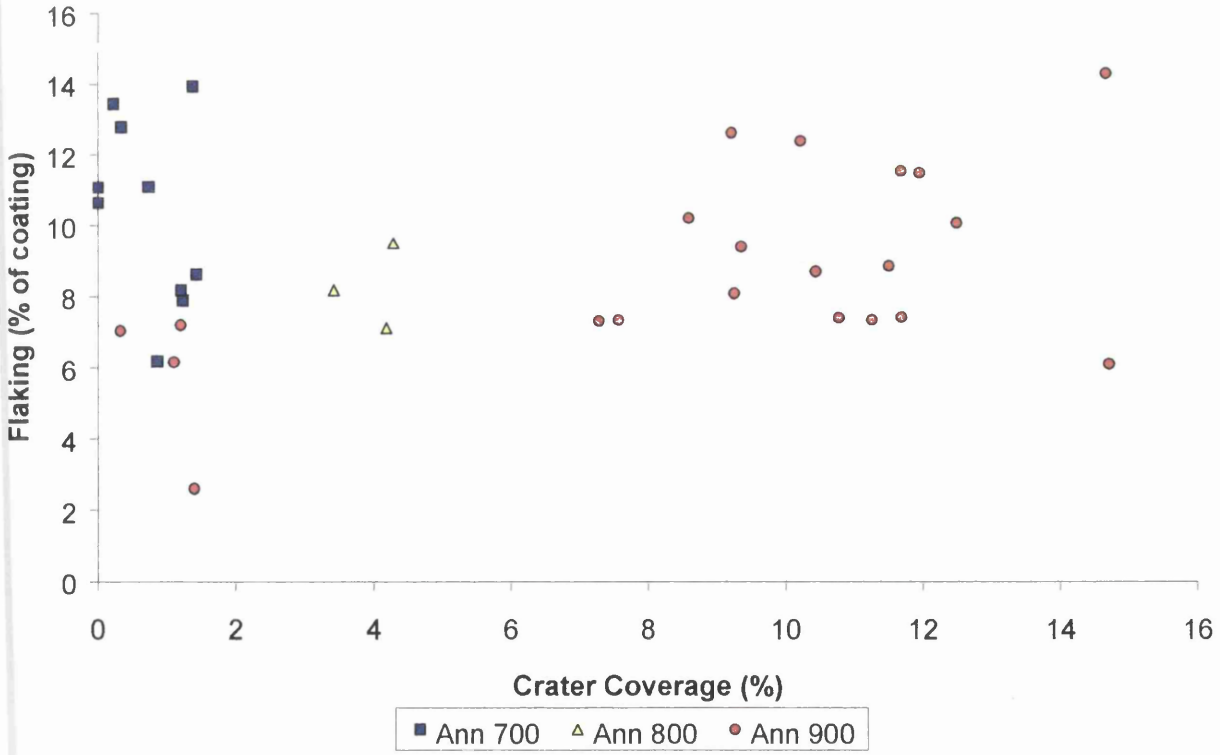

Figure 6.38. Variation of flaking with crater coverage and annealing temperature.

The combined loss of coating through both powdering and flaking is shown in figure 6.39. Zero correlation is observed between the total coating loss and the crater coverage.

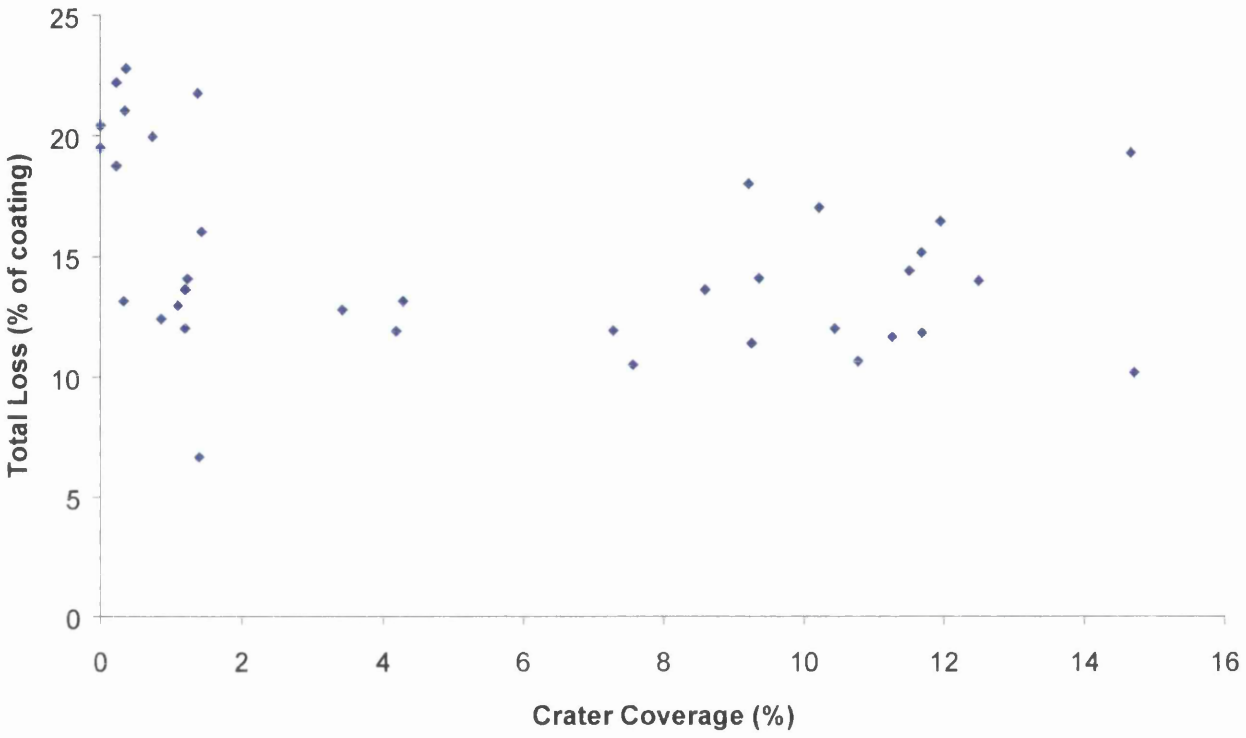

Figure 6.39. Variation of total coating loss with crater coverage.

To aid the press forming operation it is possible to apply lubricating oil to the steel strip. Figure 6.40 illustrates the variation of total coating loss (powdering and flaking) with crater coverage and annealing temperature when lubricating oil is applied to the surface. Comparing figures 6.39 and 6.40 it is observed that the application of a lubricating oil reduces the total coating loss from approximately 15% coating loss to approximately 7% coating loss. Figure 6.40 also shows the zero correlation between the total coating loss that has occurred and either the crater coverage or the annealing temperature.

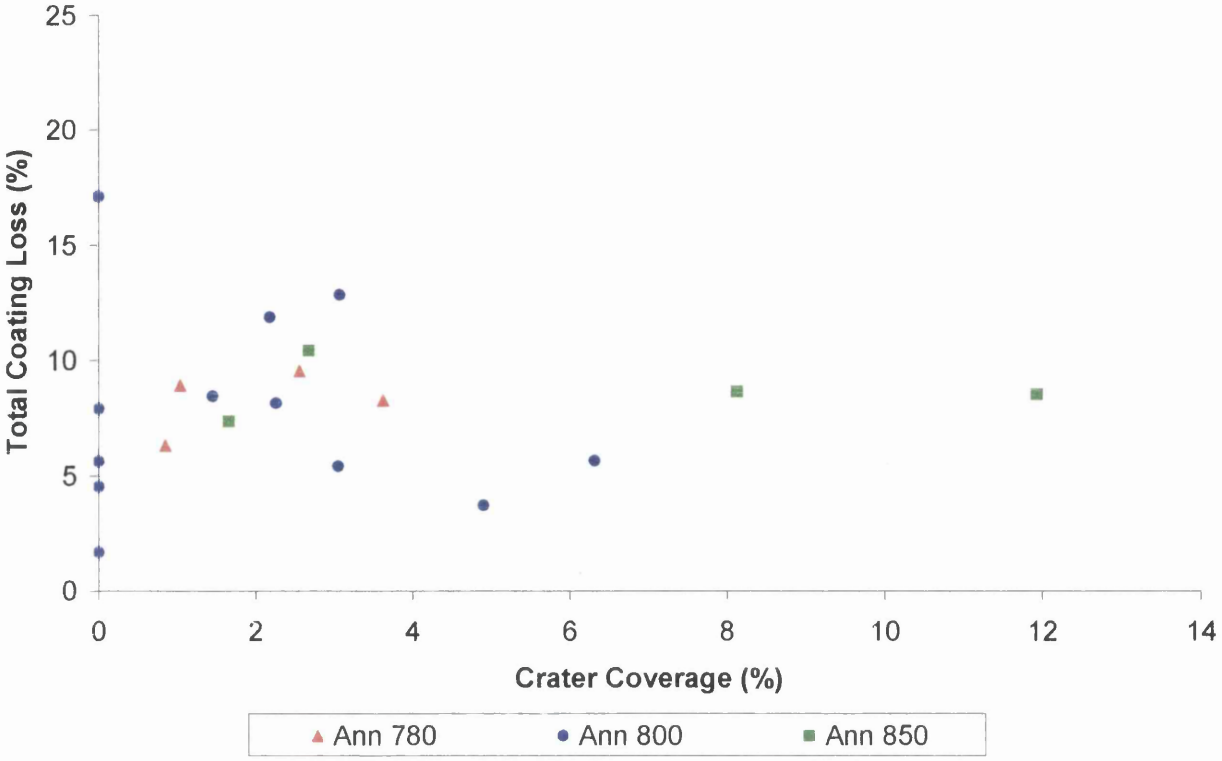

Figure 6.40. Variation of total coating loss with crater coverage and annealing temperature with the application of lubricating oil.

6.4.2 Coating Analysis

As detailed in section 5.6 the formed cup was placed within the JEOL 810A SEM to analyse how the coating and craters had behaved during the cup forming process. The initial analysis was carried out on the top of the cup where the deformation process was minimal. Figure 6.41 shows the deformation of both the normal coating and the ordered craters within it. Crack propagation can be readily seen throughout the entirety of the normal coating, subdividing it up into islands of approximately 30-50μm.

Figure 6.42 shows a close-up image of an ordered crater after minimal deformation. When a crack reaches an ordered crater it can be clearly seen that the crack splits into numerous smaller cracks that then propagate over the rest of the crater. Crack

propagation produces a cracked structure of approximately 5-10μm and is completely independent of the crystal structure within the crater.

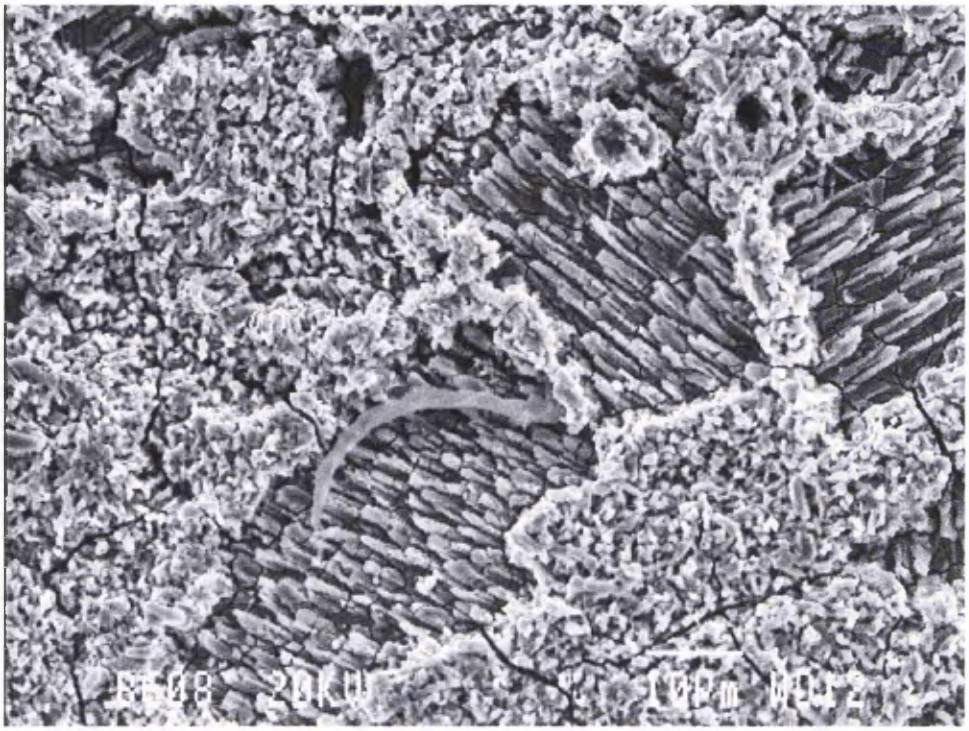

Figure 6.41. Crack propagation on the top surface of the cup (ordered craters).

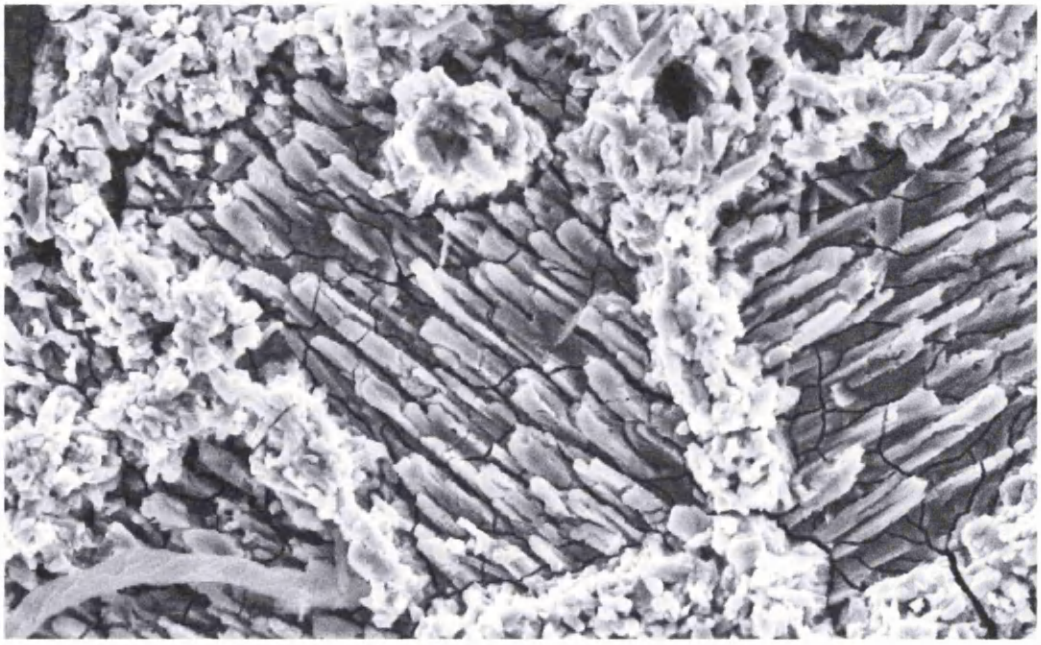

Figure 6.42. Crack propagation through an ordered crater.

When disordered craters are present within the coating the cracking of the coating is very similar, figure 6.43. The normal coating has again cracked into 'islands' of approximately 30-50μm and a close up of the disordered craters, figure 6.44, shows the much finer crack propagation through the crater.

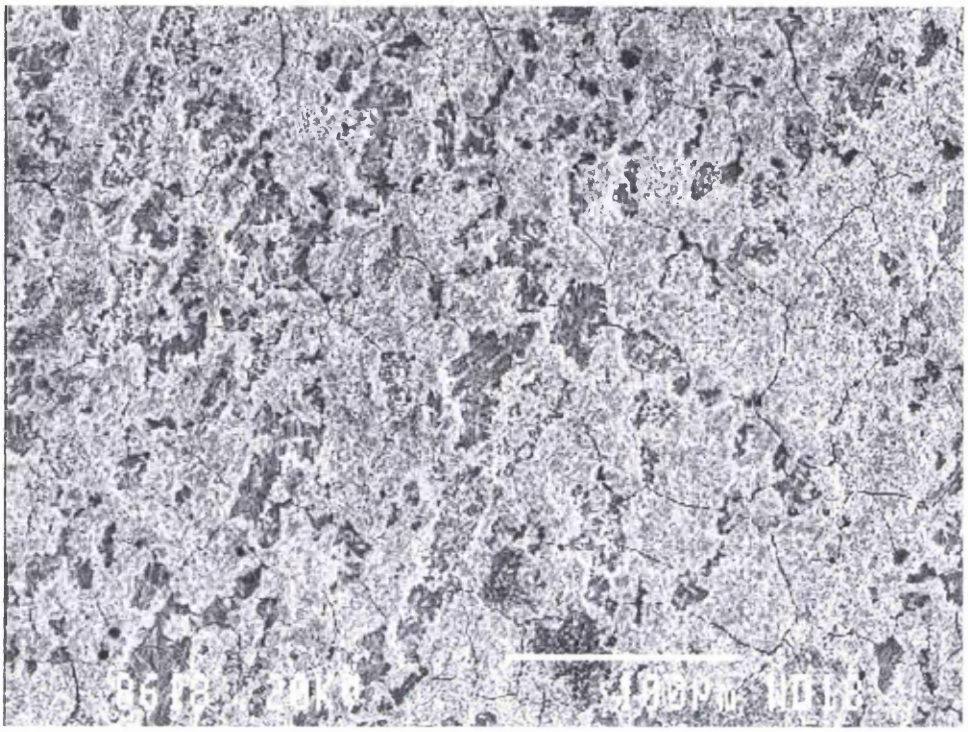

Figure 6.43. Crack propagation on the top surface of the cup (disordered crater).

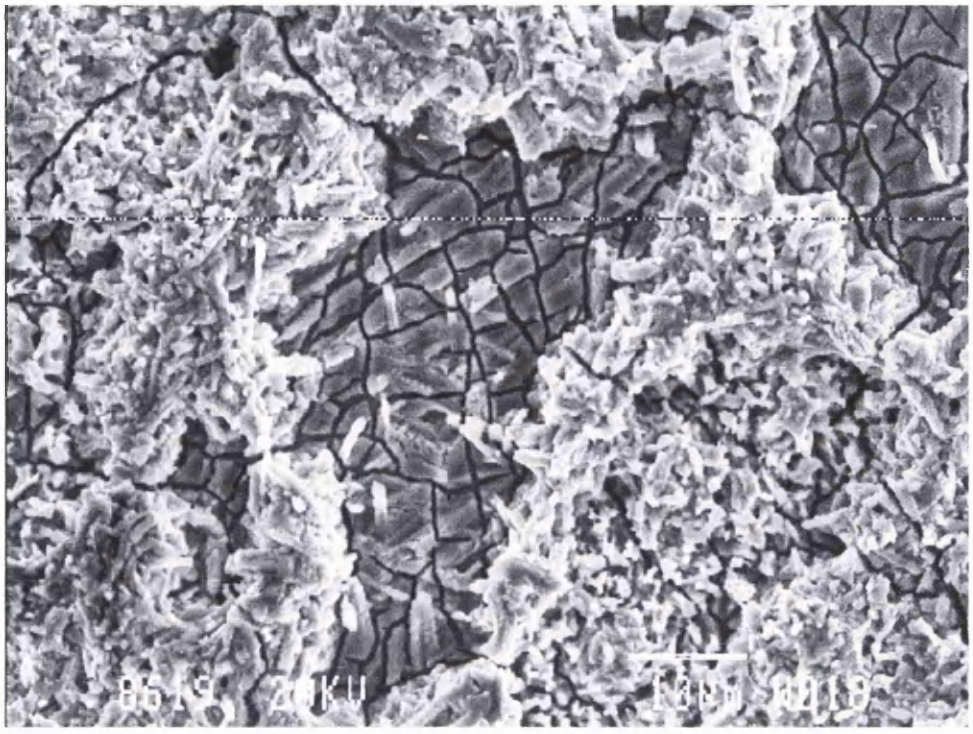

Figure 6.44. Crack propagation through a disordered crater.

Figure 6.45 shows the coating of a sample that has been annealed at 700°C and has a low crater coverage. Images from the top, middle and bottom of the wall are shown for both the inside and the outside. At the top of the wall slight deformation has taken place and the cracking on both the inside and outside has occurred perpendicular to the direction of deformation. Comparing the inside and outside it can be seen that the cracking is more pronounced on the outside compared to the inside. In addition, gaps within the coating can also be seen going all the way down to the substrate.

Further down the side of the cup the cracking has again occurred perpendicular to the direction of deformation and gaps within the coating are again seen extending down to the substrate. However, when the inside and outside of the cup are compared the cracking is considerably more pronounced on the outside than the inside.

At the bottom of the cup the cracking is considerably less and now occurs in all directions. The gaps within the coating are still observed and the cracking on the outside of the coating is again more pronounced than that on the inside.

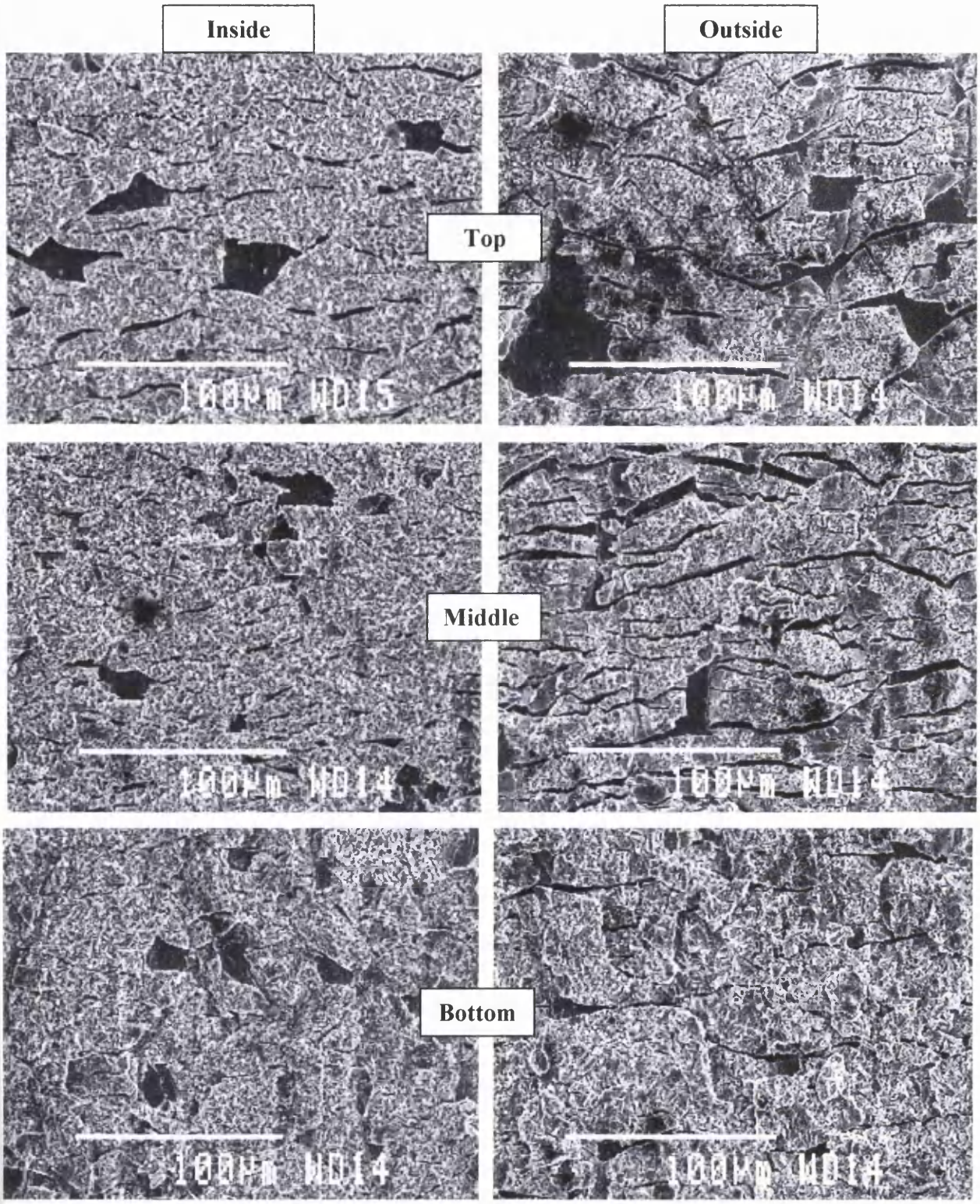

Figure 6.45. Coating deformation of a sample annealed at 700°C that has low crater coverage.

Figure 6.46 shows the coating of a sample that has been annealed at 900°C and has high crater coverage. Images from the top, middle and bottom of the wall of the cup are shown for both the inside and the outside. At the top of the wall slight deformation has taken place and the cracking of the coating has occurred perpendicular to the direction of the deformation on both the inside and the outside of the cup. The craters within the coating have also begun to crack and deform with the coating. In addition, on the outside of the cup there are gaps within the coating that go all the way down to the substrate.

Further down the side of the cup the deformation has become more pronounced and the coating has now cracked in all directions. The number of gaps that go down to the substrate has increased dramatically with the coating on the outside showing a greater degree of coating failure compared to the inside. Furthermore, the coverage of ordered craters within the coating has decreased.

Finally, at the bottom of the cup the coating has cracked in all directions with large quantities of the coating becoming detached from the substrate. Practically zero ordered crater coverage is seen over the sample.

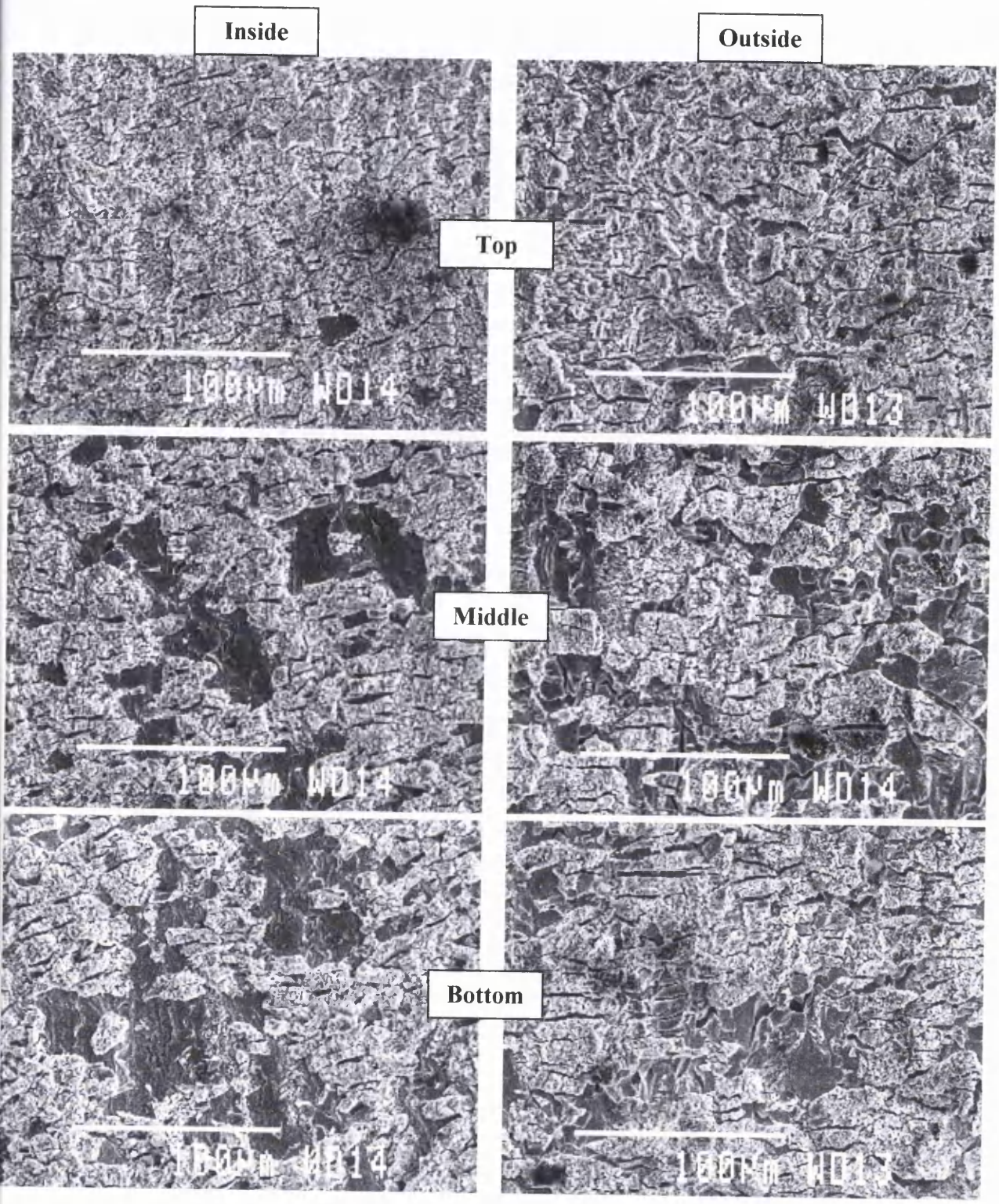

Figure 6.46. Coating deformation of a sample annealed at 900°C that has a high crater coverage.

6.4.3 Substrate Analysis

As detailed in section 5.6, the coating of the formed cups was removed using inhibited hydrochloric acid so that the underlying substrate could be analysed. SEM images of the substrate were taken from the outside of the cup at the top, middle and bottom of the wall.

Figure 6.47 shows the substrate of a sample annealed at 700°C. At the top of the wall the deformation is minimal and the exposed grain boundaries run in all directions forming an equiaxed structure. At the middle of the wall the exposed grain boundaries are running parallel to the direction of the deformation producing an elongated structure. A very similar structure is also observed at the bottom of the cup where deformation is the greatest.

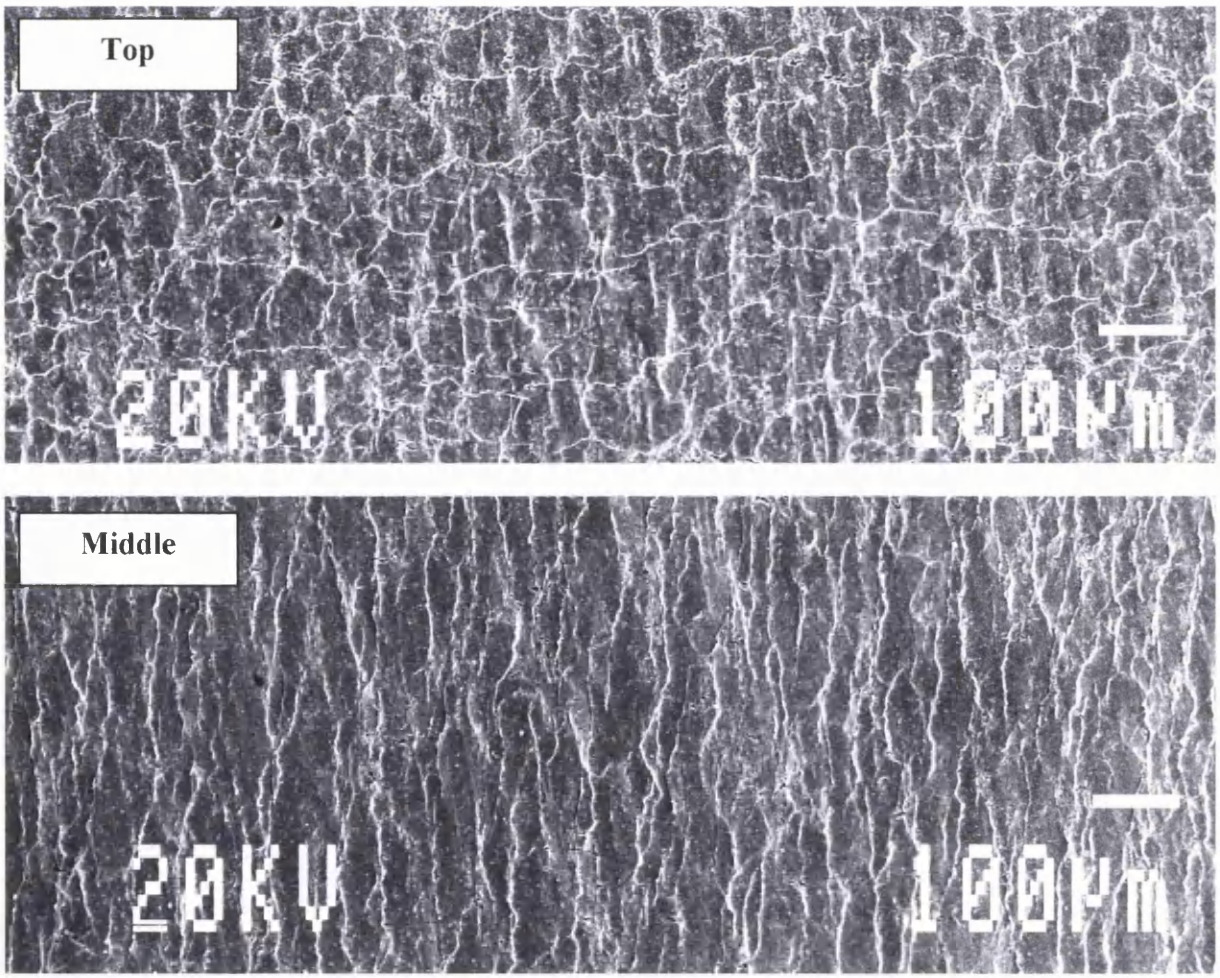

Figure 6.47. Underlying substrate of a formed sample annealed at 700°C.

The underlying substrate of a sample annealed at 900°C is shown in figure 6.48. Deformation at the top of the wall is observed to be minimal although slight cracking of the substrate is observed in places. Further down the side of the wall the amount of deformation has increased and a greater degree of cracking within the substrate is observed. In addition, the substrate has become rougher and more undulating. At the bottom of the cup where the amount of deformation is the greatest very little cracking of the substrate is observed. The number of exposed grain boundaries has increased rapidly producing a very fine equiaxed structure that is considerably rougher and more undulating than that at the middle of the wall.

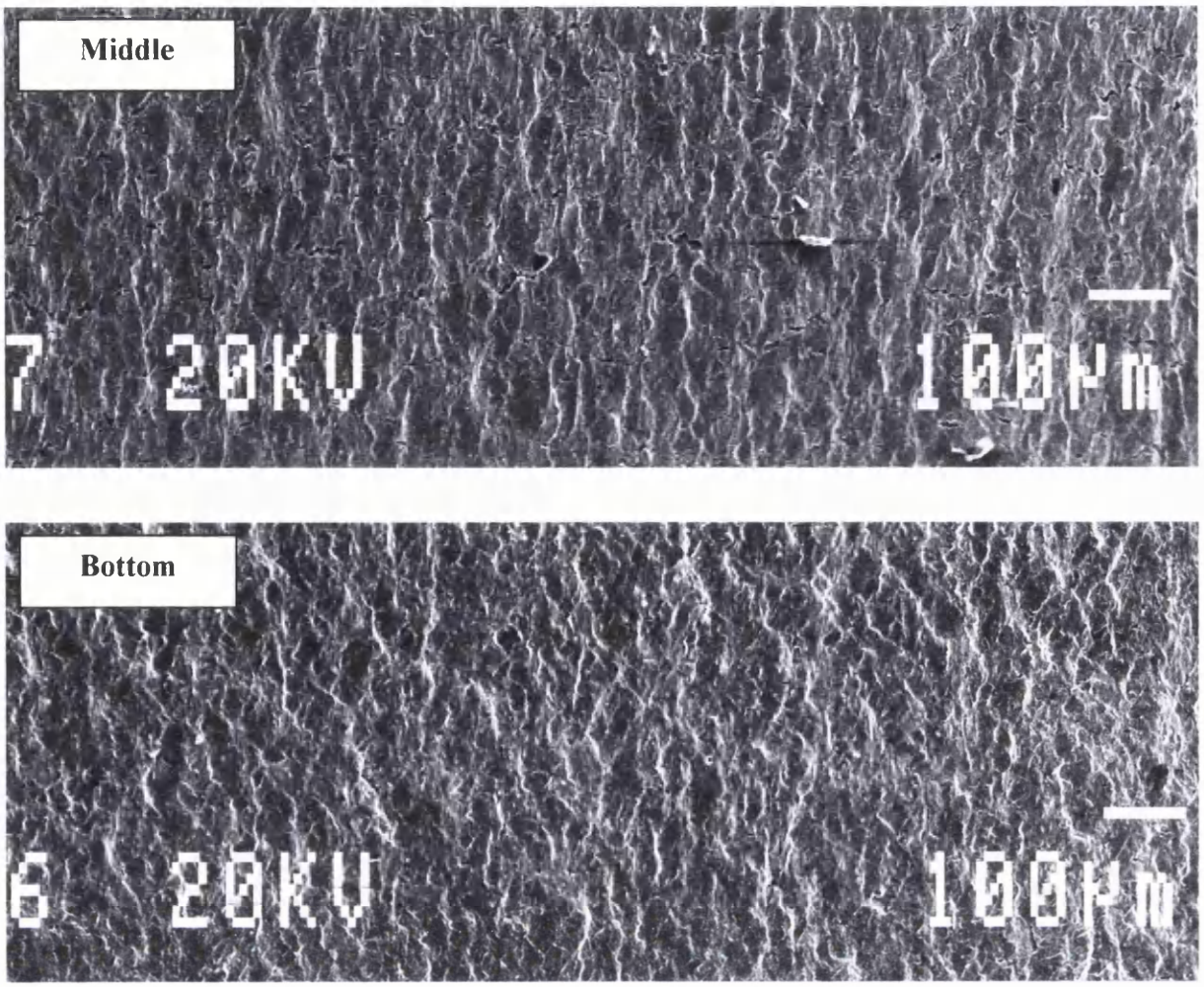

Figure 6.48. Underlying substrate of a formed sample annealed at 900°C.

6.4.4 Discussion

The works of Carless (2000) and Wright (1998) have reported the beneficial effects that craters have upon the powdering and flaking properties of the galvanneal coating. This investigation has analysed the coating failure properties and mechanisms under laboratory controlled conditions.

The initial work centred around ensuring that no external factors were influencing the powdering and flaking properties, namely the coating weight and the iron content. In terms of the iron content the variation experienced showed no correlation with the amount of powdering or flaking that had occurred, figures 6.32 and 6.33. This was due to the small variation (14-17.5wt%) in the iron content as a result of the

controlled laboratory conditions under which the samples were produced. With the coating weight, as shown in figures 6.34 and 6.35, an increase leads to an increase in both the amount of powdering and the amount of flaking. This can be explained firstly by the fact that if there is more coating i.e. a higher coating weight, then there is simply more coating available to come off during pressing leading to a greater weight loss. Secondly a thicker coating will result in less clearance between the coating and the forming tools, greater friction and thus the failure of more coating. The effect of coating weight was therefore nullified by using the percentage of coating that had failed rather than simply the amount that had failed per cup. This therefore meant that any changes in powdering and flaking would be due to the effects of either craters or the annealing temperature.

As stated in section 6.2.4 the annealing temperature influences the coverage of craters within the galvanneal coating by providing more nucleation sites upon which the craters can form. However, as well as providing more nucleation sites a higher annealing temperature also produces a more ductile substrate. During deformation the more ductile substrate will form more easily and thus may have an influence upon the failure mechanisms of the coating. Therefore, to determine whether it was the substrate or the craters that were influencing the coating it was necessary to produce a coating with varying degrees of crater coverage but with identically annealed substrates.

The work from investigation two has shown that it is not possible to produce craters on a substrate annealed at 700°C and therefore an annealing temperature of 900°C was utilised. Producing low crater coverage on a highly annealed substrate was achieved, as shown in section 6.2.4, by using a higher galvannealing temperature for a shorter period of time. The shorter period of time was needed to ensure the iron content of the coating remained similar.

In terms of the effect of craters upon powdering it can be seen in figure 6.37 that an increase in the crater coverage has very little affect upon the amount of powdering that occurs. This is best illustrated by the substrate annealed at 900°C, as the coverage increases from 0% up to 15% no change in the amount of powdering occurs.

However, if the 700°C substrate and the 900°C substrate are compared it can be seen that lower powdering is experienced with the higher annealing temperature. This shows that it is in fact the higher annealing temperature that reduces the amount of powdering and that craters form simply as a result of this higher annealing temperature.

The exact nature as to how a higher annealing temperature and more ductile substrate improves the powdering properties is shown in figures 6.47 and 6.48. It can be clearly seen that the different annealing temperatures affect the way in which the underlying substrate has deformed. The substrate annealed at 900°C has deformed in a much more uniform way compared to the substrate annealed at 700°C. This would lead to less stress building up within the coating and thus a smaller degree of powdering. A schematic diagram of this effect is shown in figure 6.49.

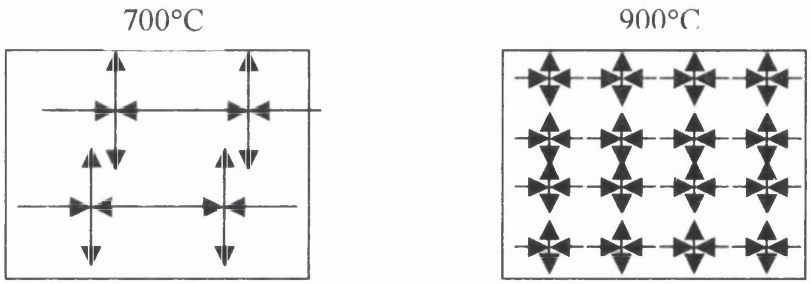

Figure 6.49. Variation in substrate deformation with annealing temperature.

In terms of the effect upon the flaking properties of the coating, figure 6.38, it can be seen that an increase in the crater coverage actually increases the amount of coating loss. By considering the samples annealed at 900°C it can be seen that higher crater coverage produces a greater amount of coating loss. The exact reason behind this has not been ascertained in this investigation but could possibly be linked to the increased roughness associated with increased crater coverage. This would lead to greater friction between the coating and the die that would in turn lead to a greater degree of flaking.

Carless (2000) suggested that the plateau beneath the crater might act as a crack inhibitor and therefore help to improve the flaking properties of the coating. From figures 6.42 and 6.44 it can be seen that even at minimal deformation crack

propagation occurs across both ordered and disordered craters. The crack propagation is much finer through the crater than compared with the surrounding coating. This would have the effect of dissipating the energy of crack thus inhibiting their propagation. However, this occurs at such minimal deformation that the effect can be considered negligible. Indeed, at higher deformations, figure 6.46, it can be seen that the craters have themselves become detached from the substrate. This suggests that the same crack propagation that has affected the normal coating has also affected the craters.

If the low crater coverage samples are analysed it can be seen that an increase in the annealing temperature results in a slightly lower amount of flaking. This can again be explained by the variation in deformation mode for the differently annealed substrates. The more uniform deformation experienced by the 900°C substrate would result in less stress being experienced at the Γ/substrate interface. This in turn would reduce the amount of crack propagation and the degree of flaking.

6.4.5 Summary

This investigation has revealed how the variation in coating failure that had previously been linked to the presence of craters within the galvanneal coating is in fact the result of variation in ductility of the underlying substrate. It has been shown that a higher annealing temperature helps improve both the powdering and flaking properties of the coating. Furthermore, the plateau that lies under the crater does not act as an effective barrier to crack propagation along the brittle Γ/substrate interface. Finally it has also been shown that an increased crater coverage for a given annealing temperature actually leads to a greater amount of flaking.

6.5 EXPERIMENTAL INVESTIGATION FIVE

Development and testing of a model, based on diffusion couples, to predict the coating constitution of the galvanneal coating produced on the Rhesca hot dip simulator.

Using the principle of diffusion couples a model was constructed to predict the formation of the four main phases present within the galvanneal coating, η, ζ, δ and Γ. The initial part of the experimental investigation was carried out to assess whether or not the published values for the diffusion coefficient of iron in zinc were applicable to the galvannealing reaction. The experimental investigation then went on to determine the accuracy of the model and at the same time the best data for the diffusion of zinc through the inhibition layer.

6.5.1 Diffusion Coefficient of Iron in Zinc

The formation of the galvanneal coating occurs by diffusion of the iron atoms from the substrate into the zinc coating. Determination of the diffusion coefficient of iron through zinc was therefore imperative to the validation and development of the GAModeller.

Figure 6.50 shows the variation of iron, zinc and aluminium content through the coating of a sample galvannealed for ten seconds at 500°C. The iron content of the coating increases the closer to the substrate the analysis is taken. The opposite is seen for the zinc content which shows an almost mirror image of the iron content and decreases with proximity to the substrate. Finally, the variation of the aluminium is much more erratic but shows a general decrease in concentration the closer to the substrate the analysis is taken.

A plot of the log of the iron content against the square of the distance into the coating is shown in figure 6.51. The three distinct groups of the ζ, δ and Γ phases are shown along with the gradient of each of the lines.

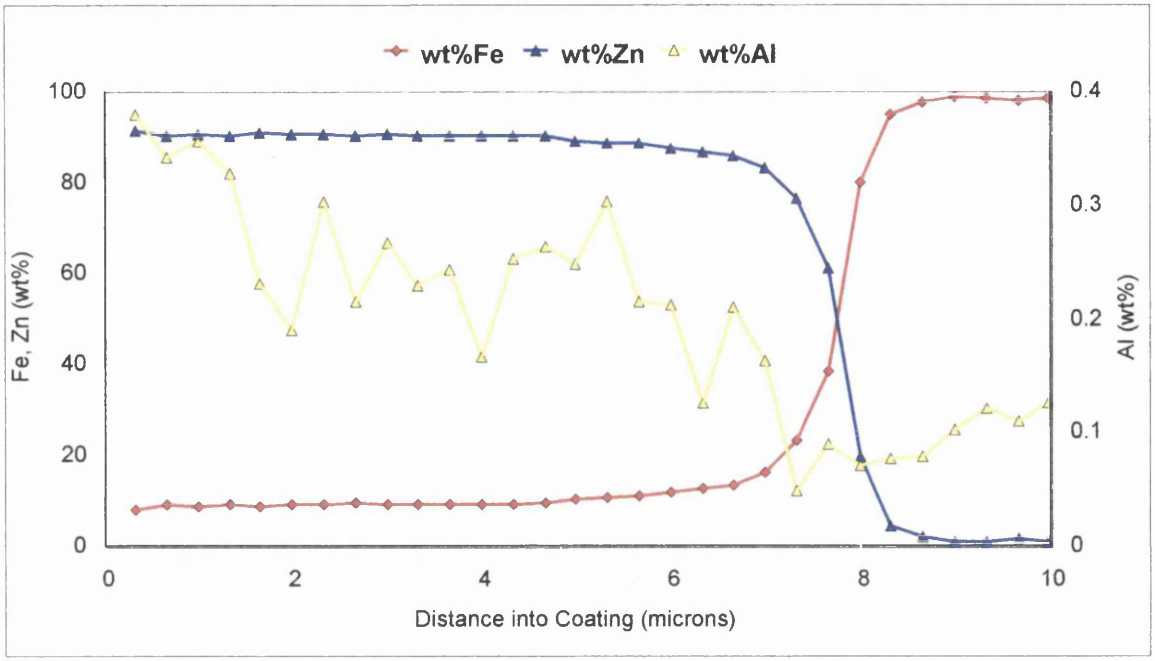

Figure 6.50. Variation of iron, zinc and aluminium content in a galvannealed sample.

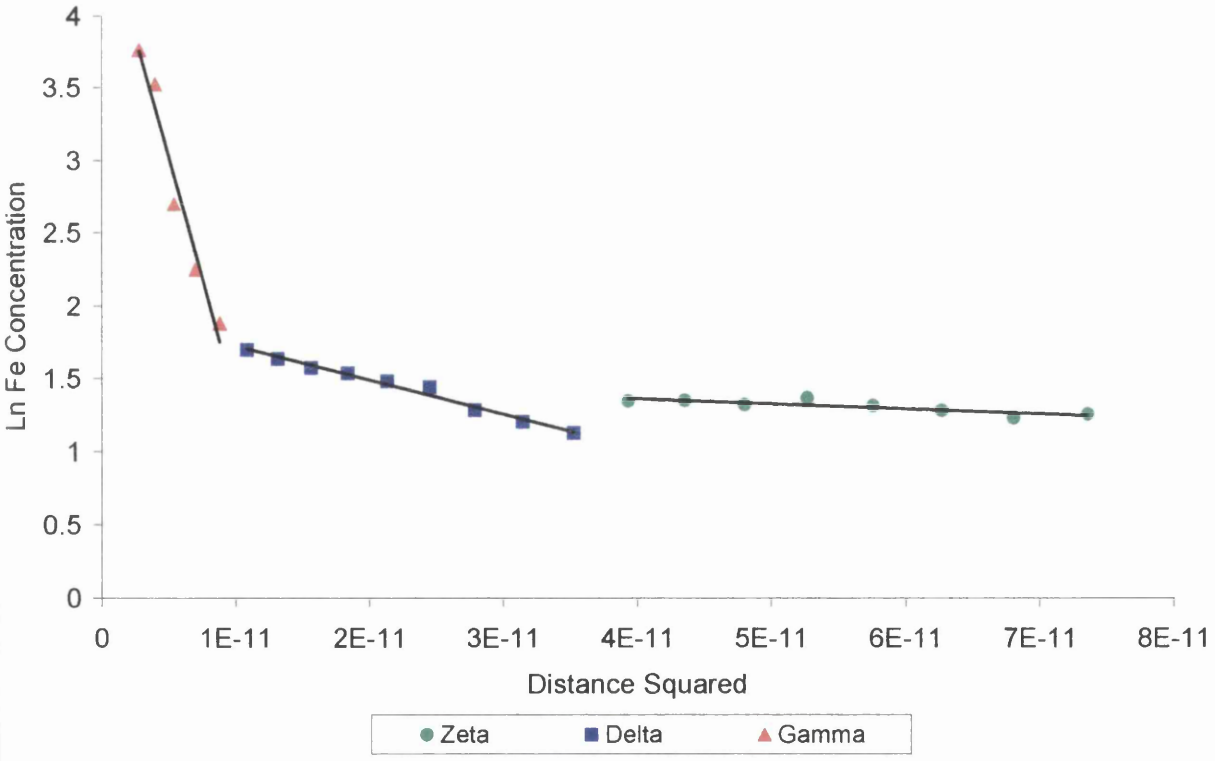

Figure 6.51. A plot of the log of iron content against the square of the distance into the coating.

Using equation 3.13 the diffusion coefficient of iron in the three different phases at 500°C was calculated. Table 6.6 compares the diffusion coefficients calculated from the gradients with those calculated using the published values of D_o and Q, as detailed in table 3.1. A close match can be seen between the values for all three phases.

Table 6.6. Comparison of diffusion coefficients of iron at 500°C

Phase	Measured	Published
Zeta (ζ)	7.29×10^{-12}	5.36×10^{-12}
Delta (δ)	1.07×10^{-12}	1.04×10^{-12}
Gamma (Γ)	7.61×10^{-14}	6.27×10^{-14}

6.5.2 Microsoft Visual Basic™ Graphical User Interface

The model was produced using the Microsoft Visual Basic™ programming language (see appendix A for the annotated code) to make it both easy and flexible to use. This enabled the production of a graphical user interface (GUI) through which the user could easily input data and rapidly receive information in both numerical and graphical format.

Figure 6.52 shows the GUI produced for the GAModeller. In the top left hand corner the user inputs information such as the coating thickness, galvannealing temperature, galvannealing time and effective aluminium. The model then calculates the coating constitution and displays it in several formats. In the bottom left hand corner the model displays a graph of the coating development with time while in the top right hand corner a schematic diagram is displayed. In addition both the thickness and percentage of the individual phases is displayed in a numerical format in the bottom right hand corner. Further information is also displayed within the model such as the iron content of the coating, the equivalent coating weight, an approximation to the amount of powdering and the thickness of the inhibition layer. Finally, so that the model can be applied to online production facilities there is also the ability to switch between HDS mode and online mode. By switching to online mode the model

calculates the coating constitution based upon the line speed rather than the galvannealing time.

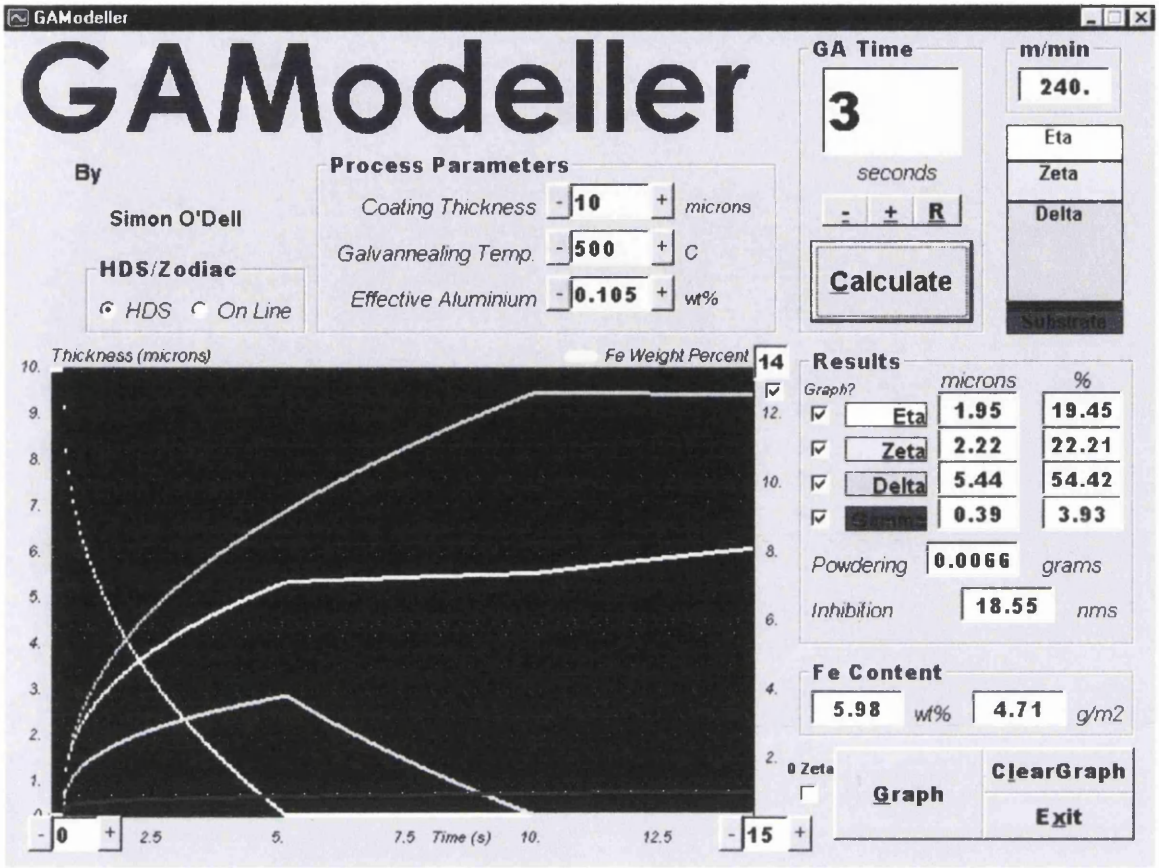

Figure 6.52. Graphical User Interface (GUI) of the GAModeller.

6.5.3 Testing and Validation

Testing and validation of the GAModeller was carried out on the Rhesca hot dip simulator. Panels of TiNb IF steel were produced with varying effective aluminium, galvannealing time and galvannealing temperature. The coating constitution of the coating was then analysed using XRD and the results compared to those predicted by the GAModeller. Two different published values were used for the diffusion of zinc through the aluminium inhibition layer and the results compared to see which values gave the best results.

Figures 6.53 to 6.56 show the difference between the measured and modelled amounts for each of the four phases. A positive value on the vertical axis shows that the

modelled value for that particular sample was higher than the amount measured using XRD. A negative value shows that the modelled value was lower than the measured value.

Figure 6.53 shows the difference between the modelled and measured values for the η phase. For some samples the model has under predicted the amount of η within the coating. The greatest of these is for samples GAM8 and GAM13 where the model under predicts the amount by 80%. In these cases the XRD analysis has measured considerably more galvannealing than has been predicted by the model. For other samples the model has over predicted the amount of η within the coating. The greatest of these is with sample GAM5 where the model over predicts the amount of η by 72.4%. However, this is only when the 'A' set of diffusion values is used, if the 'B' set of values is used then the over prediction decreases to 50.0%.

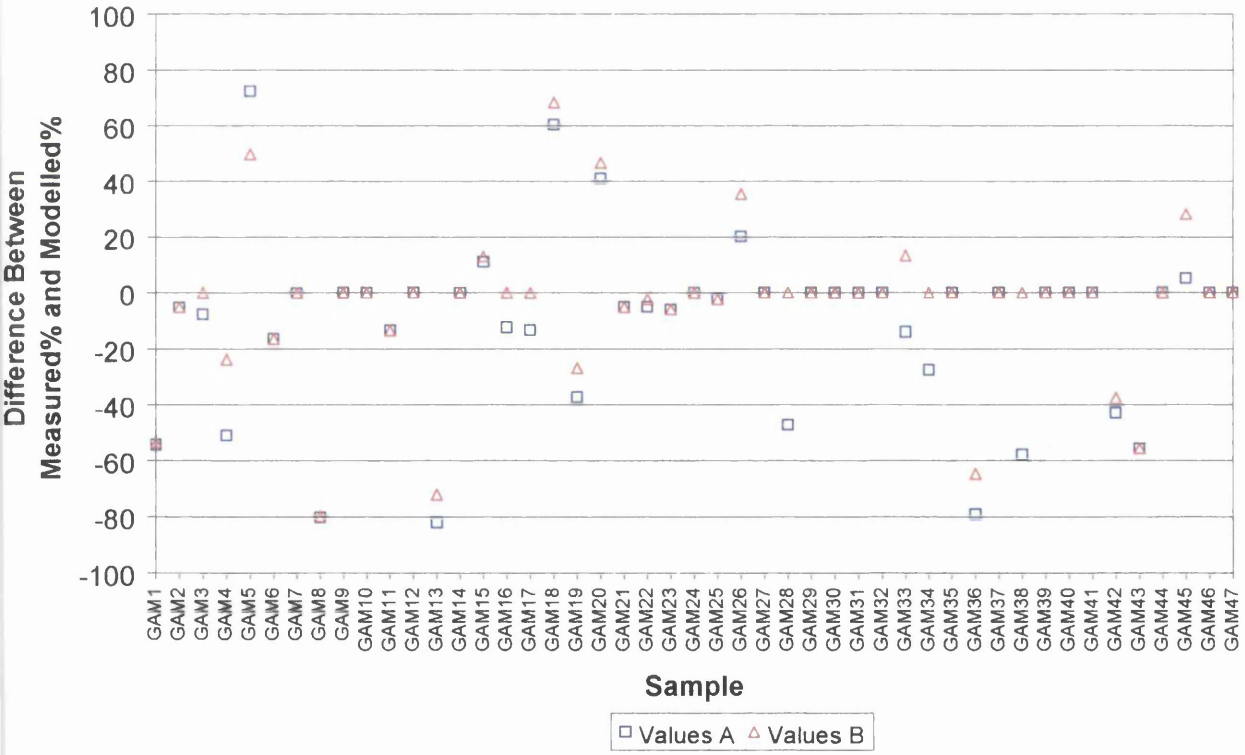

Figure 6.53. Difference between measured and modelled values for the η phase.

Overall it can be seen that the points deviate around the zero mark on the graph. The average for all the measurements is –10.8% for the 'A' values and –4.5% for the 'B' values. This suggests that the 'B' values would give better results than the 'A' values.

On average it can be stated that with the 'A' diffusion values the model under predicts the amount of η present within the coating by 10.8% and with the 'B' values by 4.5%. If the average deviation is analysed then the 'B' diffusion values also give a better result of 17.1% compared to the 'A' diffusion values of 21.8%. This shows that on average the 'B' diffusion values give a variation on the measured values for the η phase of $\pm$17.1%. For a ten micron coating this would be approximately two microns.

The difference between the measured and modelled values for the ζ phase is shown in figure 6.54. The difference between the measured and modelled values for the ζ phase is quite small. The greatest over prediction is just 20.2% for sample GAM8 and means that the XRD measurements have shown less galvannealing than that predicted by the model. The greatest under prediction is 26.2% for sample GAM20 and means that the XRD measurements have shown more galvannealing than that predicted by the model. In addition it should also be noted that those samples galvannealed above 530°C had no ζ phase present within the coating. The best example is sample GAM43 that had been dipped in a spelter containing 0.16wt% effective aluminium and galvannealed at 573°C for six seconds. The XRD measurements for this sample showed there was 44.3% δ, 55.7% η, 0% ζ and 0% Γ.

Overall it can be seen that the points on the graph deviate around the zero mark. The average for all the measurements is 1.5% for the 'A' values and 0.1% for the 'B' values. This suggests that the 'B' diffusion values give the best results by over predicting the amount of ζ, on average, by just 0.1%. The average deviation for the ζ phase is 5.1% for the 'A' values and 3.5% for the 'B' values. It can therefore be stated that on average the 'B' diffusion values give a variation on the measured values of $\pm$3.5%.

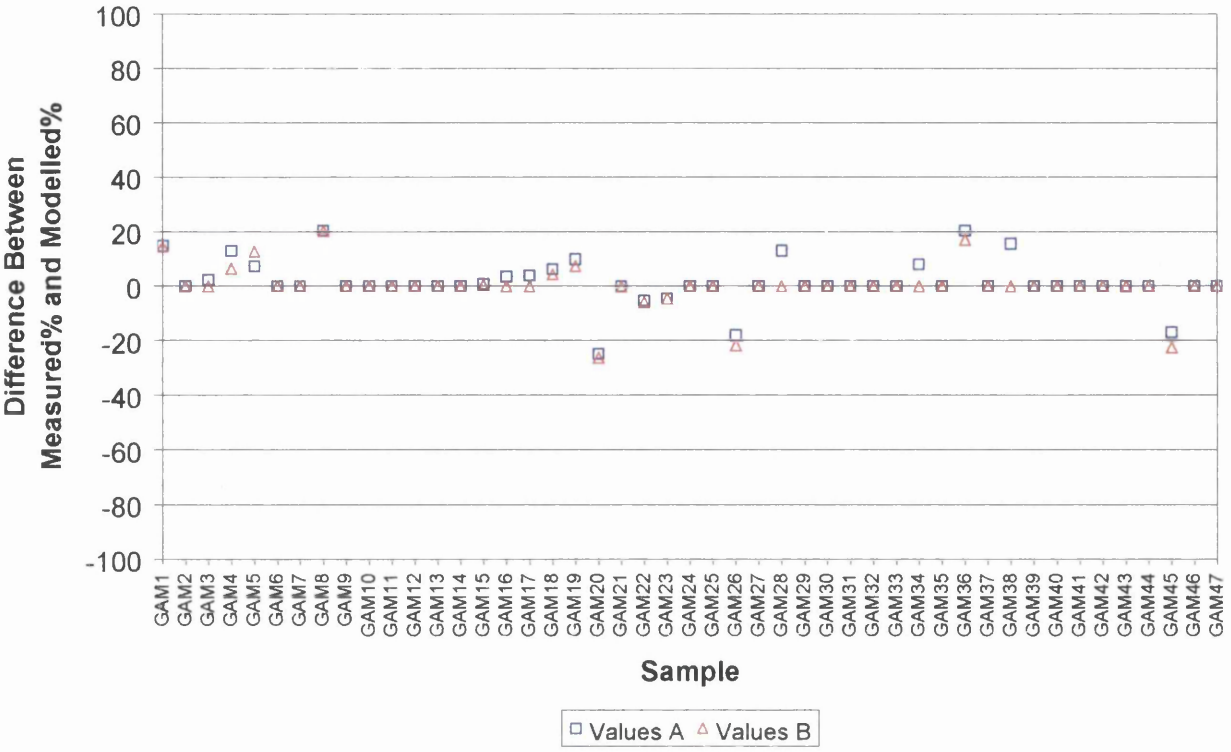

Figure 6.54. Difference between the measured and modelled values for the ξ phase.

Figure 6.55 shows the difference between the measured and modelled values for the δ phase. A large scatter around the zero mark is observed for both the 'A' and 'B' diffusion values. The greatest under prediction of 75.3% is seen with sample GAM5 when the 'A' diffusion values are used. The greatest over prediction is seen with sample GAM13 where the model over predicts by 79.7%. The average for all the measurements is 9.3% for the 'A' diffusion values and 4.7% for the 'B' diffusion values. Therefore, on average, when the 'B' diffusion values are used the model over predicts the amount of δ phase by 4.7%. The average deviation for the δ phase is 16.8% for the 'A' diffusion values and 14.3% for the 'B' diffusion values. It can therefore be stated that, on average, when the 'B' diffusion values are used the variation from the measured values is ±14.3%.

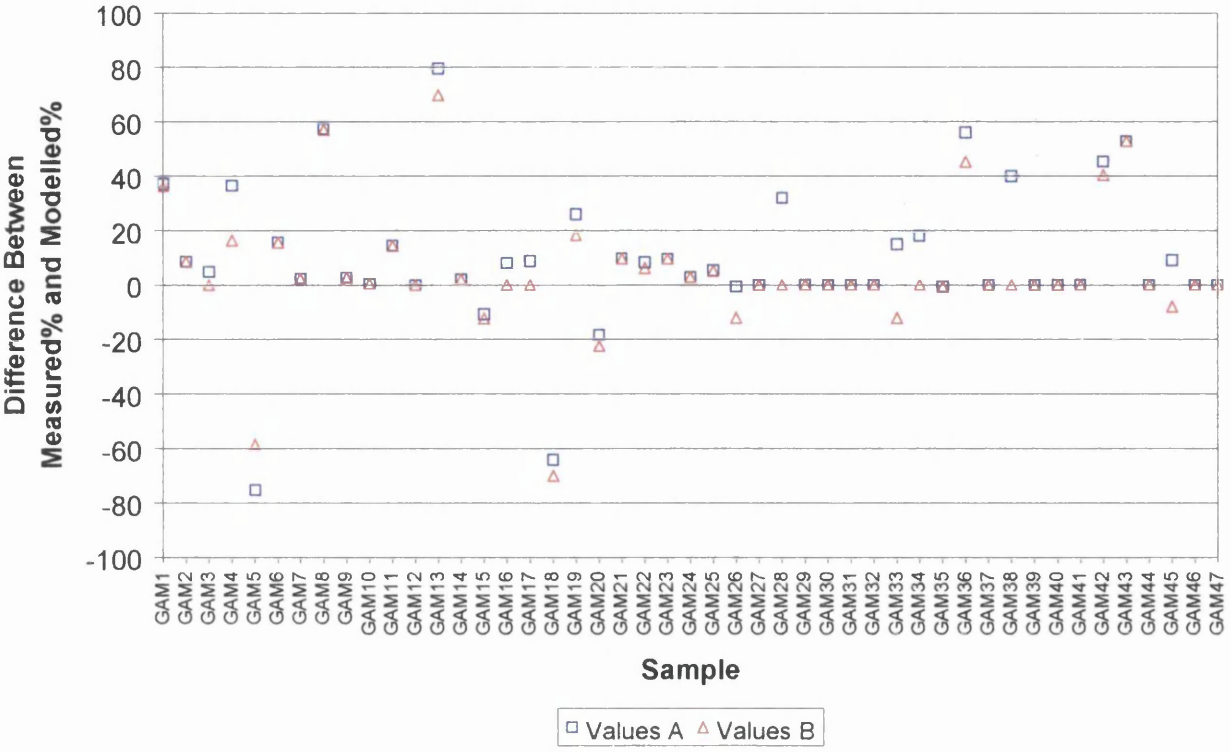

Figure 6.55. Difference between the measured and modelled values for the δ phase.

The difference between the measured and modelled values for the Γ phase are shown in figure 6.56. The difference between the modelled and measured values is seen to be extremely small. The average for all the measurements is just -0.1% for the 'A' diffusion values and –0.3 for the 'B' diffusion values. The average deviation for the 'A' and 'B' diffusion values are 1.5% and 1.4% respectively. It is therefore possible to state that, on average, when the 'B' diffusion values are used the model under predicts the amount of Γ phase by 0.3% and has a variation from the measured values of ±1.4%.

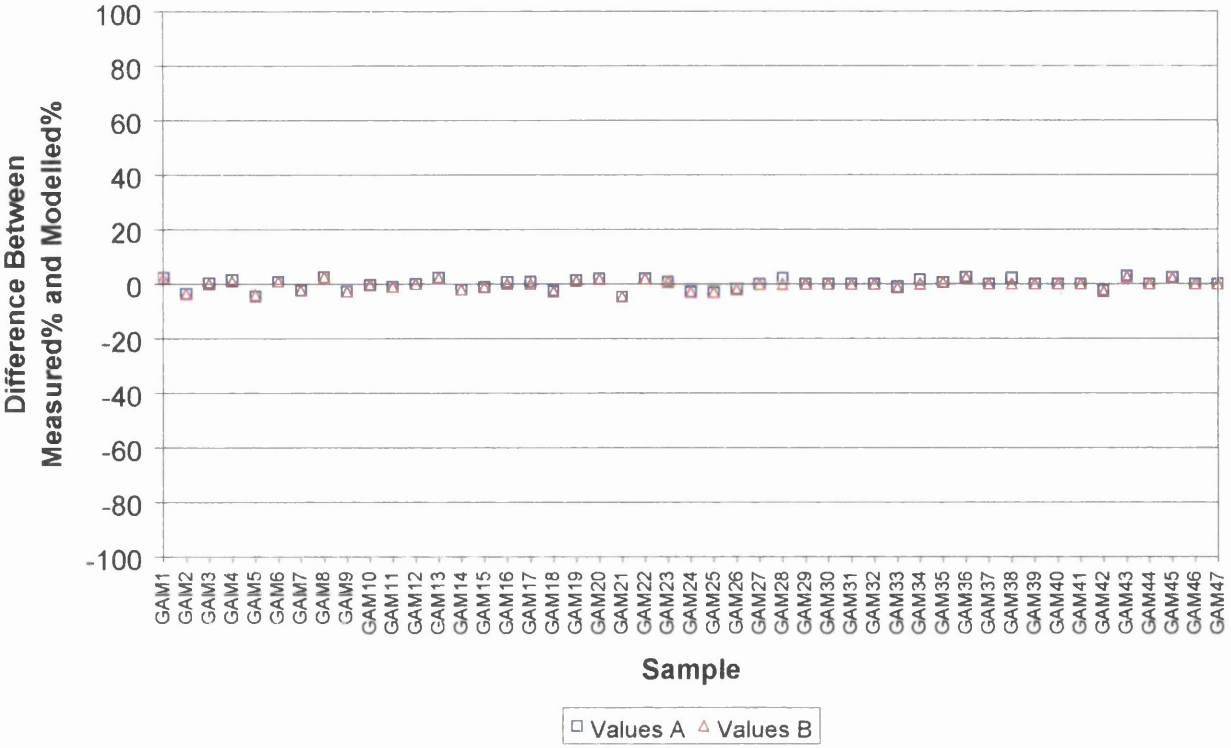

Figure 6.56. Difference between the measured and modelled values for the Γ phase.

Table 6.7 summarises the average values for each of the individual phases and diffusion values. In terms of the average prediction difference it can be seen that the 'B' diffusion values give results closer to zero in all cases except for the Γ phase. In terms of the average variation in prediction the 'B' diffusion values give the smallest variation for all of the phases.

Table 6.7. Average prediction and average variation for each phase and values.

Phase	Average Prediction Difference		Average Variation in Prediction	
	'A' Values	'B' Values	'A' Values	'B' Values
Eta (η)	-10.8	-4.5	21.8	17.1
Zeta (ζ)	1.5	0.1	5.1	3.5
Delta (δ)	9.3	4.7	16.8	14.3
Gamma (Γ)	-0.1	-0.3	1.5	1.4

6.5.4 Discussion

This investigation has analysed the possibility of using the principle of diffusion couples to model the coating constitution of the galvanneal coating. The investigation has also sought to determine the most appropriate diffusional data for use within the model.

The initial work set about determining whether or not the diffusion co-efficients published by Wakamatsu (1997) in the Smithells Metals Reference Book were applicable to the galvannealing reaction. The results verify that the values for the pre-exponential factor (D_0) and the activation energy (Q) for the different phases are suitable for use within the GAModeller.

The majority of the work in this investigation focused around the testing and validation of the model and the determining of the diffusion values of zinc through the inhibition layer. Both of these were conducted simultaneously and the results are shown in figures 6.53 to 6.56 and table 6.7. A large scatter in the points for both sets of diffusion values is seen for the η and the δ phase. However if the graphs are analysed closely it can be seen that they are in fact almost mirror images of each other. For example if sample GAM5 is analysed it can be seen that for the η phase the model over predicts by 72.4% yet for the δ phase it under predicts by 75.3%. This is observed to a greater or lesser degree with nearly all of the samples and is also seen within table 6.7. The average prediction for the η phase, using the 'B' diffusion values, is –4.5 but for the δ phase it is +4.7. The reason for this is the way in which the model predicts the amount of η phase.

To calculate the amount of η phase the model first predicts the thickness of the other three phases and then subtracts their total thickness from the overall coating thickness. Therefore, because the δ phase is the predominant phase within the coating the two will be strongly linked. The greatest variation within the model is therefore related to the prediction of the thickness of the δ phase.

On average, when the 'B' diffusion values are used the model over predicts the percentage of δ by 4.7%. This over prediction in δ may be related to an under prediction of the delaying effect of the inhibition layer. That is if the effect of the inhibition layer was increased, the model would predict less alloying and thus less δ phase. By examining both the 'A' and 'B' diffusion values it can be seen that the 'B' diffusion values hinder the diffusion of zinc through the inhibition layer more than do the 'A' diffusion values. As a result the 'B' diffusion values give a greater amount of inhibition, less alloying and more accurate results. Using diffusion values that hinder the amount of zinc diffusion even more than the 'B' diffusion values could therefore rectify the average over prediction experienced by the model. This is in part to be expected because the diffusion data used is based upon diffusion of zinc in pure aluminium. Obviously the inhibition layer is not pure zinc but an iron, aluminium and zinc mixture. However, due to the extremely thin nature of the inhibition layer practical experiments could not be carried out to determine the exact diffusion values.

Of the two sets of diffusion values used it has been shown that, on average, the 'B' set of diffusion values give the least variation and the most accurate predictions. Therefore to maintain the variation between the modelled and measured values to a minimum and until further work can be carried out the 'B' set of values by D. L. Bdke (1997) will be used within the GAModeller.

In addition to measuring the accuracy of the GAModeller this set of work has also proven that, as predicted by the iron-zinc phase diagram, no ζ is present within the coating if a galvannealing temperature greater than 530°C is used. The reason for this is that a peritectic transformation occurs at 530°C on the iron-zinc phase diagram. Above 530°C the ζ phase is no longer thermodynamically stable and is replaced by the δ phase.

6.5.5 Summary

This investigation has shown how the principle of diffusion couples can be used to create a model that predicts the constitution of the galvanneal coating. The diffusion

co-efficients for the diffusion of iron in zinc, as published by Wakamatsu *et al.*, have been shown to be appropriate to the galvanneal coating. In addition, the diffusion data published by D. L. Bdke *et al.* has also shown to be most appropriate for the GAModeller. On average the model accurately predicts the constitution of the galvanneal coating although the δ phase exhibits quite a large variation of ±14.3%.

7 GENERAL DISCUSSION

The following chapter gives an overall discussion of the whole project, detailing how the individual investigations have worked together towards the overall goal.

7.1 CRATER MEASUREMENT TECHNIQUE

The main thrust of the project has centred on microstructural features within the galvanneal coating known as craters. To be able to carry out any form of investigation into their effects it was necessary to first devise a technique for identifying and measuring the craters within the coating. The rough and undulating morphology of the surface of the galvanneal coating meant that optical microscopy was not a viable option for identifying the galvanneal craters. The only option was therefore to use the scanning electron microscope to take images of the surface of the galvanneal coating. Automated identification of the galvanneal crater could not be achieved because no distinct colour or elemental differential existed between the ordered craters and the surrounding coating. Measurement of the crater coverage was therefore achieved by manually defining the edge of each individual crater and inputting the information into the KS300 image analysis package.

Assessment of this technique has shown that over a single sample the crater coverage can vary quite dramatically and that that by measuring ten images of the surface of the galvanneal coating an accurate representation of the crater coverage can be achieved. The technique, although time consuming, gives valuable information about crater size and morphology as well as an error of just ±6.5%.

7.2 THE INFLUENCE OF PROCESS PARAMETERS

Now that a technique for identifying and measuring galvanneal craters had been developed and tested it was necessary to determine whether or not crater formation could be controlled. Were craters the result of some random uncontrollable parameter or did certain process parameters influence their formation? Use of the Rhesca hot

dip simulator enabled laboratory production of the galvanneal coating under a variety of process conditions. Combining this with the crater measurement technique enabled a complete assessment of the effect of several process parameters upon the crater coverage.

The results showed that an increase in the annealing temperature helped to promote crater formation whereas an increase in the galvannealing temperature hindered crater formation. Modification of the effective aluminium and the strip entry temperature did not affect the actual crater coverage but instead altered the morphology of the craters. Finally neither the spelter temperature nor the temperature after dipping had any effect upon either crater formation or crater morphology. All of this has shown that some degree of control could be achieved over the quantity and type of crater formation. The effect of each process parameter also helped to give an insight into just how and why craters form within the galvanneal coating. In addition, now that some control over crater formation had been achieved easier production and investigation into them could follow.

7.3 CRATER FORMATION

The next step was to work out how and why craters form as the coating develops from the galvanised to the galvannealed coating. The work that had been undertaken analysing the effect of process parameters had already given valuable information as to how craters could be easily formed for this investigation. The previous work had also taken the first steps in identifying why and how craters form.

The increase in crater coverage with increasing annealing temperature has helped to support the fact that, as proposed by Carless (2000), craters nucleate upon grains oriented with {111} in the plane of the sheet. Both the EBSD and the optical microscopy work carried out have confirmed that increasing the annealing temperature from 700°C to 900°C creates an equiaxed microstructure with numerous {111} oriented grains. Further work into the effect of the underlying substrate has shown that craters form within the high angle grain boundaries of {111} oriented grains and can also form over more than one {111} grain as long as they are

contiguous. Now that the nucleation site for the craters has been identified and explained it is necessary to determine what exactly is nucleating upon these {111} oriented grains and just when it is nucleating.

The influence of strip entry temperature on crater morphology together with the lack of effect of both the spelter temperature and the temperature after dipping suggests that the initial nucleation of the crater occurs during the first instances of dipping. During this time it is possible for both the inhibition layer and iron-zinc intermetallics to form on the surface of the substrate. In the case of ordered craters it is the ζ phase that is able to nucleate epitaxially upon the {111} oriented grains. In the case of disordered craters the increase in effective aluminium or the decrease in strip entry temperature that leads to their formation will result in a reduced super-saturation of iron near the substrate. This will therefore result in a much thinner layer of intermetallics forming upon the {111} oriented grains and with a different morphology. It is also believed, though not confirmed by experimental investigations, that a thin layer of inhibition layer is also present beneath the nucleating iron-zinc intermetallics.

The final part of the puzzle was determining just how craters form during the galvannealing process. By analysing both ordered and disordered craters during the formation of the galvanneal coating it was possible to determine that the zinc above the crater remained in a liquid state and was drawn into the surrounding coating. The formation of outbursts along the high angle grain boundaries at the edge of the crater produced a lip that became more pronounced as the galvannealing process continued. However, throughout the whole galvannealing process the initial iron-zinc intermetallics at the base of the crater remained completely unaffected. The reason for this is that the inhibition layer beneath the intermetallics prevents iron diffusing into them and the intermetallics prevent the liquid zinc from breaking up the inhibition layer. In effect they give each other mutual protection. That is, as shown in previous chapter, unless a high galvannealing temperature is used. At the higher galvannealing temperature the iron-zinc intermetallics remelt causing the break down of the inhibition layer and the formation of the normal galvanneal coating.

7.4 COATING FAILURE

The investigations so far have provided a technique for measuring crater density, a greater degree of control over crater formation and a more in-depth understanding of how and why craters form. The final challenge was to determine just what influence craters would have upon the failure of the galvanneal coating.

The previous work of Carless (2000) and Wright (1998) had suggested that craters would reduce the amount of coating failure experienced during press forming operations. Investigation into the effect of crater formation upon the coating failure was carried out by testing samples of different crater coverage with a standard cupping test. The different crater coverages were produced by manipulation of both the annealing and galvannealing temperatures.

The results showed that an improvement in both the powdering and flaking properties was a result of changes in the ductility of the underlying substrate and not the presence of craters within the coating. During pressing the more ductile substrate would deform more uniformly, impose less stress upon the coating and reduce the coating failure. The craters within the coating were simply caused by the more ductile substrate containing more grains with {111} oriented in the plane of the sheet upon which the craters could nucleate.

The work of Carless (2000) compared the coating failure on a TiNb IF steel substrate and a Ti IF steel substrate. The work concluded that the coating on the TiNb IF steel substrate experienced less coating failure than that of the Ti IF steel substrate because of a higher crater coverage. It can be concluded from the current investigation that the improved coating failure experienced by the TiNb IF substrate was in fact due to the more ductile substrate and not the presence of craters. The addition of niobium to the substrate would have helped promote more recovery and recrystallisation compared to the substrate without niobium.

In addition the work also proposed that the plateau beneath the crater would inhibit cracks travelling through the brittle Γ/substrate interface. Analysis of the base of the

craters after minimal deformation showed prolific crack propagation. This suggests that although some crack inhibition may occur the effect would be minimal.

7.5 GAMODELLER

In terms of investigating the coating constitution and surface evolution of the galvanneal coating the work up until now has primarily been involved with the nature and effect of craters. The final piece of work looked much more closely at the make-up of the galvanneal coating in terms of the presence of the individual intermetallic phases.

The major part of this work involved the creation and testing of a model, based on diffusion couples, to predict the quantity of each of the intermetallic phases within the galvanneal coating. The initial part of the work set out to determine whether or not the published diffusion values of iron in zinc were applicable to the galvannealing reaction. The results from this proved successful and the published diffusion data was incorporated into the model. Further testing and validation of the model compared the coating produced on a Rhesca hot dip simulator to that predicted by the model. The results showed a close correlation between the measured and modelled quantities of ζ and Γ. The δ phase showed some scatter and an average over prediction of about 5%. This over prediction was related to the diffusion values utilised for the inhibition layer. The results suggest that the modelled inhibition layer is not hindering the alloying process as much as it should be. A greater hindrance would reduce the amount of alloying and the amount of each of the phases. This is due to the fact that the diffusion values used were based upon the diffusion of zinc through pure aluminium. The inhibition layer is actually an aluminium, iron and zinc mixture that would inhibit the amount of alloying to a much greater extent. However, measuring the actual diffusion values of zinc through the inhibition layer is very difficult due to its extremely thin nature. Therefore until further work can be undertaken into the diffusion of zinc through the inhibition layer the values of D. L. Bdke (1997) will be used within the GAModeller.

7.6 COMMERCIAL RELEVANCE

The current work has shown that the presence of craters within the coating has no positive effect upon the powdering or flaking properties of the galvanneal coating. In addition there is also the possibility that the presence of craters may actually worsen the flaking properties. From a commercial point of view craters should therefore be avoided within the galvanneal coating. However, the work has also shown that a well-annealed substrate will help improve the resistance to coating failure by reducing the stresses imposed upon the coating. In addition, eradicating craters from a well-annealed substrate by increasing the galvannealing temperature may result in excess Γ formation and increased coating failure, in particular because during on-line production the galvannealing time is dictated by the line speed that is in turn controlled by the annealing furnace. Therefore if an improvement in powdering properties is desired the galvanneal producer may have to just accept the presence of craters within the coating.

There is also the possibility that, although craters do not improve the resistance to coating failure, they may be beneficial in another way. The increased roughness of the coating as a result of the presence of craters may help to improve the adhesion of both paints and glues to the galvanneal. This increased roughness helps to promote greater 'keying' between the coating and either the paint or the glue. In addition, work currently being carried out by Wright (1998) under the ILZRO (International Lead and Zinc Research Organisation) project ZCO-29 suggests that the presence of craters may help the stone chipping resistance of painted galvanneal panels.

The GAModeller has shown to be fairly accurate in predicting the coating constitution of the galvanneal coating. However, in its present state use as an on-line production tool would be limited. The main reason for this is the lack of additional process parameters such as substrate composition, bath temperature and immersion time within the model. Also, on-line production currently uses an X-ray machine to measure iron content and determine the amount of alloying. This method of determining the coating constitution is rapid, tested and accurate. Use of the GAModeller will therefore be on a research basis, used to plan experiments and give an understanding as to how the coating develops.

From an immediate commercial point of view the main result that has come from this piece of work is that if a galvannealing temperature above 530°C is used then no ζ is present within the coating. The preferred coating of many customers is a zero ζ coating, as this tends to have the most consistent forming properties. Normally a galvannealing temperature of around 500-510°C is used together with a long enough galvannealing time to ensure that all of the ζ has transformed to δ. This work has shown that by using a galvannealing temperature of above 530°C the coating consists of just δ and Γ even when some free zinc still remains in the coating. Therefore, as long as a shorter galvannealing time is used to compensate for the higher temperature, the coating will always consist of zero-ζ without the need for transformation of the ζ to δ.

8 CONCLUSIONS

The following chapter states the overall conclusions that have been derived from the completion of this project.

Crater Measurement Technique

- Use of the KS300 image analysis package for the identification and measurement of craters is both accurate and repeatable.
- Crater density can vary quite considerably over a single sample.

Influence of Process Parameters

- Increasing the annealing temperature from 700°C to 900°C leads to an increase in crater formation.
- Increasing the galvannealing temperature from 500°C to 510°C leads to a decrease in crater formation.
- Increasing the strip entry temperature results in a more ordered structure of the crystals at the base of the crater.
- Increasing the effective aluminium content of the spelter leads to a more disordered structure at the base of the crater.
- Neither the spelter temperature nor the temperature after dipping have any influence upon crater formation or crater morphology.

Crater Formation

- Craters nucleate during the first instances of dipping and within the high angle grain boundaries of grains oriented with {111} parallel to the sheet surface.
- Craters can nucleate across adjacent {111} oriented grains separated by low angle grain boundaries.
- During the galvannealing process the liquid zinc above the crystals is drawn into the surrounding coating.

Coating Failure

- Any improvement in powdering and flaking properties is the result of a more ductile substrate and not the effect of craters.
- Craters have no effect upon the powdering properties of the galvanneal coating.
- Craters may worsen the flaking properties of the galvanneal coating.
- Craters do not act as an effective inhibitor to crack propagation along the brittle Γ/substrate interface.

GAModeller

- The principle of diffusion couples is applicable to the formation of the galvanneal coating.
- The diffusion values published by Wakamatsu (1997) are applicable to the galvannealing process.
- Galvannealing above 530°C results in no ζ phase being present within the coating.

Overall it can be stated that during the first moments of dipping craters form by the epitaxial nucleation of the ζ iron-zinc intermetallic. This occurs upon grains oriented with {111} in the plane of the sheet, the proportion of which increases with an increase in annealing temperature. The presence of these craters within the coating has no major influence upon the failure properties of the coating. Instead, an increase in the annealing temperature creates a more ductile substrate that imposes less strain upon the coating and thus results in less coating failure. From a commercial point of view craters are neither a help nor a hindrance to the failure properties of the coating and simply give an indication as to the grain structure of the underlying substrate.

9 REFERENCES

Angeli J., Faderl J. and Gerderitsch J., (1993), Identification of Zinc-Iron Phases on Galvanneal Steel Sheets. The Physical Metallurgy of Zinc Coated Steel, Proceedings of the International Symposium of The Minerals, Metals and Minerals, p221.

Armiura M., Urai M., Iwaya J. and Iwai M., (1995), Effects of Press Forming Factors and Flash Plating on Coating Exfoliation of Galvannealed Steel Sheets. Galvatech'95 Conference Proceedings, p733.

Bdke B. L., (1997), Smithells Metals Reference Book, Butterworth and Heinmann, ISBN 0705636254, p7.13.

Cahn J.W. and Hilliard J.E., (1958), J. Chem. Phys. 28, p258.

Carless S.P., Jeffs B.D. and Randle V., (1998), Influence of Substrate Topography on the Formation of Iron-Zinc Phases and the Properties of Galvanneal Coatings. Proc. Galvatech International Conference 1998, p687.

Carless S.P. (2000), Engineering Doctorate Thesis, University of Wales, Swansea, Influence of Steel Strip Topography on the Quality of Galvanneal Coatings, p102.

Coffin C. and Thompson S.W., (1995) The Effect of 0.07wt% Phosphorous on the Galvannealing Behaviour of a Niobium/Titanium Stabilised Interstitial Free Sheet Steel. Galvatech'95 Conference Proceedings, p121.

De Cooman, De Mare and Meseure (1998), On the Visual Appearance of Painted Galvannealed Panels. Zinc Based Steel Coating Systems, Production and Performance, Proceedings of the International Symposium of The Minerals, Metals and Materials Society, p337.

Deits and Matlock, (1990), Formability of Coated Sheet Steels. An Analysis of Surface Damage Mechanisms. Zinc Based Coating Systems, Metallurgy and Performance, Proceedings of the International Symposium of The Minerals, Metals and Materials Society, p297.

Eliott L., (1999), Formability Assessment of Pre-phosphated Galvanneal. BSSP Technical Note, Report Number WL/PE/TN/D17/4/99/D.

Foct J., (1992), Microstructure and Mechanical Behaviour of Zinc Coatings. Galvatech 1992 Conference Proceedings, p468.

Foct J., Reumont G. and Perrot P. (1993), The Morphology of Zinc Coatings. The Physical Metallurgy of Zinc Coated Steel, Proceedings of the International Symposium of The Minerals, Metals and Materials Society, p1.

Fujii S. and Nishimura K., (2000), Effect of the Coating Layer Morphology on the Powdering Resistance of Galvannealed Steel Sheets, Galvanised Steel Sheet Forum – Automotive Conference Proceedings, The Institute of Materials, p173.

Guttmann M., LePretre Y., Aubry A., Roch M-J, Moreau T., Drillet P., Mataigne J.M. and Baudin H. (1995), Mechanisms of the Galvanising Reaction. Influence of Ti and P Contents in Steel and of its Surface Microstructure After Annealing. Galvatech '95 Conference Proceedings, p295.

Hertveldt I., Craenen J., Dilewijns J., Blanpain B., Xhoffer C. and DE Cooman B.C., (1998), The Structure of the Inhibition Layer After Hot Dip Galvanising of TiIF DDQ, TiNb IF DDQ and TiNb+P IF HSS Substrates. Zinc Based Steel Coating Systems, Production and Performance, Proceedings of the International Symposium of the Minerals, Metals and Materials Society, p13.

Holliday *et al.*, (1996), Prediction of Electrode Campaign Life when Spot Welding Zinc Coated Steels Incorporating Electrode Tip Dressing Operations. Iron and Steelmaking, Vol. 23, No. 2, p157.

Inagaki J., Morita M. and Sagiyama M., (1991), Iron-Zinc Alloying Reaction on Interstitial Free Steels. Surface Engineering Vol.7 No.4, p331.

Inagaki J., Sakurai M. and Watanabe T., (1995), Alloying Reaction in Hot-Dip Galvanising and Galvannealing Processes. ISIJ International Vol. 35 No.11, p1388.

Isobe M., Masuda A. and Yamato Y, (1992) Initial Alloying Behaviour in the Galvannealing Process. CAMP-ISIJ Vol.5, p1629.

Ito T., (1977) Nisshin Steel Techincal Report, Vol 36, p39.

Jordan C.E., Goggins K.M. and Marder A.R., (1992), Kinetics and Formability of Hot-Dip Galvanneal Coatings. Galvatech'92 Conference Proceedings, p137.

Jordan C and Marder A. R, (1998), Inhibition Layer Breakdown and Outburst Fe-Zn Alloy Formation During Galvannealing. Zinc Based Steel Coating Systems, Production and Performance, Proceedings of the International Symposium of the Minerals, Metals and Materials Society, p115.

Kato C., Koumura H. and Vesugi V., (1993), Influence of Phase Composition on Formability of Galvannealed Steel Sheet. The Physical Metallurgy of Zinc Coated Steel, Proceedings of the International Symposium of The Minerals, Metals and Materials Society, p241.

Kawaguchi H. and Hirose Y., (1993), Structural Control of Galvannealed Alloy Layer by Adding Mn to the Galvanising Bath. The Physical Metallurgy of Zinc Coated Steel, The Minerals, Proceedings of the International Symposium of Metals and Materials Society, p153.

Kim J. and Chung J., (1998), Alloying Behaviour of Hot Dip Galvannealed Sheet Steels Containing Silicon. Zinc Based Steel Coating Systems, Production and Performance, Proceedings of the International Symposium of The Minerals, Metals and Materials Society, p157.

Kunde N.D., Saran M.J. and Michal G.M, (1998), Correlation of Pre-Phosphate Treatment, Surface Friction and Powdering of Galvanneal During Forming. Society of Automotive Engineers, p17.

Lamberigts M., (1992), Kinetics of Fe-Zn Reactions During Galvannealing. Galvatech'92 Conference Proceedings, p199.

Martin J., (1996), Materials for Engineering, The Institute of Materials, ISBN 1-86125-012-6, p121.

Mataigne J., Drillet P., Prat J.M., Mareuse D., Terraux P. and Guttmann M., (1995), Optimised Galvannealed Coating Microstructure for Automotive Applications. Galvatech'95 Conference Proceedings, p589.

McDevitt E., Morimoto Y. and Meshii M., (1997), Characterisation of the Fe-Al Interfacial Layer in a Commercial Hot Dip Galvanised Coating. ISIJ International Vol.37 No.8, p776.

McDevitt E. and Meshii M., (1998), Electron Microscopy Study of the Microstructural Evolution in the Early Stages of Galvannealing. Zinc Based Steel Coating Systems, Production and Performance, Proceedings of the International Symposium of The Minerals, Metals and Materials Society, p127.

McDevitt E.T. and Meshii M., (1998), Microstructural Evolution During Galvannealing Formation and Breakdown of the Fe-Al layer. Galvatech '98 Conference Proceedings, p153.

Morimoto Y., McDevitt E. and Meshii M., (1997), Characterisation of the Fe-Al Layer Formed in the Initial Stages of Hot Dip Galvanising. ISIJ International Vol. 37, No. 9, p906.

Nakamori T., Adachi Y., Toki T. and Shibuya A., (1995), Effect of Microstructure of Base Steel on Fe-Zn Alloy Growth During Galvanising of an IF Steel. ISIJ International, Vol. 36 No. 2, p179.

Onishi M, Wakamatsu Y and Miura H, (1974), Formation and Growth Kinetics of Intermediate Phases in Fe-Zn Diffusion Couples, Trans JIM, Vol 15, p331.

Peterson and Rothman, (1997), Smithells Metals Reference Book, Butterwoth and Heinmann, ISBN 0705636254, p7.13.

Porter D.A. and Easterling K.E., (1995), Phase Transformations in Metals and Alloys, Chapman & Hall, London, ISBN 0-412-45030-5, p 60.

Price S. (1999), Engineering Doctorate Thesis, University of Wales, Swansea, Formation of the Inhibition Layer During Galvanneal Production, p158.

Rangarajan V, (1997), Galvanneal Powdering in Drawbeads. Society of Automotive Engineers, p1.

Scheers J., De Cooman B.B. and Vermeulen M., (1996), Frictional Properties of Galvannealed Steel Sheets. 19th IDDRG Biennial Congress, p515.

Stevenson E.V., (1998), Investigation of the Effects of Galvannealing Cycles on Galvatite ZF Phase Composition. BSSP Tech Report WL/PD/TN/3416/16/98/D.

Tang N.Y. and Adams G.R. (1993), Studies on the Inhibition of Alloy Formation in Hot-Dip Galvanised Coatings. The Physical Metallurgy of Zinc Coated Steel, The Minerals, Proceedings of the International Symposium of Metals and Materials Society, p42.

Tang N.Y., (1996), 450°C Isotherm of Zn-Fe-Al Phase Diagram Update. Journal of Phase Equilibria Vol. 17 No. 5, pp396-398.

Tang N. Y., (1998), Thermodynamics and Kinetics of Alloy Formation in Galvanised Coatings. Zinc Based Steel Coating Systems, Production and Performance, Proceedings of the International Symposium of The Minerals, Metals and Materials Society, p4.

Toki, (1994), Effect of P content in Ultra-Low Carbon Ti Stabilised Steel on the Rate of Fe-Zn Alloy Formation Through Ferrite Grain Boundary Diffusion During Hot-Dip Galvanizing. The Physical Metallurgy of Zinc Coated Steel, Proceedings of the International Symposium of The Minerals, Metals and Materials Society, p169.

Urai M., Arimura M., Sakai H and Nomura S., (1996), Effects of Galvanising and Galvannealing Conditions on Powdering Characteristics of Galvannealed Steel Sheets. Kobelco Technology Review No. 19, p27.

Urai M., Iwaya S., Iwai H. and Arimua M., (1999), Effects of Press Forming Conditions and Coating Structure on Flaking Phenomenon in Galvannealed Steel Sheets. Kobelco Technology Review No. 22, p48.

Van der Heiden A., (1993), Galvanneal Microstructure and Anti Powdering Windows. The Physical Metallurgy of Zinc Coated Steel, Proceedings of the International Symposium of The Minerals, Metals and Materials Society, p251

Wakamatsu (1997), Smithells Metals Reference Book, Butterworth and Heinmann, ISBN 0705636254, p7.13

Wilkinson D.S.. (1997), Mass Transport in Materials. Custom Courseware, McMaster University, Ontario Canada, Chapter 7.

Wright R. (1998), Control of Cratering of Galvannealed Coatings, International Lead Zinc Reasearch Organisation, Project ZCO-29.

Zhong W., Ng H.F. and James J.M., (1998), Correlation Between Adhesion Properties and the Interfacial Bonding Strength of Galvanneal Coatings. Zinc Based Steel Coatings, Production and Performance, Proceedings of the International Symposium of The Minerals, Metals and Materials Society p185.

APPENDIX

The complete Visual Basic™ code for the GAModeller is detailed and annotated below:

'Declaration of variables

```
Option Explicit
Dim R_boundary As Single
Dim L_boundary As Single
Dim Far_L_boundary As Single
Dim Far_R_boundary As Single
Dim D0 As Single
Dim Q As Single
Dim k As Single
Dim Time As Single
Dim n As Single
Dim thickness As Single
Dim inhibition As Single
Dim D As Single
Dim zeta As Single
Dim delta As Single
Dim gamma As Single
Dim eta As Single
Dim etafecontent As Single
Dim zetafecontent As Single
Dim deltafecontent As Single
Dim gammafecontent As Single
Dim zetaover As Single
Dim value As Single
Dim HEATtime As Single
Dim eqtime As Single
Dim speed As Single
Dim coating_thickness As Single
```

'Clear the graph

```
Private Sub Clear_Click()
Cls
End Sub
```

'Decrease the coating thickness by half a micron

```
Private Sub CoatThminus_Click()
CoatThinput.Text = CoatThinput.Text - 0.5
If CoatThinput.Text < 0 Then CoatThinput = 0
End Sub
```

'Increase Coating thickness by half a micron

```
Private Sub CoatThplus_Click()
CoatThinput.Text = CoatThinput.Text + 0.5
End Sub
```

```
'Decrease the Galvannealing Time by one second
Private Sub DecGATime_Click()
GATimeInput.Text = GATimeInput.Text - 1
If GATimeInput.Text < 0 Then GATimeInput.Text = 0
End Sub

'Decrease the effective aluminium by 0.005%
Private Sub Effalminus_Click()
EffAlinput.Text = Format(EffAlinput.Text - 0.005, "0.000")
If EffAlinput.Text < 0 Then EffAlinput.Text = 0
End Sub

'Increase the Effective aluminium by 0.005%
Private Sub EffAlplus_Click()
EffAlinput.Text = Format(EffAlinput.Text + 0.005, "0.000")
End Sub

'Decrease the galvannealing temperature by 1 degree
Private Sub GATempminus_Click()
GATempinput.Text = GATempinput.Text - 1
If GATempinput.Text < 0 Then GATempinput = 0
End Sub

'Increase the galvannealing temperature by 1 degree
Private Sub GATempplus_Click()
GATempinput.Text = GATempinput.Text + 1
End Sub

'Increase Galvannealing Time by one second
Private Sub IncGATime_Click()
value = GATimeInput.Text + 1
GATimeInput.Text = value
End Sub

'Vary the x and y scales on the graph
Private Sub MaxXminus_Click()
MaxX.Text = MaxX.Text - 1
If MaxX.Text < 0 Then MaxX.Text = 0
If MaxX.Text = MinX.Text Then MaxX.Text = MinX.Text - 1
End Sub

Private Sub MaxXplus_Click()
MaxX.Text = MaxX.Text + 1
If MaxX.Text = MinX.Text Then MaxX.Text = MinX.Text + 1
End Sub

Private Sub MinXminus_Click()
MinX.Text = MinX.Text - 1
If MinX.Text < 0 Then MinX.Text = 0
If MinX.Text = MaxX.Text Then MinX.Text = MaxX.Text - 1
End Sub

Private Sub MinXplus_Click()
MinX.Text = MinX.Text + 1
If MinX.Text = MaxX.Text Then MinX.Text = MaxX.Text + 1
End Sub
```

```
'Set Galvannealing Time back to zero
Private Sub ResetGA_Click()
GATimeInput.Text = 0
End Sub

'Exit Program
Private Sub Exit_Click()
End
End Sub

'Change to HDS Option
Private Sub GATimeOption_Click()
GATimeLbl.Visible = True
linespeedLbl.Visible = False
Label4.Visible = False
Label5.Visible = False
Furnace.Visible = False
GATimeSelect.Caption = "GA Time"
Equivalent.Caption = "m/min"
MaxX.Text = 30
End Sub

'Change to Zodiac Option
Private Sub LineSpeedOption_Click()
GATimeLbl.Visible = False
linespeedLbl.Visible = True
Label4.Visible = True
Label5.Visible = True
Furnace.Visible = True
GATimeSelect.Caption = "Line Spd"
Equivalent.Caption = "Secs"
MaxX.Text = Furnace.Text
If GATimeInput.Text = 0 Then GATimeInput.Text = 1
End Sub


Private Sub Calculate_Click()
'*********************************************
'Calculate the time delay due to the Inhibition Layer
'*********************************************

'Calculate diffusion of Zn through Inhibition Layer
D0 = 0.0000245
Q = 119600
D = D0 * (2.7182 ^ (0 - Q / (8.314 * (GATempinput.Text + 273))))

'Calculate thickness of Inhibition layer from work of Guttman, Price Etc
If EffAlinput.Text <= 0 Then EffAlinput = 0.000001
thickness = 866 + 376 * (Log(EffAlinput.Text) / Log(2.7182))
If thickness < 0 Then thickness = 0

'Display the thickness in nanometres
InhibLayer.Caption = Format(thickness, "###.##")
thickness = thickness / 1000000000
```

```
'Calculate the time it takes for Zn to diffuse through
inhibition = (thickness * thickness) / (0.01 * D)


'****************************************
'Calculate the thickness of the zeta phase
'****************************************

'Boundary conditions from the phase diagram
R_boundary = 7.2
If GATempinput.Text > 530 Then L_boundary = 7.2
If GATempinput.Text <= 530 Then L_boundary = (GATempinput.Text + 583.9) / 160
If L_boundary < 7.05 Then L_boundary = 7.05
Far_L_boundary = 0.25
Far_R_boundary = 7.95

'Diffusion Coefficients for iron through the zeta phase
D0 = 0.00000228
Q = 83300

D = D0 * (2.7182 ^ ((0 - Q) / (8.314 * (GATempinput.Text + 273))))

k = (2 * D * (((R_boundary - L_boundary) / (L_boundary - Far_L_boundary)) + ((R_boundary -
L_boundary) / (Far_R_boundary - R_boundary)))) ^ 0.5

'If the user is using the line speed parameter then the immersion time needs to be
adjusted
If LineSpeedOption = True Then
If GATimeInput.Text = 0 Then GATimeInput.Text = 1
End If

'If the zodiac option is used then the Galvannealing time is dependent upon the line
'speed
'The equivalent HDS galvannealing time is also calculated
If LineSpeedOption = True Then
If GATimeInput.Text = 0 Then GATimeInput.Text = 1
HEATtime = Furnace.Text / (GATimeInput.Text / 60)
Equivalent.Caption = "Secs"
eqtime = Furnace.Text / (GATimeInput.Text / 60)
convert.Caption = Format(eqtime, "###.##")
End If

'If the HDS option is used then the equivalent line speed is calculated
If LineSpeedOption = False Then
HEATtime = GATimeInput.Text
Equivalent.Caption = "m/min"
End If

'zero GA time
If GATimeInput.Text = 0 Then
convert.Caption = "N/A"
Else
speed = 60 * (Furnace.Text / GATimeInput.Text)
convert.Caption = Format(speed, "###.##")
End If
```

```
Time = HEATtime - inhibition
If Time < 0 Then Time = 0

n = 0.36

thickness = k * Time ^ n
If GATempinput.Text > 530 Then thickness = 0

zeta = thickness * 1000000

'************************************
'Calculate the delta phase thickness
'************************************

'Boundary conditions from the phase diagram
R_boundary = 11.4
L_boundary = 7
Far_L_boundary = 6.2
Far_R_boundary = 21

'Change of boundary if temperature is above 530C

If GATempinput.Text > 530 Then L_boundary = 7 + ((1.5 / 90) * GATempinput - 530)

'Diffusion coefficients of iron through the delta phase
D0 = 0.000000282
Q = 80400

D = D0 * (2.7182 ^ (0 - Q / (8.314 * (GATempinput.Text + 273))))

k = (2 * D * (((R_boundary - L_boundary) / (L_boundary - Far_L_boundary)) + ((R_boundary -
L_boundary) / (Far_R_boundary - R_boundary)))) ^ 0.5

Time = HEATtime - inhibition
If Time < 0 Then Time = 0

n = 0.43

thickness = k * Time ^ n

delta = thickness * 1000000

'****************************************
'Calculate the thickness of the Gamma Phase
'****************************************

'Boundary conditions from the phase diagram
R_boundary = 28
L_boundary = 21
Far_L_boundary = 11.4
Far_R_boundary = 100 - ((GATempinput.Text - 300) / 22.8)

'Diffusion coefficients of iron through the gamma phase
D0 = 0.000000105
Q = 92100
```

```
D = D0 * (2.7182 ^ (0 - Q / (8.314 * (GATempinput.Text + 273))))

k = (2 * D * (((R_boundary - L_boundary) / (L_boundary - Far_L_boundary)) + ((R_boundary -
L_boundary) / (Far_R_boundary - R_boundary)))) ^ 0.5

Time = HEATtime - inhibition
If Time < 0 Then Time = 0

n = 0.24 - (0.5 * EffAlinput.Text)
If n < 0 Then n = 0.000001
If n > 0.3 Then n = 0.3

thickness = k * Time ^ n

gamma = thickness * 1000000

'**********************************
'Calculate the overall constitution
'**********************************

coating_thickness = CoatThinput.Text

eta = coating_thickness - (zeta + delta + gamma)
If eta <= 0 Then eta = 0
If eta = 0 Then zeta = coating_thickness - (delta + gamma)

'Effectively the amount of iron that would have escaped
zetaover = zeta

If zeta <= 0 Then zeta = 0
If zeta = 0 And eta = 0 Then delta = coating_thickness - gamma

etamicrons.Caption = Format(eta, "##0.##")
zetamicrons.Caption = Format(zeta, "##0.##")
deltamicrons.Caption = Format(delta, "##0.##")
Gammamicrons.Caption = Format(gamma, "##0.##")

etaPerc.Caption = Format(eta / CoatThinput.Text * 100, "##0.##")
zetaPerc.Caption = Format(zeta / CoatThinput.Text * 100, "##0.##")
deltaPerc.Caption = Format(delta / CoatThinput * 100, "##0.##")
gammaPerc.Caption = Format(gamma / CoatThinput * 100, "##0.##")

'**************************************
'Calculate the Fe content of the coating
'**************************************

etafecontent = 0.003
zetafecontent = 6.25
deltafecontent = 7
gammafecontent = 20

'The enrichment of the delta and gamma phases
If zeta = 0 Then
deltafecontent = (7 - (zetaover / 2.5))
gammafecontent = (20 - (zetaover / 1.3))
End If
If deltafecontent > 12 Then deltafecontent = 12
```

```
If gammafecontent > 30 Then gammafecontent = 30

Fewghtperc.Caption = Format((etafecontent * eta + zetafecontent * zeta + deltafecontent *
delta + gammafecontent * gamma) / coating_thickness, "##0.##")
Fegrams.Caption = Format((Fewghtperc.Caption / 100) * coating_thickness * 7.88, "##0.##")

'*********************************
'Calculate the amount of powdering
'*********************************

If GATempinput.Text <= 530 Then powdering.Caption = Format(0.000113 * Exp(0.865 *
Fegrams.Caption), "0.####")
If GATempinput.Text > 530 Then powdering.Caption = Format(0.000137 * Exp(0.594 *
Fegrams.Caption), "0.####")

'*********************************
'Display schematic microstructure
'*********************************
substratepic.Top = 2880
substratepic.Left = 10440
gammapic.Left = 10440
deltapic.Left = 10440
zetapic.Left = 10440
etapic.Left = 10440

gammapic.Top = substratepic.Top - 1920 * (gammaPerc.Caption / 100)
gammapic.Height = substratepic.Top - gammapic.Top

deltapic.Top = gammapic.Top - 1920 * (deltaPerc.Caption / 100)
deltapic.Height = gammapic.Top - deltapic.Top
If deltaPerc.Caption = 0 Then deltapiclab.Visible = 0
If deltaPerc.Caption > 0 Then deltapiclab.Visible = 1
deltapiclab.Top = deltapic.Top

zetapic.Top = deltapic.Top - 1920 * (zetaPerc.Caption / 100)
zetapic.Height = deltapic.Top - zetapic.Top
If zetaPerc.Caption <= 10 Then zetapiclab.Visible = 0
If zetaPerc.Caption > 10 Then zetapiclab.Visible = 1
zetapiclab.Top = zetapic.Top

etapic.Top = zetapic.Top - 1920 * (etaPerc.Caption / 100)
etapic.Height = zetapic.Top - etapic.Top
If etaPerc.Caption <= 10 Then etapiclab.Visible = 0
If etaPerc.Caption > 10 Then etapiclab.Visible = 1
etapiclab.Top = etapic.Top

End Sub
```

```
'*********************************************
'*
'*          Display the Graph
'*
'*********************************************

Private Sub Display_Graph_Click()

Dim X As Integer
Dim zetaY As Single
Dim etaY As Single
Dim deltaY As Single
Dim gammaY As Single
Dim FeY As Single
Dim GAtime As Single
Dim time_step As Single
Dim zeta_thickness As Single
Dim delta_thickness As Single
Dim gamma_thickness As Single
Dim zeta_growth_rate As Single
Dim delta_growth_rate As Single
Dim gamma_growth_rate As Single

Display_Graph.MousePointer = 11
Display_Graph.Caption = "Computing"

'Alter the scale on the thickness axis
LabY1.Caption = Format(1 * (CoatThinput.Text / 10), "##.#")
LabY2.Caption = Format(2 * (CoatThinput.Text / 10), "##.#")
LabY3.Caption = Format(3 * (CoatThinput.Text / 10), "##.#")
LabY4.Caption = Format(4 * (CoatThinput.Text / 10), "##.#")
LabY5.Caption = Format(5 * (CoatThinput.Text / 10), "##.#")
LabY6.Caption = Format(6 * (CoatThinput.Text / 10), "##.#")
LabY7.Caption = Format(7 * (CoatThinput.Text / 10), "##.#")
LabY8.Caption = Format(8 * (CoatThinput.Text / 10), "##.#")
LabY9.Caption = Format(9 * (CoatThinput.Text / 10), "##.#")
MaxY.Caption = Format(CoatThinput.Text, "##.##")

'Alter the scale on the fe content axis
LabFeY1.Caption = Format(1 * (FeYMax.Text / 7), "##.#")
LabFeY2.Caption = Format(2 * (FeYMax.Text / 7), "##.#")
LabFeY3.Caption = Format(3 * (FeYMax.Text / 7), "##.#")
LabFeY4.Caption = Format(4 * (FeYMax.Text / 7), "##.#")
LabFeY5.Caption = Format(5 * (FeYMax.Text / 7), "##.#")
LabFeY6.Caption = Format(6 * (FeYMax.Text / 7), "##.#")

'Alter the scale on the X axis
LabX1.Caption = Format(MinX.Text + 1 * ((MaxX.Text - MinX.Text) / 6), "##.##")
LabX2.Caption = Format(MinX.Text + 2 * ((MaxX.Text - MinX.Text) / 6), "##.##")
LabX3.Caption = Format(MinX.Text + 3 * ((MaxX.Text - MinX.Text) / 6), "##.##")
LabX4.Caption = Format(MinX.Text + 4 * ((MaxX.Text - MinX.Text) / 6), "##.##")
LabX5.Caption = Format(MinX.Text + 5 * ((MaxX.Text - MinX.Text) / 6), "##.##")

'Start Point of the Graph for the different phases
X = 460
zetaY = 8150
deltaY = 8150
```

```
gammaY = 8150

If LineSpeedOption = True Then
Label10.Caption = "Dist (m)"
Else
Label10.Caption = "Time (s)"
End If

'Do loop for drawing the graph

Do While X < 7800
If etacheck.value = 1 Then PSet (X, etaY), RGB(255, 255, 255)
If zetacheck.value = 1 Then PSet (X, zetaY), QBColor(11)
If deltacheck.value = 1 Then PSet (X, deltaY), RGB(0, 255, 0)
If gammacheck.value = 1 Then PSet (X, gammaY), RGB(255, 0, 0)
If fecheck.value = 1 Then PSet (X, FeY), QBColor(14)

If LineSpeedOption = True Then
If GATimeInput.Text = 0 Then GATimeInput.Text = 1
GAtime = MinX.Text + (X - 460) / ((7335 * (GATimeInput.Text / 60)) / (MaxX.Text -
MinX.Text))
Else
GAtime = MinX.Text + (X - 460) / (7335 / (MaxX.Text - MinX.Text))
End If

'**********************************************
'Calculate the time delay due to the Inhibition Layer
'**********************************************

'Calculate diffusion of Zn through Inhibition Layer
D0 = 0.0000245
Q = 119600
D = D0 * (2.7182 ^ (0 - Q / (8.314 * (GATempinput.Text + 273))))

'Calculate thickness of Inhibition layer from work of Guttman, Price Etc
If EffAlinput.Text <= 0 Then EffAlinput = 0.000001
thickness = 866 + 376 * (Log(EffAlinput.Text) / Log(2.7182))
If thickness < 0 Then thickness = 0

thickness = thickness / 1000000000

'Calculate the time it takes for Zn to diffuse through
inhibition = (thickness * thickness) / (0.01 * D)

'**********************************************
'Calculate the thickness of the zeta phase
'**********************************************

'Boundary conditions from the phase diagram
R_boundary = 7.2
If GATempinput.Text > 530 Then L_boundary = 7.2
If GATempinput.Text <= 530 Then L_boundary = (GATempinput.Text + 583.9) / 160
If L_boundary < 7.05 Then L_boundary = 7.05
Far_L_boundary = 0.25
Far_R_boundary = 7.95
```

```
'Diffusion coefficients of iron through the zeta phase
D0 = 0.00000228
Q = 83300

D = D0 * (2.7182 ^ ((0 - Q) / (8.314 * (GATempinput.Text + 273))))

k = (2 * D * (((R_boundary - L_boundary) / (L_boundary - Far_L_boundary)) + ((R_boundary -
L_boundary) / (Far_R_boundary - R_boundary)))) ^ 0.5

If LineSpeedOption = True Then
If GATimeInput.Text = 0 Then GATimeInput.Text = 1
End If

Time = GAtime - inhibition
If Time < 0 Then Time = 0

n = 0.36

zeta_thickness = k * Time ^ n

If GATempinput.Text > 530 Then zeta_thickness = 0

zetaY = zeta_thickness * 1000000

'************************************
'Calculate the delta phase thickness
'************************************

'Boundary conditions from the phase diagram
R_boundary = 11.4
L_boundary = 7
Far_L_boundary = 6.2
Far_R_boundary = 21

'Change of boundary if temperature is above 530C
If GATempinput.Text > 530 Then L_boundary = 7 + ((1.5 / 90) * (GATempinput - 530))

'Diffusion coefficients of iron through the delta phase
D0 = 0.000000282
Q = 80400

D = D0 * (2.7182 ^ (0 - Q / (8.314 * (GATempinput.Text + 273))))

k = (2 * D * (((R_boundary - L_boundary) / (L_boundary - Far_L_boundary)) + ((R_boundary -
L_boundary) / (Far_R_boundary - R_boundary)))) ^ 0.5

Time = GAtime - inhibition
If Time < 0 Then Time = 0

n = 0.43

delta_thickness = k * Time ^ n

deltaY = delta_thickness * 1000000
```

```
'*****************************************
'Calculate the thickness of the Gamma Phase
'*****************************************

'Boundary conditions from the phase diagram
R_boundary = 28
L_boundary = 21
Far_L_boundary = 11.4
Far_R_boundary = 100 - ((GATempinput.Text - 300) / 22.8)

'Diffusion coefficients of iron through the gamma phase
D0 = 0.000000105
Q = 92100

D = D0 * (2.7182 ^ (0 - Q / (8.314 * (GATempinput.Text + 273))))

Time = GAtime - inhibition
If Time < 0 Then Time = 0

n = 0.24 - (0.5 * EffAlinput.Text)
If n < 0 Then n = 0.0000001
If n > 0.3 Then n = 0.3

k = (2 * D * (((R_boundary - L_boundary) / (L_boundary - Far_L_boundary)) + ((R_boundary -
L_boundary) / (Far_R_boundary - R_boundary)))) ^ 0.5

gamma_thickness = k * Time ^ n

gammaY = gamma_thickness * 1000000

'*********************************
'Calculate the overall constitution
'*********************************

coating_thickness = CoatThinput.Text

etaY = coating_thickness - (zetaY + deltaY + gammaY)
If etaY <= 0 Then etaY = 0
If etaY = 0 Then zetaY = coating_thickness - (deltaY + gammaY)

'Effectively the amount of iron that would have escaped
zetaover = zetaY

If zetaY <= 0 Then zetaY = 0
If zetaY = 0 And etaY = 0 Then deltaY = coating_thickness - gammaY

If zerozeta Then
If zetaY = 0 And etaY = 0 Then Exit Do
End If

'*************************************
'Calculate the Fe content of the coating
'*************************************

etafecontent = 0.003
zetafecontent = 6.25
```

```
deltafecontent = 7
gammafecontent = 20

'The enrichment of the delta and gamma phases
If zetaY = 0 Then
deltafecontent = (7 - (zetaover / 2.5))
gammafecontent = (20 - (zetaover / 1.3))
End If
If deltafecontent > 12 Then deltafecontent = 12
If gammafecontent > 30 Then gammafecontent = 30

FeY = 8150 - ((etafecontent * etaY + zetafecontent * zetaY + deltafecontent * deltaY +
gammafecontent * gammaY) / coating_thickness) * (4650 / FeYMax.Text)
etaY = 8150 - (etaY * (4650 / coating_thickness))
zetaY = 8150 - (zetaY * (4650 / coating_thickness))
deltaY = 8150 - (deltaY * (4650 / coating_thickness))
gammaY = 8150 - (gammaY * (4650 / coating_thickness))

X = X + 25

Loop

Display_Graph.Caption = "&Graph"
Display_Graph.MousePointer = 0

End Sub
```